Universidad Complutense de Madrid

Facultad de Ciencias Físicas

Erasmus Mundus Joint Master Degree in Nuclear Physics

Master Thesis

Experimental tests of a scanner prototype for medical imaging with protons developed at IEM-CSIC

As part of the research activities of the

Grupo de Física Nuclear Experimental

Instituto de Estructura de la Materia - Consejo Superior de Investigaciones Científicas

Author:
Amanda Nathali Nerio Aguirre

Supervisors:
José Antonio Briz Monago
María José García Borge

A thesis submitted in fulfillment of the requirements for the degree of Master of Science

September, 2021

Declaration of Authorship

I, Amanda Nathali Nerio Aguirre, with NIE Y8513858P, student of the Erasmus Mundus Joint Master Degree in Nuclear Physics at the Facultad de Ciencias Físicas, of the Universidad Complutense de Madrid, in the academic year 2020-2021, as author of the master's thesis titled "Experimental tests of a scanner prototype for medical imaging with protons developed at IEM-CSIC", whose supervisors are José Antonio Briz Monago, and María José García Borge; DECLARE THAT:

- The master's thesis that I present has been prepared by me and it is original.
- I do not copy, or use ideas, formulations, comprehensive quotes and illustrations of any work, article, report, or document (in printed or electronic version), without clearly and strictly mentioning its origin, both in the body of the text and in the bibliography.
- I also declare that the data is true and that I have not made use of unauthorized information from any written source of another person or from any other source.
- In the same way, I am fully aware that failure to respect these terms is subject to university sanctions and/or other sanctions.

Signed:

Place: Madrid, Spain

Date: February 10, 2021.

A mi mamita Mauricia:
Gracias por todos los años que ha estado conmigo, por todo el amor y la comprensión, por todos los consejos y todas las risas.
Con amor y admiración, a una de las mujeres más importantes de mi vida.

Acknowledgements

I would like to express my most sincere gratitude to my research supervisors José Antonio Briz Monago and María José García Borge, for the opportunity they gave me to work with such a great group at the Experimental Nuclear Physics group of the IEM-CSIC and for all their guidance in the development of this work. I would also like to thank all the members of the Experimental Nuclear Physics group, especially Olof Tengblad, for his invaluable advice and mentorship throughout this research and Vicente García Távora for making me feel like another member of the group.

I am incredibly grateful to my parents, Ana Paula and José Malaquías, for their love and support during this period we spent apart, for all the short and long talks, and for encouraging me in all those moments that felt impossible. I can not leave aside the support I received from my baby sister Marcela during the best and worst days of this adventure. And to my brother José Carlos and the rest of my family, for their love.

I want to acknowledge my dearest friends Mojahed Abushawish, Ignacio González Oliva, and Claudia Ayala for their unconditional support and help in my research, and for always being there for me during this great adventure.

Contents

List of Figures

List of Tables

List of Abbreviations

ADC	**A**nalog-to-**D**igital **C**onverter
CEPA	**C**ALIFA **E**ndcap **P**hoswich **A**rray
CFD	**C**onstant **F**raction **D**iscrimitator
CT	**C**omputed **T**omography
DAQ	**D**ata **Acq**uisition system
DSSSD	**D**ouble **S**ided **S**ilicon **S**trip **D**etector
HU	**H**ounsfield **U**nit
LED	**L**eading-**E**dge **D**iscrimitator
pCT	**p**roton **C**omputed **T**omography
PMMA	**P**oly (**m**ethyl **m**eth**a**crylate)
QDC	Charge-to-**D**igital **C**onverter
RBE	**R**adio**b**iological **E**ffectiveness
ROI	**R**egion **O**f **I**nterest
RSP	**R**elative **S**topping **P**ower
SOBP	**S**pread-**O**ut **B**ragg **P**eak
TFA	**T**iming **F**ilter **A**mplifier
TFLU	**T**hree-**F**old **L**ogic **U**nit

"Research is what I'm doing when I don't know what I'm doing"

—Wernher von Braun

UNIVERSIDAD COMPLUTENSE DE MADRID

Abstract

Facultad de Ciencias Físicas

Master of Science

Experimental tests of a scanner prototype for medical imaging with protons developed at IEM-CSIC

by Amanda Nathali NERIO AGUIRRE

Proton therapy requires precise knowledge of the patient's anatomy to guarantee an accurate dose delivery. X-ray computed tomography (CT) images are currently used to calculate the relative stopping power (RSP) needed for proton therapy treatment planning. Recent studies indicate that tomographic imaging using protons has the potential to provide directly more accurate measurement of RSP with significantly lower radiation dose than X-rays. The planar imaging capabilities of the proton CT (pCT) scanner prototype developed at IEM-CSIC were studied at the Cyclotron Centre Bronowice in Krakow, Poland.

The pCT scanner prototype is composed by a tracking system of two double-sided silicon strip detectors of 1000μm, and the CEPA4 detector as the residual energy detector. Three different planar phantoms of aluminum and PMMA were imaged using proton beams with energies between 95 and 120 MeV, a uniform phantom of PMMA, a cross-shaped phantom of aluminum and PMMA, and a Derenzo-type phantom of aluminum and PMMA.

Planar images were reconstructed from pixelated detectors and they were converted into *continuous* images by uniformly distributing the statistics of each pixel over the pixel area. With the pCT scanner prototype it was possible to differentiate and localize the different materials that composed the phantoms. The images displayed great fidelity with respect to the actual shapes. The dimensions of the cross-shaped and Derenzo-type phantom were obtained by getting the grey-level profiles of different regions of interest (ROI) and fitting them to a super Gaussian function, reporting their values within the full width at half maximum (FWHM) and full width at tenth maximum (FWTM). For the cross-shaped phantom, the measurements of the FWHM underestimated the real dimensions in 4% to 23%. The FWTM gave more accurate results, offering smaller deviations (1%-13%). The spatial resolution of this pCT scanner prototype was determined with the study of the Derenzo-type phantom. The scanner prototype was capable to resolve structures with sizes up to 2 mm and 3 mm while using proton beams of 100 MeV and 110 MeV, respectively.

Chapter 1

Introduction

Initially, X-rays have been used in radiology to image bones in two dimension which then further evolved to 3-dimensional imaging using computed tomography scanners. X-rays in the megavoltage range are also used in therapeutic applications. Technologies used for cancer treatment take advantage of high energy photons emitted either electrically as in the case of linear accelerators or through high-energy sealed sources like Co-60 which emits gamma rays in the MeV energy range [1]. The emitted radiations interact with tissues via atomic and nuclear interactions and the energy is deposited to the tissue through these processes. Nowadays, LINACs and Co-60 teletherapy machines are the most widely used radiotherapy machines. However, in terms of therapeutic ratio, proton therapy technologies are expected to outperform conventional photon or electron therapy [2]. The use of protons in radiotherapy makes the delivery of higher doses to tumor while minimizing the total dose delivered to critical structures feasible. This is due to the finite range of a proton beam, unlike photon beams which have a short build-up region before an exponential decrease in energy deposition with increasing depth in tissue. The energy transfer by protons depends on the proton velocity, as they lose energy, their energy transfer increases, producing a distribution known as Bragg peak. This feature allows the maximum deposition to the prescribed depth by adjusting the initial energy of the proton beam.

Proton radiation therapy requires precise knowledge and consistency of the patient's anatomy to ensure accurate dose delivery. Currently, proton treatment plans are created using X-ray computed tomography (CT) images. However, errors in the Hounsfield units (HU) to relative stopping power (RSP) conversion, unexpected changes in anatomy, or misalignments of the patient with respect to the proton beam can cause overdosing of healthy tissues surrounding the tumor or underdosing of the tumor volume [3].

Proton computed tomography (pCT) plays an important role in medical physics and imaging because it allows a direct calculation of the RSP from proton energy loss measurements. The idea of using pCT for proton-therapy treatment planning was initially studied in the 60's, and recently, it has become an important topic to exploit its potential and its validity as an imaging technique. Not only the dose delivered using protons is considerably lower than the one delivered by X-rays to obtain comparable images, but the use of protons in imaging techniques (proton radiography and pCT) represent a control tool for the Hounsfield Units to Relative Stopping Power (HU-RSP) calibration curve and a direct way of generating the RSP maps that would reduce the uncertainties of proton ranges to less than 1% [4].

The goal of this work was to test the capabilities of the pCT scanner prototype developed at IEM-CSIC to image different planar structures of volumetric phantoms using proton beams of different energies at the Cyclotron Centre Bronowice in Krakow, Poland. The pCT scanner prototype design included two components: a tracking system composed by two double-sided silicon strip detectors of 1000μm, and a residual energy detector, the detector CEPA4 that offers fast response and good energy resolutions for both, gamma rays and protons.

This work was included in the activities carried out in the Experimental Nuclear Physics Group of the *Instituto de Estructura de la Materia*, a department of the *Consejo Superior de Investigaciones Científicas*, in the framework of the project "Proton therapy and Nuclear Techniques for Oncology" (PRONTO) funded by the local government of Madrid, with reference B2017/BMD-3888 [5].

After the theoretical fundamentals and an overview on pCT (chapter 2), the methodology of this experiment, including the pCT scanner prototype description is included in detail in chapter 3. The analysis algorithms are also presented (chapter 4). Chapter 5 presents the evaluation of the quality of the planar image reconstruction achieved using the pCT scanner prototype together with a comparison of the simulated planar images developed by C. Ballesteros in his Master thesis [6].

Chapter 2

Theoretical background

This chapter summarizes the fundamentals of the interaction of radiation with matter and the modalities of radiation therapy, focusing on the advantages of proton therapy and its treatment planning. The development, current status, and limitations of proton computed tomography technologies are also included.

2.1 Interaction of radiation with matter

The term radiation applies to the emission and propagation of energy through space or materials. When the energy is sufficient to ionize atoms or molecules, it is called ionizing radiation. Ionizing radiation can be divided into directly and indirectly ionizing radiation. Charged particles such as electrons, protons, and alpha particles are known as directly ionizing radiation because, in case they have enough kinetic energy, can directly produce ionization by collisions with atoms as they penetrate matter. As neutrons and photons, the uncharged particles are called indirectly ionizing radiation because they liberate directly ionizing particles from matter when they interact with matter [7].

2.1.1 Photons

Ionizing photons interact with the atoms of a material to produce high-speed electrons by three major processes: photoelectric effect, Compton effect, and pair production.

Photoelectric effect is a phenomenon where a photon interacts with an atom and ejects one of the orbital electrons from the atom. In the process, the photon energy is first fully absorbed by the atom and then transmitted to the ejected electron. An illustration of the photoelectric effect is shown in Fig. 2.1(a).

Compton effect, the photon interacts with an atomic electron as if it were a "free" electron. Fig. 2.1(b) shows this process. The electron receives some energy from the photon and is emitted at an angle θ, while the photon is scattered with reduced energy at an angle ϕ.

Pair production is an interaction mechanism that can only occur if the energy of the photon is greater than 1.022 MeV. The photon interacts with the atomic nucleus and gives up all its energy, generating a pair electron-positron, as it can be seen in Fig. 2.1(c). Both the electron and the positron deposit their kinetic energy in the material. Near the end of the positron's range, it combines with one of the free electrons in its vicinity and generates two annihilation photons, each having 0.511 MeV energy.

Fig. 2.2 shows the relative importance of the three processes for different materials and different photon energies. The lines represent the energies at which photoelectric effect and Compton scattering, and Compton scattering and pair production are equally probable as a function of the atomic number of the materials [8].

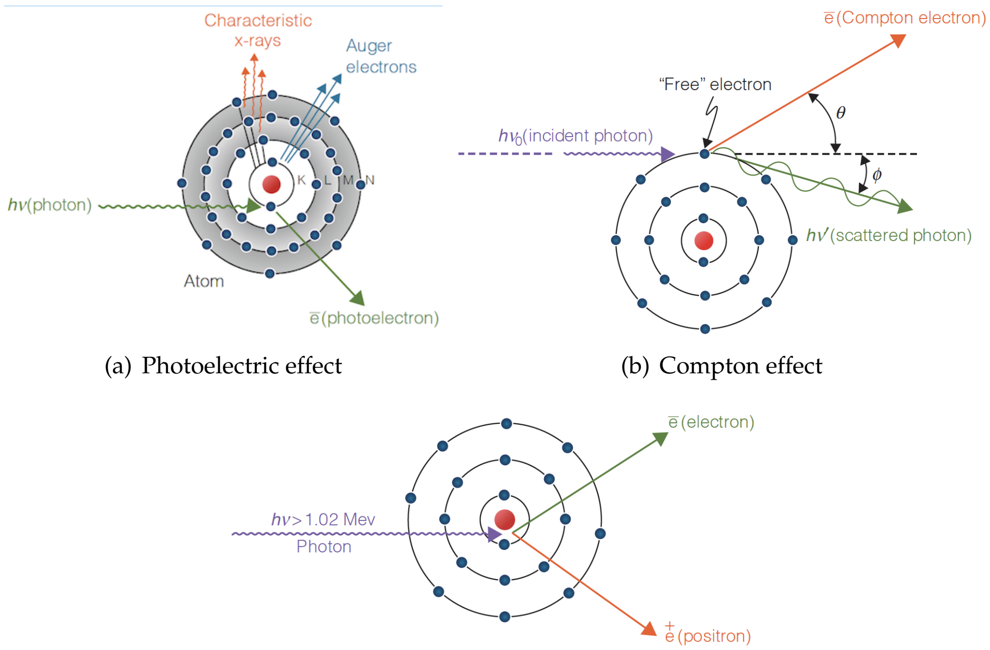

(a) Photoelectric effect

(b) Compton effect

(c) Pair production

FIGURE 2.1: Main types of interactions that cause the attenuation of a photon beam by an absorbing material. Images taken from [7].

The photoelectric effect predominates over the Compton effect at low photon energies. As the photon energy increases beyond the binding energy of the K electron, the probability of photoelectric effect decreases rapidly with energy, and the Compton effect becomes more and more relevant. However, this effect also decreases with increasing photon energy. The pair production is predominant for high-energy gamma rays. It presents a rapidly increasing probability with the atomic number of the absorber, and it also increases with the logarithm of the incident photon energy above the threshold energy [7].

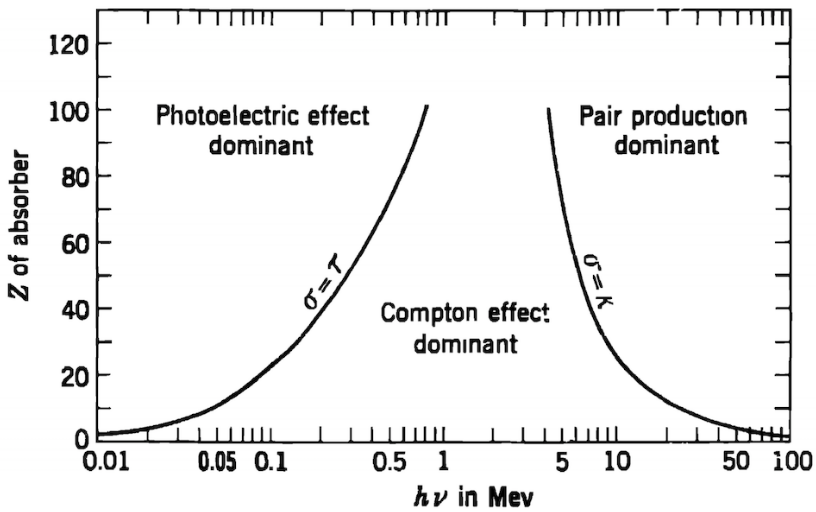

FIGURE 2.2: Relative importance of the three major types of interactions of photons with matter: photoelectric effect, Compton effect and pair production. Image taken from [9].

When a photon passes through a material, the probability that it will experience an interaction depends on its energy, and composition and thickness of the absorber. Fig. 2.3 shows the attenuation of a photon beam after passing through an absorber layer of thickness x. The number of photons after passing through the absorber ($N(x)$) is proportional to the number of incident photons (N_0) and to the thickness of the absorber (x). The following mathematical expression describes the attenuation of photon beam intensity:

$$N(x) = N_0 e^{-\mu x} \tag{2.1}$$

where μ is the constant of proportionality, called the linear attenuation coefficient of the absorber material [7, 10].

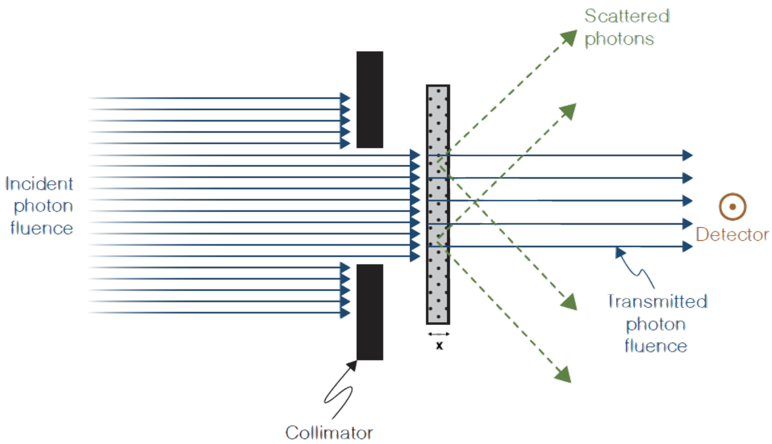

FIGURE 2.3: Photon beam attenuation with an absorber material with thickness x. Image taken from [7].

2.1.2 Charged particles

Charged particles interact mainly by ionization and excitation. Radiative collisions are possible, but they are much more likely for electrons than for heavier charged particles. The charged particle interactions are mediated by Coulomb force between the electric field of the traveling particle and electric fields of orbital electrons and nuclei of atoms of the material. Collisions between the particle and the atomic electrons result in ionization and excitation of the atoms. Collisions between the particle and the nucleus result in radiative loss of energy. Particles also suffer scattering without significant loss of energy [7].

Charged particles are characterized by a definite range in a given absorber material. The range represents a distance beyond which no particles will penetrate. The products of these encounters in the absorber are either excited atoms or ion pairs. Ion pairs usually do not appear as randomly spaced single ionizations. However, there is a tendency to form many clusters of multiple ion pairs distributed along the particle's track. [8].

The predominant interactions of protons in the matter are Coulomb interactions with atomic electrons, Coulomb interactions with atomic nuclei, and nuclear reactions. Protons continuously lose energy as they pass through a medium due to inelastic Coulomb interaction with the atomic electrons. The amount of energy loss per collision is only a small fraction of the total energy due to the huge difference in the mass of protons and electrons. The amount of deflection is also negligible; thus, it is generally assumed that most protons travel nearly on a straight line. In contrast, a proton passing near the atomic nucleus will experience a repulsive elastic Coulomb interaction with the protons in the nucleus and it will be deflected from its original trajectory. Additionally, while traversing a material, this process can occur a number of times known as Multiple Coulomb Scattering (MCS) which causes a non-negligible macroscopic deflection. There is a significant deflection due to the large mass of the atomic nucleus. When the incoming proton projectile enters the nucleus, several processes may occur. The interaction of protons with the nucleus through nuclear reactions may produce secondary protons and heavy ions, neutrons, and gamma rays [11].

The rate of energy loss per unit path length or stopping power caused by ionization interactions for charged particles is proportional to the square of the particle charge and inversely proportional to the square of its velocity. Thus, as the particle slows down, its rate of energy loss increases, and so does the ionization or absorbed dose by the medium. As it can be seen in Fig. 2.4, the dose deposited in water increases at first very slowly with depth and then very sharply near the end of the range, before dropping to an almost zero value. This peaking of dose near the end of the particle range is called the Bragg peak [7].

The rate of energy loss, or linear stopping power, is defined as the quotient of the mean energy loss dE over a distance dx. It is usually expressed independently of the density of the material ρ as the mass stopping power expressed as:

$$\frac{S}{\rho} = -\frac{dE}{\rho dx} \tag{2.2}$$

A more accurate way of expressing the mass stopping power takes into account quantum mechanical effects and corrections. This equation is known as the Bethe-Bloch equation, named after Hans Bethe and Felix Bloch, and is expressed as

$$\frac{S}{\rho} = -\frac{dE}{\rho dx} = 4\pi N_A r_e^2 m_e c^2 \frac{Z}{A}\frac{z^2}{\beta^2}\left[ln\frac{2m_e c^2\gamma^2\beta^2}{I} - \beta^2 - \frac{\delta}{2} - \frac{C}{Z}\right] \tag{2.3}$$

where N_A is Avogadro's number, r_e is the classical electron radius, $m_e c^2$ is the mass of an electron, z is the charge of the incoming projectile (proton), Z is the atomic number of the absorbing material, A is the atomic weight of the absorbing material, c is the speed of light, $\beta = v/c$ where v is the velocity of the projectile, $\gamma = (1-\beta^2)^{-\frac{1}{2}}$, I is the mean excitation potential of the absorbing material, δ is the density correction parameter, and C is the shell correction parameter. The density and shell corrections need to be considered for very high or very low proton energy ranges [11].

The pristine Bragg peak shows the maximum dose near the end of range of the charged particle. The physical processes governing the location and height of the peak are mainly the proton stopping power and energy straggling, and nuclear reactions to a much lesser extent. A pristine proton peak is shown in Fig. 2.4. In order of increasing depth, the regions of the Bragg peak are electronic buildup, protonic buildup, subpeak, peak, and distal falloff [11].

- **Electronic buildup region:** it is a small region near the surface of the absorber where the proton beam is incident.

- **Protonic buildup region:** it is a region near the surface of the absorber where the absorbed dose increases with depth because of the buildup of secondary protons that appear due to proton-induced non-elastic nuclear interactions.

- **Sub-peak region:** it is the region extended from the surface of the absorber to the proximal depth of the peak. The physical processes involved here are, in decreasing order of importance, the stopping power's dependence on the inverse-square of the proton velocity, the removal of some protons by nuclear reactions, the liberation of secondary particles from nuclear reactions, and for very small fields, the accumulation of lateral deflections from MCS leading to lateral protonic disequilibrium and reduction of the proton fluence on the central axis.

- **Bragg peak:** is the maximum dose near the end of range. The processes that govern the location or height of the peak are mainly the proton stopping power and energy straggling, nuclear reactions to a much lesser extent and, for very small fields, MCS.

- **Distal falloff region:** this region extends from depths greater than that of the pristine Bragg peak depth, z_{BP}.

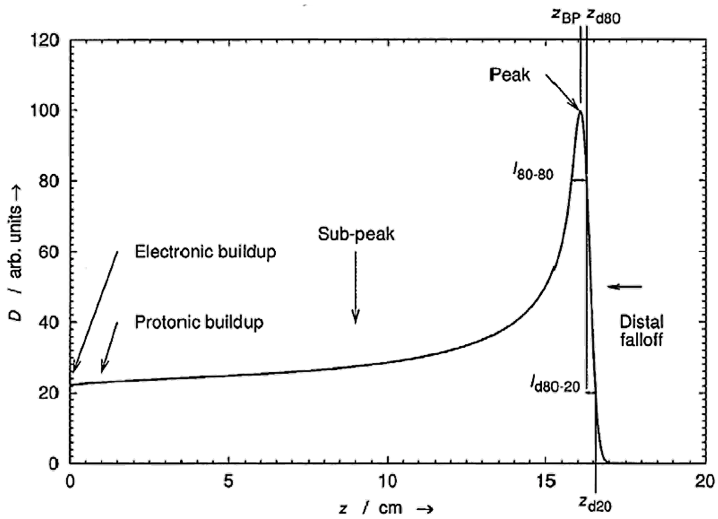

FIGURE 2.4: Absorbed dose D as a function of depth z in water from a pristine proton Bragg peak produced by a broad proton beam with an initial energy of 154 MeV. Image taken from [11]

Some characteristic lengths are the 80%-to-20% distal-falloff length (l_{d80-20}) and the proximal-80%-to-distal-80% pristine-peak width (l_{80-20}) that represent the distances between the distal-80% and distal-20% depths, and the the proximal-80% and distal-80%, respectively. These definitions help to characterize Bragg peaks in clinical and research settings [11].

2.2 Modalities of radiation therapy

Radiation therapy has been widely used in the management of cancers, and it has become one of the primary modalities for cancer patient treatment. Three-dimensional conformal radiation therapy and intensity-modulated radiation therapy have been developed and applied in clinics. These techniques represent a standard tool in cancer treatment because they concentrate irradiation doses on the tumor while sparing the adjacent normal tissues and organs [12]. However, the improvement in the benefits of radiation therapy mostly comes from the dose conformation of photons, which are the main source of radiation therapy currently in use, rather than their radiobiological effectiveness [13].

Charged particle beams such as protons offer many advantages compared to any modality of conventional radiotherapy with X-rays due to their different interaction mechanisms with matter. The dose applied by proton beams is deposited in precise areas with a minimal lateral scattering in tissue, reducing the irradiation to the healthy tissue that surrounds the tumor. Protons' limited range and high linear energy transfer at the end of their range make them preferentially applied in treating tumors located near critical structures such as the spinal cord, eyes, and brain, and in pediatric malignancies. Relative biological effectiveness (RBE) is a value used to account for differences in radiobiological effects between photons and other particles employed for radiation treatments. For clinical patient treatment, a constant RBE of 1.1 is currently used for protons [14]. Clinical proton beams provide distributions of doses superior to those achievable by the highest technology photon beams due to their physical properties [15]. Fig. 2.5(a) shows a spread-out Bragg peak (SOBP), compared with a 15 MV X-ray beam for dose depth on the central axis. The SOBP is a clinical beam whose energy is spread to conform to the target, achieving a maximal and approximately constant dose deposition over the whole dimension of the tumors. Cross-section views of the dose depths are shown in Fig. 2.5(b). Proton beams deliver a near-zero dose at depths beyond the target for each proton beam path, leading to a finite dose distribution contained within the target volume, contrary to what is observed for photon beams.

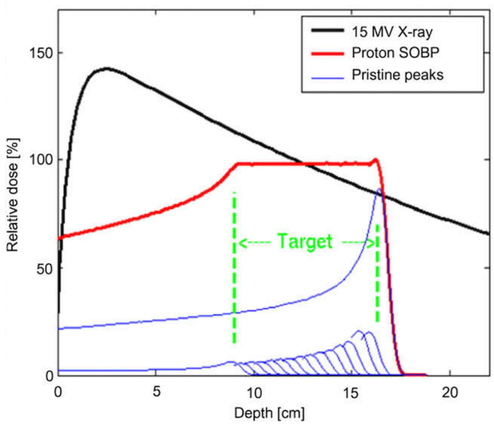

(a) Central axis depth dose curves for a 150 MeV proton beam with a 7 cm SOBP, and a 15 MV X-ray beam. beam

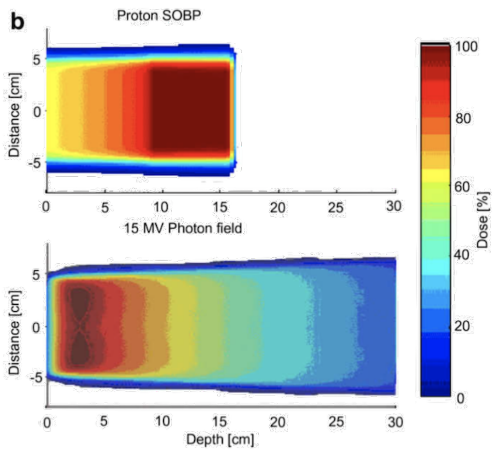

(b) Cross section of dose vs depth for a 150 MeV proton beam with a 7 cm SOBP and for a 15 MV X-ray beam

FIGURE 2.5: Comparison of a 150 MeV proton beam with a 7 cm SOBP, and a 15 MV X-ray beam. a) depth dose curves. b) Cross section of dose vs depth. Images taken from [15].

As observed in Fig. 2.5, in conventional radiotherapy, most of the energy is deposited at the entrance, and the photons keep depositing energy along a range in depth; these cause a high dose deposition in the healthy tissue of the patients. On the contrary, the ion energy can be tuned such that the ions stop in the tumor, resulting in a minimal dose proximal to the tumor and nearly zero doses distal to the tumor. The use of ion beams is beneficial to the patients because they reduce the deposited doses to surrounding healthy tissue and the probability of secondary cancers [4, 16].

2.3 Proton therapy treatment planning

Proton radiation therapy delivers a conformal dose to a target volume in a patient. This requires precise knowledge and consistency of the patient's anatomy to ensure accurate dose delivery. Medical physicists currently create proton treatment plans using X-ray computed tomography (CT) images, which assume that the patient anatomy remains constant during all treatment fractions. However, errors in the Hounsfield units (HU) to relative stopping power (RSP) conversion, unexpected changes in anatomy, or misalignments of the patient with respect to the proton beam can cause overdosing of healthy tissues surrounding the tumor or underdosing of the tumor volume [3].

Proton therapy effectiveness depends on the accuracy and precision of both the treatment planning and the proton beam delivery. Nowadays, for both photons and protons therapy, the patient treatment is based on X-ray CT images, which consist of a map of Hounsfield unit (HU) values. The HU is a relative measurement of the attenuation coefficient of the materials that is used to interpret CT images, and it is obtained using Eq. 2.4:

$$HU = 100\left(\frac{\mu - \mu_{water}}{\mu_{water} - \mu_{air}}\right) \tag{2.4}$$

where μ is the average linear attenuation coefficient in a voxel, μ_{air} and μ_{water} are the linear attenuation coefficients of air and water, respectively.

Each X-ray CT scanner is characterized by its calibration curve to convert the HU values into electron density of known materials with acceptable accuracy. The RSP corresponds to the stopping power of a specific material ($S_{material}$) relative to water (S_{water}) as shown in Eq. 2.5. For proton therapy purposes, a map of the proton RSP is necessary.

$$RSP = \frac{S_{material}}{S_{water}} \tag{2.5}$$

A problem with this approach is that X-rays interact very differently with materials compared with protons, resulting in relations between HU and RSP that are not unique, and can therefore be ambiguous [4].

Theoretical and experimental approaches were investigated to get a RSP map from an X-ray CT image. The theoretical relationship between RSP and HU values was not easily formulated, and the accuracy of $\pm 5\%$ was not clinically acceptable. The different dependence of the energy deposition on Z and Z/A of protons and photons, respectively, results in a non-unique correspondence between RSP and HU, causing uncertainties in the proton range estimation. The stoichiometric method and the polybinary calibration are two experimental approaches that are currently used and give proton range uncertainties around 1% to 3% [16]. The RSP sources of error were classified into five categories:

1. Uncertainties from CT imaging.
2. Uncertainties in the stoichiometric formula used to calculate the theoretical CT numbers.
3. Uncertainties in the human tissue composition.
4. Uncertainties in the mean excitation energies used in the Bethe-Bloch equation.
5. Uncertainties due to RSP proton energy dependence not taken into account by dose algorithms.

The increase of proton scattering in heterogeneous organs results in more critical uncertainties on the RSP than those obtained for homogeneous tissues. At the interface between two materials with different stopping powers, problems as dose perturbation and Bragg peak degradation are observed [16].

The direct use of X-ray CT for proton therapy treatment planning does not constitute the best approach due to the different interaction processes between photons and protons. Protons have a dose distribution that is contained within the target volume due to their finite range in the matter, while photons are attenuated, and they keep depositing energy along a range in depth [17].

Accurate RSP maps assure better proton therapy treatment plans. Proton computed tomography (pCT) plays an essential role in medical physics and imaging because it allows a direct calculation of the RSP from proton energy loss measurements, allowing more accurate proton therapy treatment planning. At the same time it has been reported that a 6 min pCT scan produced a good CT image and caused a dose of 1.4 mGy, corresponding to doses of 2.8% to 4.6% of the doses typically delivered by an X-ray CT scan of the head [4].

2.4 Proton computed tomography overview

The idea of using pCT for proton-therapy treatment planning was initially studied in the 60's decade. In 1963 Allan Corkmack proposed using the energy loss of charged particles to determine the variable density of matter with constant chemical composition. Andrew Koehler presented the first example of the use of energetic protons for radiographic purposes at Harvard cyclotron and emphasized a higher contrast in proton radiography than the X-rays radiography of human tissues with tumors [4, 16]. During that decade and the next one, important advances were performed.

- Goiten performed in 1972, the first heavy particle tomographical reconstruction at LBL Cyclotron in Berkeley, California, U.S.A. [16].
- Cormack and Koehler participated in the first laboratory implementation of pCT in 1975, using a 158-MeV pencil beam to image a phantom with small density variations [4].
- In the late 1970s and early 1980s proton tomography was extensively investigated at Los Alamos Meson Physics Facility (LAMPF) in New Mexico by Ken Hanson *et al.* In 1978 and 1979, a 29-cm and a 19-cm diameter phantom were scanned with 240 MeV and 192 MeV proton beams, respectively. The phantoms had different materials and densities inserted and were both reconstructed using the filtered back-projection (FBP) algorithm. In 1981, the dosimetric advantage of pCT was demonstrated, and the first pCT scan of humans organs was performed [16].

Despite the lack of technology available to fully exploit the potential of pCT, its validity as an imaging technique was spread worldwide thanks to the contribution of the LAMPF group. Since 1994, the use of proton radiography as a control tool for the HU-RSP calibration curve in proton therapy has been studied, and in 2004, Schneider *et al.* performed the first proton radiography on an a dog to prove the dosimetric advantages of proton radiography. It was proven that the dose delivered using protons was 50 to 100 times lower than the one necessary to obtain a comparable image using X-rays [16].

2.5 Current status of proton computed tomography

The pCT is based on the energy loss measurement of individual protons traversing the scanned object. The existing prototypes consist of two main components: a proton tracking system and a residual energy detector. The scanned objects are placed at the center between the front and rear tracking planes, and they are rotated along the vertical axis, as shown in Fig. 2.6 during the tomography scan.

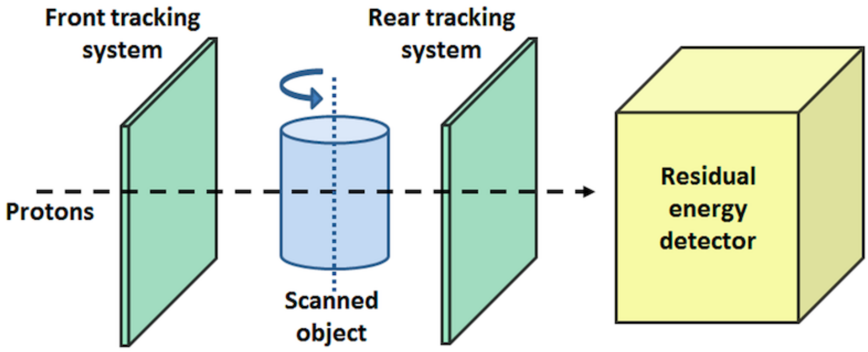

FIGURE 2.6: Schematic representation of the pCT scanner prototypes components; proton tracking system (in green), residual energy detector (in yellow) and scanned object (in blue). Image taken from [16].

There are several efforts to build prototype pCT systems of the type described in Fig. 2.6, which are listed in Table 2.1. All consist of a combination of tracking detectors and an energy or range detector, but not all use the same detector technologies. There are also recent efforts to build similar systems that are restricted to proton radiography. Even in cases when pCT is not needed, information on particle tracking before and after the phantom can be used to improve the spatial resolution of proton radiography greatly. Therefore, an optimal proton radiography detector system may be very similar to a system designed for pCT with the advantage of producing an image in seconds instead of minutes [4].

TABLE 2.1: List of some efforts on prototype pCT systems and particle radiography (pRad) systems with particle tracking. List taken from [4].

Collaboration	**Type**	**Aperture** (cm^2)	**Tracking technology**	**Residual energy detector**	**Acquisition rate**
AQUA	pRad	10×10	GEM	Scint. range counter	10 kHz
LLU/UCSC phase-II	pCT	36×9	Si strip	5 scint. stages	1.2 MHz
Niigata	pCT	9×9	Si strip	NaI calorimeter	30 Hz
NIU, FNAL	pCT	24×20	Sci Fi	Scint. range counter	2 MHz
PRaVDA	pCT	4.8×4.8	Si strip	CMOS APS telescope	2.5 MHz
PRIME	pCT	5.1×5.1	Si strip	YAG:Ce calorimeter	10 kHz
PSI	pRad	22.0×3.2	Sci Fi	Scint. range counter	1 MHz
QBeRT	pRad	9×9	Sci Fi	Sci Fi range counter	1 MHz

2.5.1 The pCT Scanner Prototype at IEM-CSIC

The design of the pCT scanner prototype included the development of Monte Carlo simulations and experimental tests of the first prototype. This work was presented by V.G. Távora [17] and M.I. Posadillo [18] in their respective Master theses defended in 2019.

Two double-sided silicon strip detectors (DSSSDs) constituted the initial design of the pCT scanner prototype developed at IEM-CSIC, as it can be seen in Fig. 2.7(a). This prototype was tested at the *Centro de Microanálisis de Materiales* (CMAM) in Madrid. Fig. 2.7(b) shows the estimated energy of the protons that impinge on each of the element that compose the system, as well as the dimensions of each element. The maximum proton beam energy available in the facility was 10 MeV. The function of the first DSSSD was to track the position on which the protons impinged on the sample. The second DSSSD was used as both tracker and residual energy detector because the thickness of this detector stopped the protons that passed through the phantom.

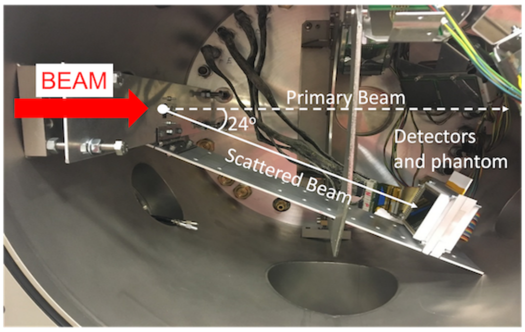

(a) Experimental setup of the first experiment performed at CMAM.

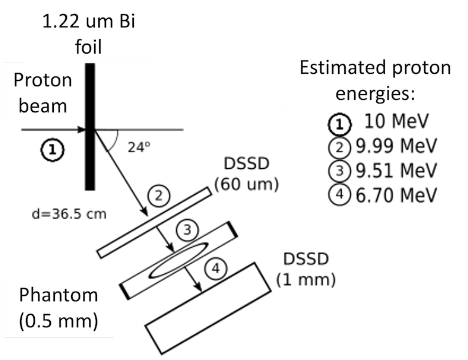

(b) Detailed scheme of the setup.

FIGURE 2.7: Experimental setup of the first experiment performed at CMAM (a) Experimental, (b) Detailed scheme of the setup showing the thickness of the detectors and the estimated energy of the protons that reach the system components. Images modified from [18].

Fig. 2.8 shows the different phantoms made of PVC and aluminum that were studied. In the upper part, the designs are shown, while the four inferior images are the real phantoms used in the experiment.

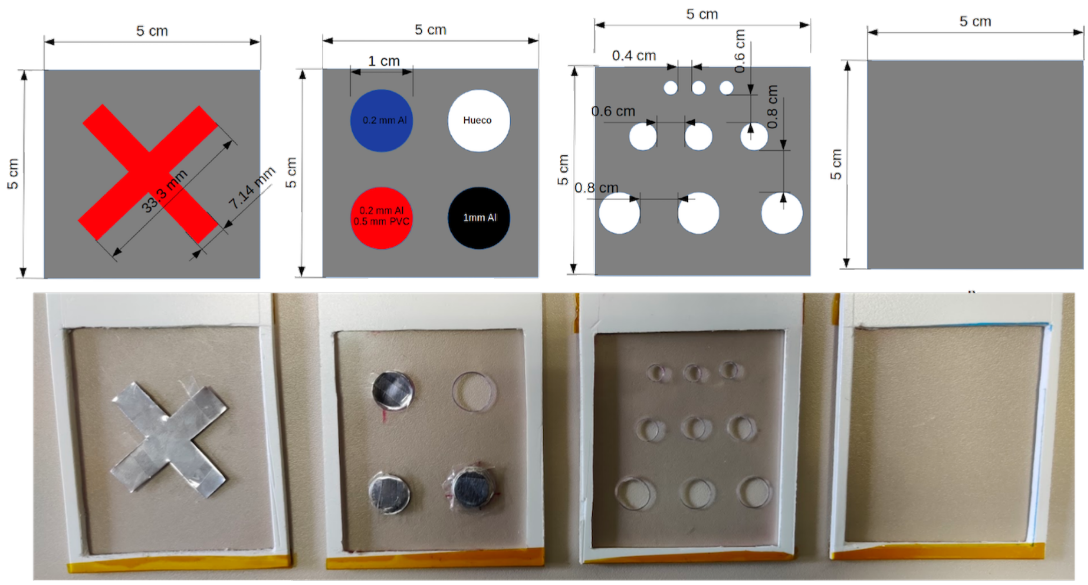

FIGURE 2.8: Design of the different phantoms used in the CMAM experiment. Images taken from [17].

The goals of this experiment were:

- The determination of the energy deposited on the phantoms to reconstruct a structure of known dimensions.
- The differentiation of materials from the energy deposited on them.
- The study of the spatial resolution of the prototype.

The data analysis allowed the reconstruction of the images in the phantom plane for all the phantoms. Fig. 2.9 shows the simulated and experimental results obtained for the experiment that was performed at CMAM. The identification of shapes and materials was possible with the use of proton beams. A good agreement between the experimental and simulated results was observed despite the technical difficulties that the DSSSDs presented.

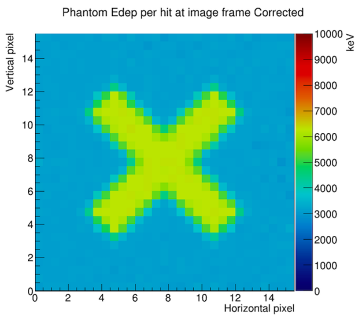

(a) Simulated cross phantom

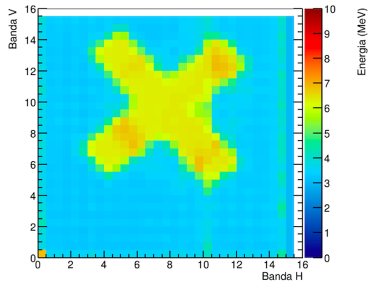

(b) Experimental cross phantom

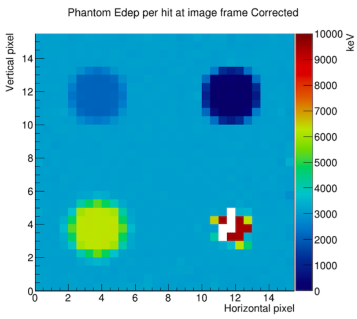

(c) Simulated 4 regions phantom

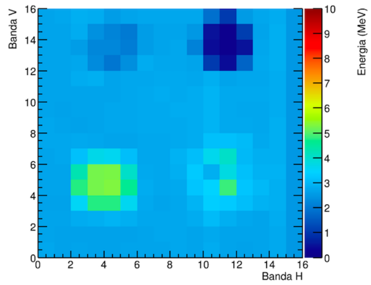

(d) Experimental 4 regions phantom

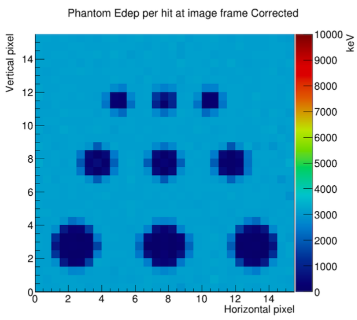

(e) Simulated Derenzo-type phantom

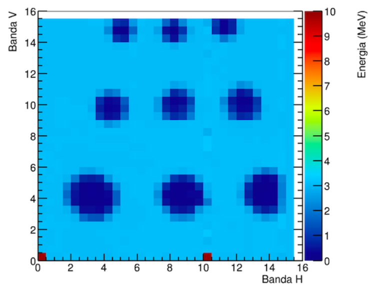

(f) Experimental Derenzo-type phantom

FIGURE 2.9: Simulated and experimental 2D plots of the energy lost per hit on the different phantoms imaged at the CMAM facility in 2019. Images (a), (c), (e) taken from [17], and (b), (d), (f) from [18].

The first pCT scanner design proved the possibility of realizing 2D-imaging of thin phantoms made of a PVC matrix of 500 μm thickness and up to 1 mm of aluminum. To work in a real case and image three-dimensional structures, the CEPA4 detector was considered an excellent candidate to be used as the residual energy detector of the pCT prototype due to its capability to stop protons with energies up to 200 MeV providing good energy resolution with a fast response [19]. The proposed experimental setup for this experiment is shown in Fig. 2.10. This setup included two DSSSDs, for particle tracking and the CEPA4 detector, to measure the residual energy of the protons [17].

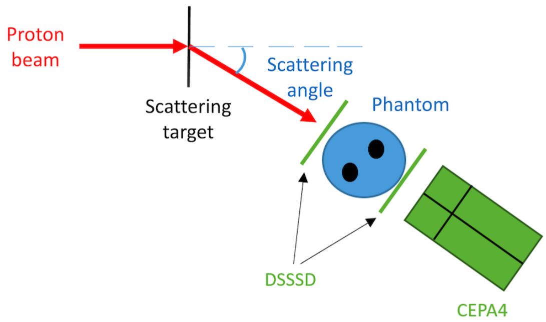

FIGURE 2.10: Proposed experimental setup of the CEPA4 experiment. Image modified from [17].

The main goal of the design of this experiment was to perform Monte Carlo simulations concerning the geometry and interactions of the pCT prototype to evaluate the possible results of the actual experiment and define the initial parameters of the experimental setup. Simulations using a cylindrical phantom of 5-cm diameter made of poly (methyl methacrylate) (PMMA) with two inserts were included. In one case the inserts were of alcohol and water and in the other air and water. The data analysis algorithms to obtain two-dimensional images in the phantom plane resulted in Fig. 2.11, where it is possible to differentiate between water (blue), alcohol (cyan), air (orange), and PMMA (red) [17].

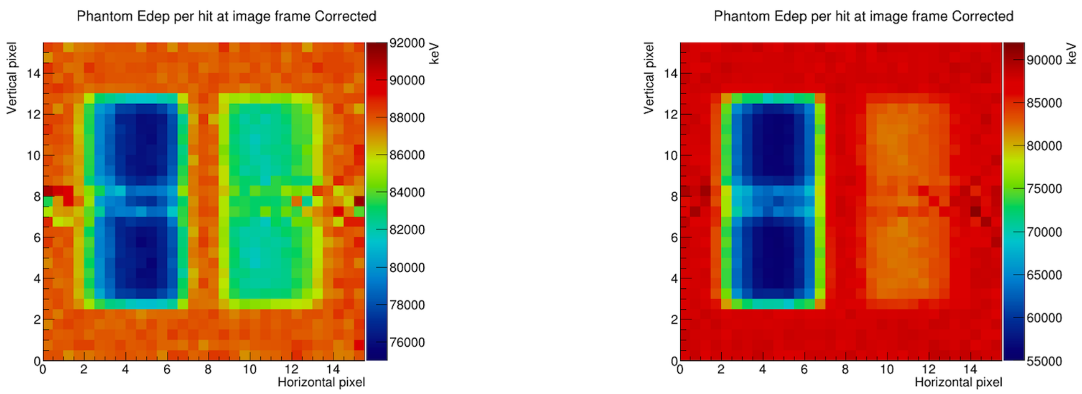

(a) Alcohol and water

(b) Air and water

FIGURE 2.11: Simulated two-dimensional plots of the energy lost per hit on the cylindrical phantom with water/alcohol and water/air imaged with a 100 MeV proton beam. Images taken from [17].

.

The results of the work of V.G. Távora assured the viability of the experiment presented in this document.

2.5.2 Limitations in proton computed tomography

Although the economic aspect plays a significant role in the pCT clinical development, it is not the only type of limitation that pCT presents at the moment.

The main **physical limitations** come from the proton's energy loss fluctuations and the scatter of protons that pass through matter. The energy loss fluctuations cause the stopping location not to be the same and make the proton range to be slightly variable. This phenomenon is known as energy straggling, and it affects pCT density resolution. The spatial resolution of pCT is negatively affected by the small multiple angular and lateral deflection that protons suffer when traversing a medium because of the electromagnetic interactions with the atomic nuclei of the material traversed. This mechanism is known as Multiple Coulomb Scattering. On the other hand, the nuclear interactions are not a limiting factor because their contribution is negligible in the relevant energy range for pCT, that is, between 100 MeV and 250 MeV [4, 16].

The **economic aspect** also needs to be considered because the use of pCT is strongly affected by the costs of medical facilities that use protons for treatment purposes. The use of proton therapy treatment facilities is not an accessible option due to the slow acceptance of this treatment modality. This is mainly due to construction problems, running costs, and lack of evidence of cost-competitiveness and cost-effectiveness. Even if proton therapy has advantages over conventional radiotherapy, from an economic point of view, more proof of proton therapy's effectiveness over IMRT is required [16].

Chapter 3

Experimental methods

In this chapter, a detailed description of the components of the pCT scanner prototype, and the preliminary tests of the prototype alongside their proposed configuration prior to conducting the experiment at the Cyclotron Centre Bronowice (CCB), Krakow, Poland, are presented. The final configuration of the prototype and the different phantoms that were imaged are also included.

3.1 The pCT scanner prototype developed at IEM-CSIC

The pCT scanner prototype developed at IEM-CSIC with its components is shown in Fig. 3.1. Protons with 90 - 120 MeV energy were tracked with double-sided silicon strip detectors (DSSSD) before entering the phantom and after passing through it. The residual energy of protons was measured with the cetector CEPA4, a phoswich array of $LaBr_3$(Ce)-$LaCl_3$(Ce) scintillators.

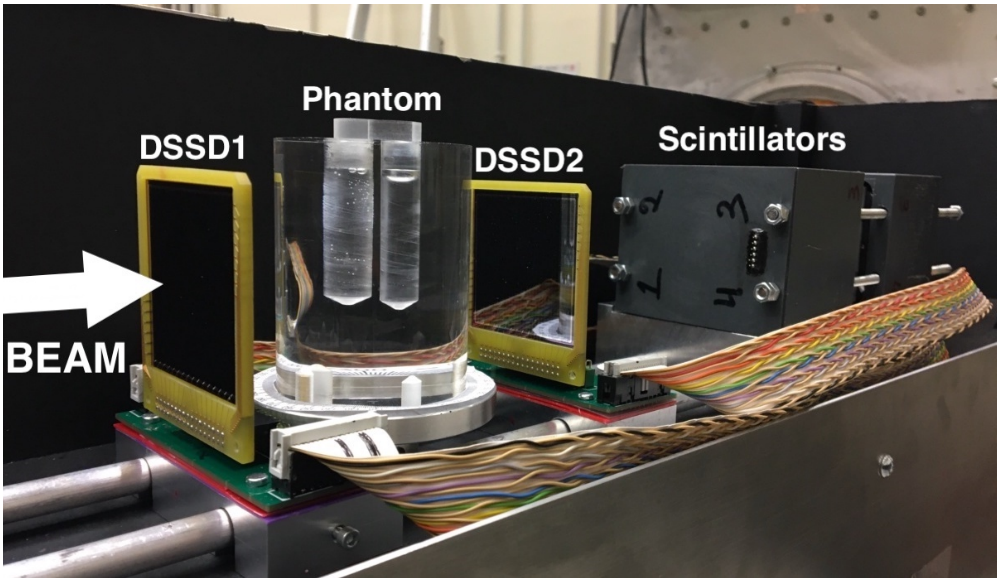

FIGURE 3.1: An image of the experimental setup of the pCT scanner prototype developed at IEM-CSIC mounted on a beam line of the Cyclotron Centre Bronowice in Krakow (Poland).

The first prototype was tested at the CMAM, in Madrid. The initial results were reported in the work of M.I. Posadillo [18]. The tests were performed with a proton beam of 10 MeV and included the analysis of thin phantoms made of 50 μm of PVC and aluminum up to 1 mm thickness. Two DSSSDs were used to determine the position and deposited energy of the particles on each detector. This initial experiment was a good starting point for developing the prototype to perform 2D imaging of different structures of homogeneous materials. On the other hand, the current prototype was tested at Cyclotron Centre Bronowice (CBB) in Krakow, Poland. The latter tests were performed with beam energies between 90 to 120 MeV. The incorporation of the CEPA4 detector to the prototype allowed the use of more energetic proton beams to perform 2D and 3D imaging of the volumetric phantoms presented on this work.

3.1.1 Tracking Detectors

The tracking detectors consisted of two DSSSD with thicknesses of 1000μm, and total active areas of 50 $\times$ 50 mm^2. On the front side, the active area was divided into 16 vertical strips of 3 $\times$ 50 mm^2 and 16 strips with similar characteristics oriented perpendicularly on the backside. This arrangement composed 256 pixels of 3 $\times$ 3 mm^2. A figure of a DSSSD can be seen in Fig. 3.2. The front and rear trackers were located symmetrically with respect to the rotation center of the phantom. Some advantages of the DSSSDs include their high performance, reliability, and stability [16]. Silicon detectors have a detection efficiency of nearly 100% for charged particles, and their calibration is simple and stable for many years.

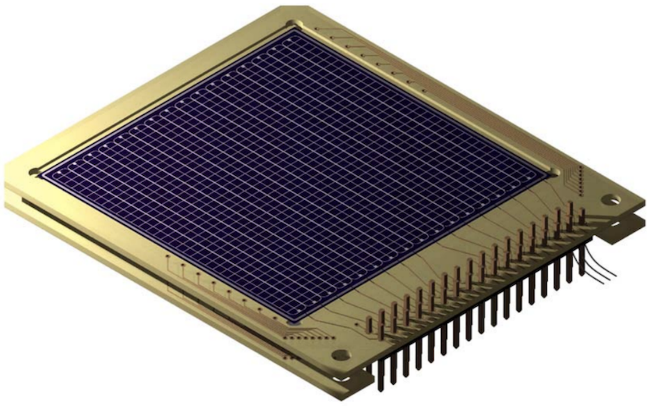

FIGURE 3.2: An image of a double-sided silicon strip detector. Image taken from [20].

3.1.2 Residual Energy Detector

The CEPA4 detector is a combination of 4 detectors which allows the reconstruction of the original energy of fast protons. Each detector is made of 4 cm of $LaBr_3(Ce)$ and 6 cm of $LaCl_3(Ce)$ in phoswich configuration coupled to a photomultiplier tube (PMT). The characteristics of the PMTs produced by Hamamatsu are displayed in Table 3.1. The detector was manufactured by Saint-Gobain and was tested using standard low-energy gamma sources, and high-energy proton beams [19].

TABLE 3.1: Parameters of the PMTs of the CEPA4 detector.

Crystal	Model	Stages	Outputs
1	R7600	10	2: anode and last dynode
2	R7600	10	2: anode and last dynode
3	R11187	8	2: anode and last dynode
4	R1187	6	1: anode

The decay constants of $LaBr_3(Ce)$ and $LaCl_3(Ce)$ are 16 and 28 ns, respectively [21]. The second layer crystal, $LaCl_3(Ce)$, is transparent to the light emitted by the first layer, $LaBr_3(Ce)$. Their corresponding wavelengths of maximum emission are of 380 nm for the $LaBr_3(Ce)$ and 350 nm for the $LaCl_3(Ce)$ [22]. Fig. 3.3(a) shows a picture of the CEPA4 detector on the configuration used for this experiment. A diagram of its components is shown Fig. 3.3(b). Due to its high performance, this detector has proven to be a good tool in proton spectroscopy, making it a fine instrument for designing the pCT scanner prototype.

(a) Image of the detector

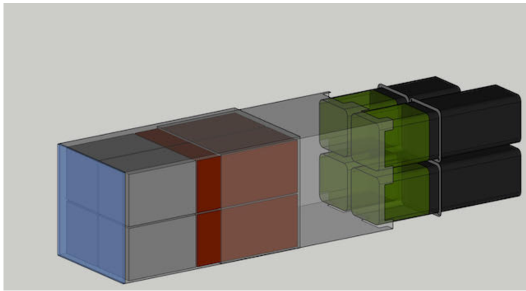

(b) Detailed scheme of the CEPA4

FIGURE 3.3: (a) An image of the CEPA4 detector taken at the Laboratory of Experimental Nuclear Physics of the IEM-CSIC (b)Detailed scheme of the CEPA4 detector. In red/gray one can see the squared prisms representing the phoswich units and the four photomultipliers tubes are at the left side in green there.

3.1.3 Data Read Out

The readout of the CEPA4 detector constituted the trigger of the pCT data acquisition system (DAQ). The number of the DSSSD, the strip number, and the energy deposited were registered for each proton detected by the CEPA4. The data acquisition was performed using the data acquisition software MVME (Mesytec Virtual Machine Environment), developed by Mesytec [23]. The DAQ provides basic data visualization and analysis capabilities, allowing calibration, accumulation, and visualization of data both during a data acquisition run or while replaying from a list file [24].

The signals from each DSSSD were digitized by a CAEN V785 analog-to-digital converter (ADC). On the other hand, the signals from the CEPA4 were digitized with the MDPP-16-QDC, a fast high-resolution time and amplitude digitizer. The events were built and then sent to the DAQ that writes all raw data to disk in "mvlclst" format. The files were read in hexadecimal format, and they were organized in 32-bit words. All data was stored in little-endian byte order. The first 32-bit word was a common header for all the files, indicating the endiannes of the file, shown as a solid red rectangle in Fig. 3.4(a). Each file was structured in frames of events with sub-frames of each analysis module within them. All the frames had headers that identified their type. Software-generated frames are called system event frames. These frames are used for transporting additional information, and they are displayed as red rectangles. A stack frame is shown in blue, and it marks the start of an event. Inside the stack frame, block read frames are shown in pink for the ADCs CAEN V785, orange for the digital pulse processor MDPP-16-QDC, and green for the TDC CAEN V1190A. Each event of the ADCs CAEN V785 consists of the header, data words, and the end of the block. The events of the MDPP-16-QDC consist of the header, data words (ADC, TDC, and the time stamp), and the end of the event. The events of the TDC CAEN V1190A consist of the header and the data words. A system event frame shown is shown in red. This frame's subtype is the end of the file and is written before closing the list file [25]. The files were read using a custom-designed C++ program and they were organized into root files. The structure of each root file is shown in Fig. 3.4(b). The root files were analyzed using ROOT, a software framework with building blocks for data processing, data analysis, data visualization, and data storage that is written mainly in C++ [26].

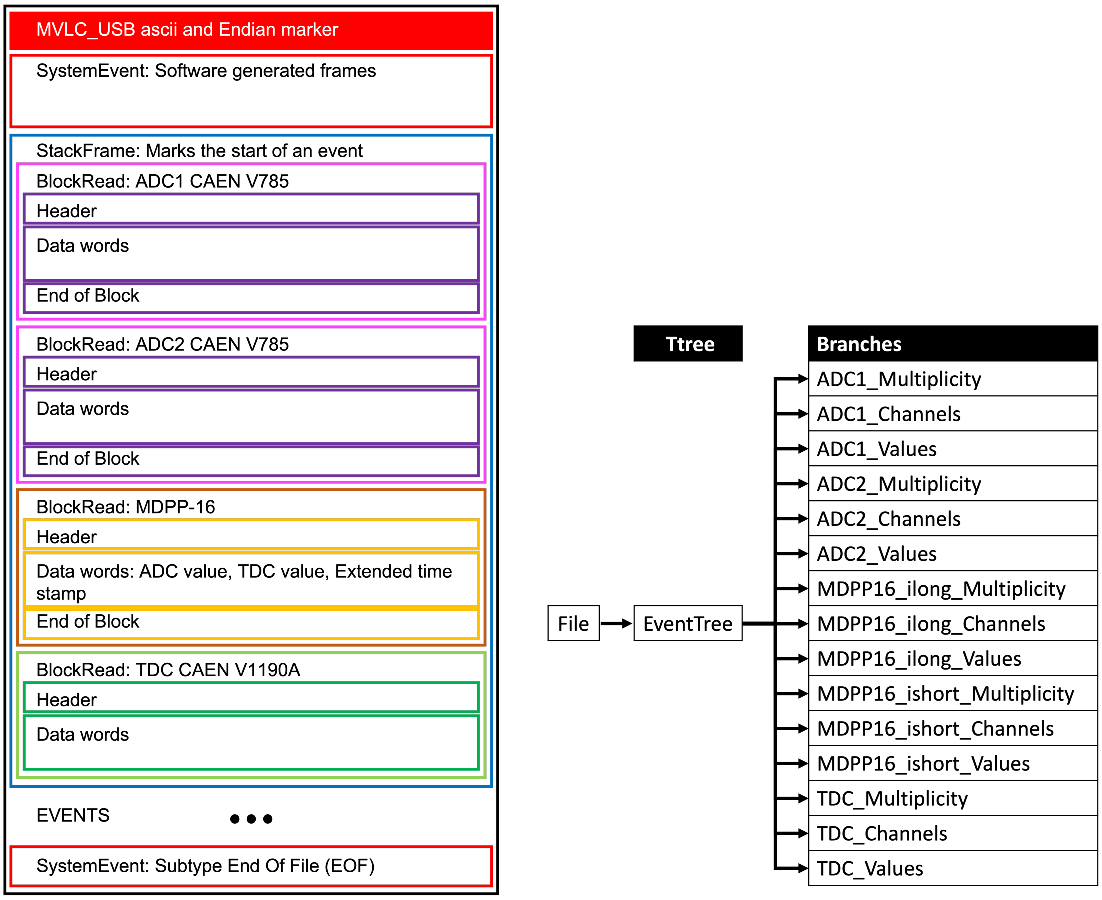

(a) Structure of the mvlclst files

(b) Structure of the root files

FIGURE 3.4: Structure of the files (a) Structure of the mvlclst files, (b) Structure of the root files.

The root files were built with the information of each detector. The structure of each root file consisted in a TTree and with fifteen branches arranged in order of detector, **first ADC** CAEN V785, **second ADC** CAEN V785, **long integration** and **short integration** of the MDPP-16-QDC, and **TDC** CAEN 1190A; for each detector, the branches are organized as follows:

- **Multiplicity of the detector**, corresponding to the number of detectors that were triggered in the event.
- **Triggered channels** that correspond to the position horizontal and vertical of the hit.
- **Energy deposited in the detector** expressed in channels for each detector.

3.2 Preliminary tests of the pCT scanner prototype at IEM-CSIC

The experimental setup was tested at the Laboratory of Experimental Nuclear Physics of the IEM-CSIC in two phases. In the first phase, the detectors and the data acquisition (DAQ) system were tested to guarantee a good performance. The second phase comprised the setting of the dynamic ranges for each detector and the test of the whole electronic chain for the experiment.

3.2.1 Test of the detectors and the DAQ system

Standard radioactive sources were used to carry out the tests of the detectors, and a pulser was used to test the performance of the DAQ system. The DSSSD could only be tested with alpha sources, for this reason the detector had to be placed inside a vacuum chamber, reducing the noise signals that reached the detector. The test of this detector was done using a standard alpha source of ^{148}Gd with energy of 3182.7 keV. On the other hand, the CEPA4 detector was placed in the air, and it was tested using a gamma source of ^{60}Co with energies of 1173 and 1332 keV.

The electronic chain for the previous experiment is described in Fig. 3.5. The blue boxes represent the shaping/timing filter amplifier modules STM-16+, the red box represents the CEPA4, the digital pulse processor module MDPP-16-QDC is enclosed in a green box, and the VME controller is marked with an orange box. The photomultiplier tubes (PMT) of the CEPA4 were connected to the voltage that was supplied in pairs. The PMTs of crystals 1 and 2 were connected to 555 V, and the PMTs of crystals 3 and 4 to 699 V. The DSSSD was placed at a pressure of 1.2×10^{-5} mbar. The voltage of the DSSSD corresponded to 30.5 V with a leakage current of 0.532 μA. The performance of the DAQ system was tested by "stressing" it with the use of a pulser that was connected simultaneously to the DSSSD's preamplifiers and to the module MDPP-16-QDC. The pulser was set at a constant amplitude of 0.08 V with positive polarity without attenuation and with variable pulse rates ranging from 100 Hz to 35 kHz. The system's response was checked by determining the FWHM, the peak centroid, and the integration of the peaks in the spectra of both detectors as a function of the variable pulse rates while setting the acquisition time of the data at 300 seconds in all the cases.

The study of both detectors was performed analyzing those channels that allowed the highest signal collection of the $\alpha-$particles emitted by the ^{148}Gd source. Central strips were selected in the P-side (P4) and N-side (N9) of the DSSSD. For the CEPA4, the third crystal was selected for the same reason. Fig. 3.6(a) displays the spectra measured with the strip P4 of the DSSSD when the pulser rate was set at 100 Hz, 2 kHz, 5 kHz, 7.5 kHz, 15 kHz, and 35 kHz. In order to observe the different peaks on the spectra, the counts (y axis) are shown on a logarithmic scale. From 100 Hz to 3 kHz, the detector response was similar, a peak centered around channel 1229 and a broader peak centered around channel 2939 were observed. The first peak observed in the spectra was associated with the signal of the pulser, while the last one was due to the $\alpha-$particles emitted by the ^{148} Gd source. As expected, for the former signal, the integral of the peak increased linearly with the pulse rate for all the tested values, whereas for the latter signal, the integral remained around 20000 counts per 300 seconds up to the measurement with the pulser at 10 kHz and then, it decreased to approximately 12000 counts at the highest test rate of 35 kHz for the same acquisition time. As expected, for the signal associated with the pulser, the integral of the peak increased linearly with the pulse rate for all the tested values, whereas for the signal related to the ^{148}Gd source, the integral remained around 20000 counts up to 10 kHz and then, it decreased to approximately 12000 counts at the highest test rate of 35

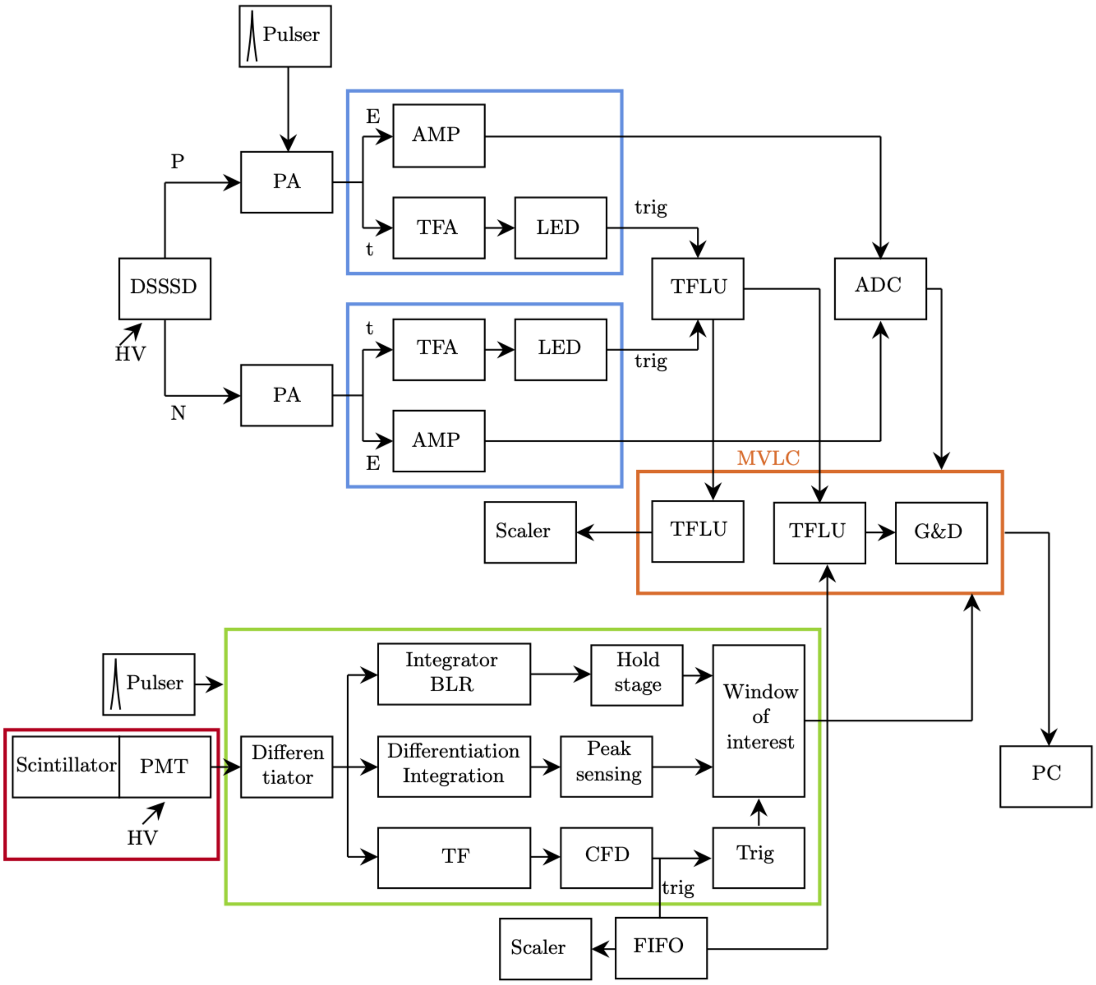

FIGURE 3.5: Electronic chain for the determination of the most suitable counting rate of the system for both detectors. The blue boxes represent the shaping/timing filter amplifier modules STM-16+, the red box represents the CEPA4, the green box represents the digital pulse processor module MDPP-16-QDC and the orange box represents the VME controller.

kHz. For pulse rates higher than 5 kHz a noise peak appeared at very low amplitudes, and the rest of the spectra were displaced. In general, the spectra measured with the DSSSD, showed a relatively constant behavior for pulse rates below 5 kHz, while the integral of the pulser peak increased linearly as a function of the pulse rate. For pulse rates larger than 5 kHz, the spectrum was shifted to larger amplitudes and it appeared a third peak at amplitudes below the channel 1000.

The peaks observed due to the decay of the ^{60}Co on the CEPA4 were studied for all its four detectors. The spectra of the $\beta - \gamma$ source measured with the CEPA4 was approximately constant for all the tests, Fig. 3.6(b) shows the spectra of the ^{60}Co when the pulse rate was set at 100 Hz and 35000 kHz. As the characterization of each peak yielded similar results for all four detectors, regardless of the value of the pulse rate, their average values were calculated, and those are reported in Table 3.2.

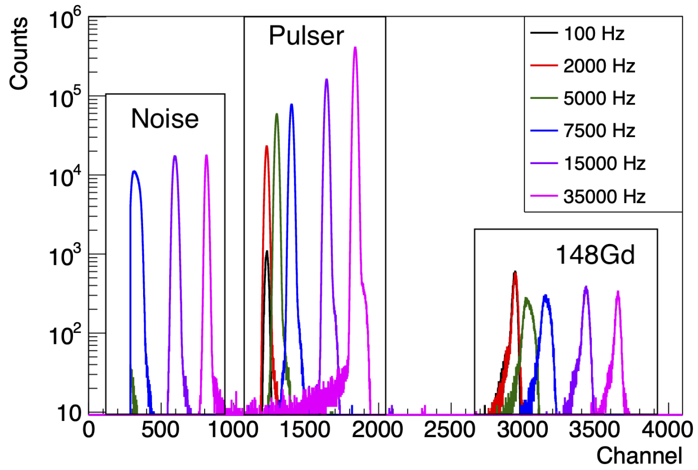

(a) Spectra of the pulser and the source of ^{148}Gd measured with the strip P4 of the DSSSD.

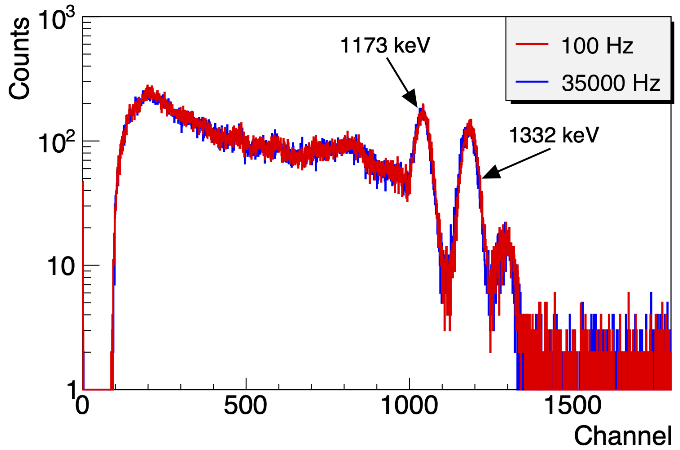

(b) Spectra of ^{60}Co measured with the detector 3 of the CEPA4.

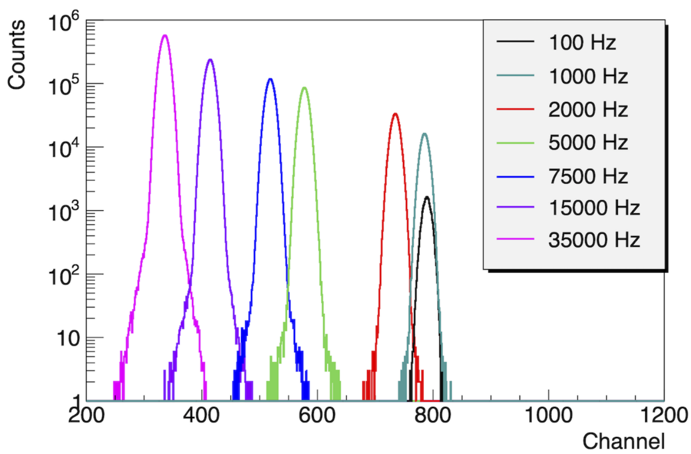

(c) Spectra of the pulser measured with MDPP-16-QDC.

FIGURE 3.6: Spectra obtained with the detectors for different pulse rates. (a) Strip P4 of DSSSD, (b) Crystal 3 of CEPA4, (c) Pulser measured with the module MDPP-16-QDC.

TABLE 3.2: Characterization of CEPA4 detector using a source of ^{60}Co.

	Peak of ^{60}Co at 1173 keV			Peak of ^{60}Co at 1332 keV		
Crystal	**Centroid** (channel)	**Resolution** (%)	**Area** (counts)	**Centroid** (channel)	**Resolution** (%)	**Area** (counts)
1	1256.1±2.2	1.60	7386±125	1428.1±2.7	1.36	5709±92
2	1286.5±2.9	1.47	6748±175	1463.2±3.4	1.33	5698±214
3	1037.6±1.3	2.13	8664±172	1182.2±1.6	1.75	6334±143
4	838.3±0.9	2.60	9194±258	955.6±1.2	2.15	6227±215

The signal of the pulser was also measured using the MDPP-16-QDC (green box in Fig. 3.5). The Fig. 3.6(c) shows the signal measured with this module for different pulse rates. The integrals of the pulser depended linearly of the pulse rate, as expected. The behavior of the centroids of the pulser was similar to the one observed in the DSSSD, a shift was observed to lower amplitudes, as it can be seen in Fig. 3.7. Even if the pulser signal was shifted, all the signals showed a FWHM almost constant.

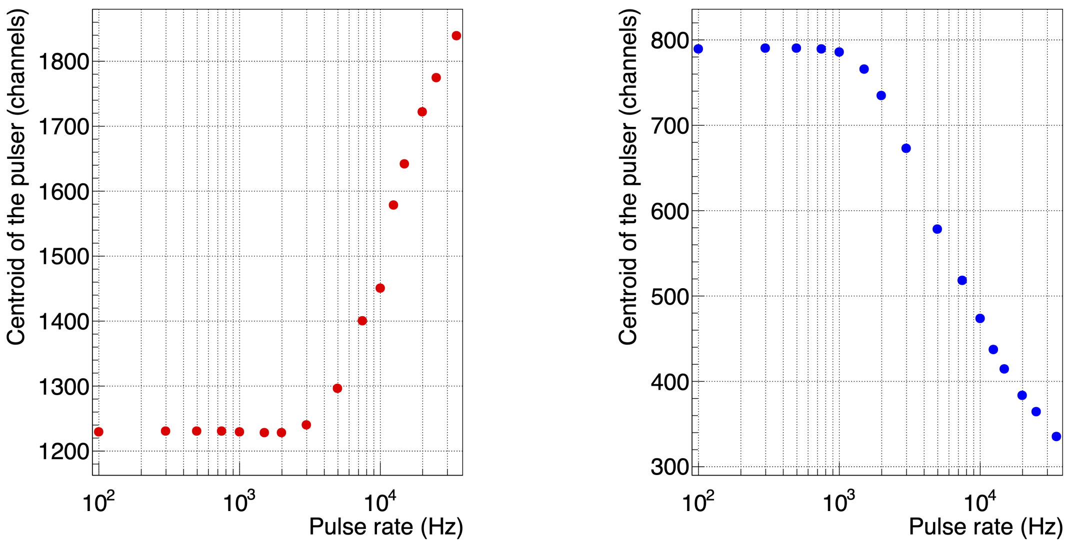

(a) ADC Caen 785

(b) MDPP-16-QDC

FIGURE 3.7: Centroid of the pulser signal shown as a function of the pulse rate. Values extracted from the spectra measured with (a) Strip P4 of DSSSD using ADC Caen-785, (b) MDPP-16-QDC.

For the DSSSD, at 3182.7 keV, the resolution of the strip N9 was 24.6 channels on average, and the centroid of the peak was around the channel 2924.4 for all the tested pulse rates; while for the strip P4, the behavior varied. Fig. 3.8 shows the resolution of the strip P4 for the tested pulse rates. For this strip, the resolution was almost constant for pulse rates below 5 kHz (approximately 31.4 channels), while for higher pulse rates, it increased.

The spectra measured with the DSSSD showed a relatively consistent behavior for pulse rates up to 3 kHz. The integral of the pulser peak increased while the integral of the ^{148}Gd peak remained at a constant value. The MDPP-16-QDC showed similar overall behavior for pulse rates below 3 kHz. The signal coming from the ^{60}Co also remained constant. The pulser signals measured with both detectors did not show any significant change in the FWHM. The main conclusion that can be drawn in this

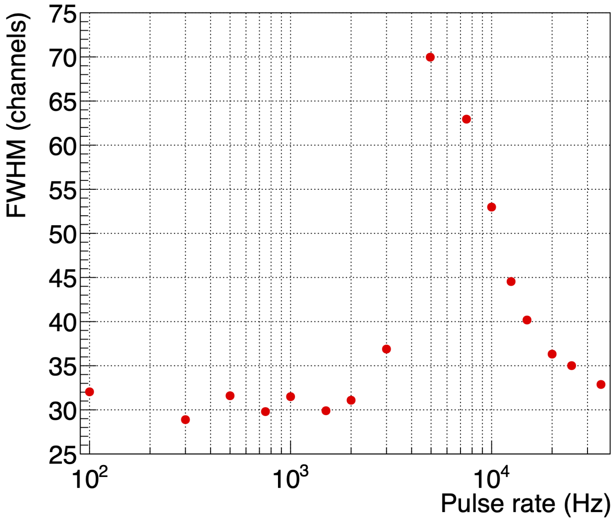

FIGURE 3.8: Energy resolution of the DSSSD at the ^{148}Gd peak located at 3182.7 keV.

section is that the energy resolution of the DSSSD decreased for pulse rates above 5 kHz. In comparison, the energy resolution of the CEPA4 remained between 2% and 3% for rates below 10 kHz, limiting the actual experiment to particle rates below 10 kHz.

3.2.2 Setting of the dynamic ranges of the detectors

Knowing the basic parameters of each detector and controlling the DAQ system were the first steps in preparing the experimental setup. The following steps included mounting the detectors in the experimental chamber and setting their corresponding dynamic ranges. The final goal of this project is to develop a prototype that works in clinical applications. For this reason, this system must be able to work outside vacuum conditions. The use of silicon detectors in air has some downsides, such as their sensitivity to light or their susceptibility to electronic noise. The detectors must be kept in the dark, and they have to be grounded to remove the noise efficiently to overcome these disadvantages.

The theoretical dynamic ranges of the detectors were defined using the simulation toolkit GEANT4 [27]. The simulated dynamic ranges of the detectors were from 0 to 2 MeV, from 0 to 10 MeV, and from 0 to 100 MeV for the front DSSSD, the back DSSSD 2, and the CEPA4 detector, respectively.

Fig. 3.9(a) shows the experimental setup used to set the dynamic range of the detectors, determined by irradiating each of them with the radioactive sources placed in the configuration shown in Fig. 3.9(b). The DSSSD 1 was irradiated with a triple alpha source composed of ^{239}Pu, ^{241}Am, and ^{244}Cm with emission of alpha particles of nominal energies of 5143, 5486, and 5804 keV, respectively; and it was located at $\Delta x_1 = 35$ mm from it. On the other hand, a source of ^{241}Am, with alpha emissions of nominal energy of 5486 keV, irradiated the DSSSD 2 from a distance $\Delta x_2 = 8$ mm. Finally, the CEPA4 was irradiated using $\beta - \gamma$ sources of ^{137}Cs and ^{22}Na.

The final tests of the detectors were performed using the electronic chain shown in Fig. 3.10. The aim was to detect those particles that left energy in each detector at the same time. The electronics were set to acquire information of all events that left energy on at least one detector. A logic signal for each DSSSD was created with an

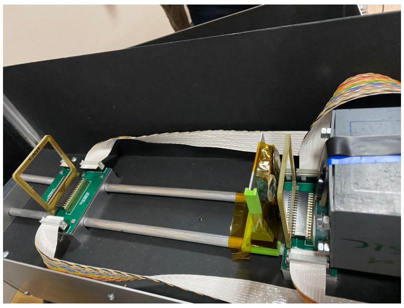

(a) Experimental setup

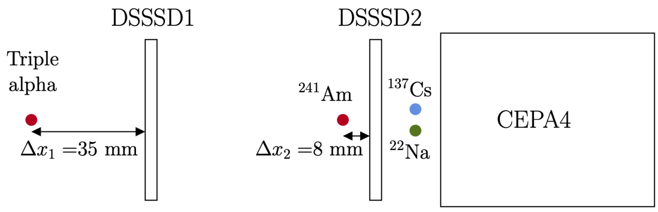

(b) Scheme

FIGURE 3.9: Image and scheme of the experimental setup used for setting the dynamic ranges of the detectors. (a) Image of the setup, (b) Scheme of the setup, red dots represent α sources, blue dot represents β^- source (^{137}Cs) and green dot represents β^+ source (^{22}Na).

OR condition between the time signal of the P and N sides. These signals, alongside the trigger signal of the scintillators, were used to generate a time window of 3μs to acquire the events that arrived within this time, whether or not all of the detectors were hit.

Ideally, one particle hitting the three detectors will generate a coincident signal on each of them, as it is expected to obtain with the proton beam in the experiment at CCB. For this particular case:

1. **Each DSSSD** was connected to a voltage high enough to assure that the detector was fully depleted. The positive and negative charges were collected at the detector's P side (front) and N side (back), respectively. The signal generated was preamplified and then sent to the amplifier. A fast output from the amplifier was processed by a timing filter amplifier (TFA) and a leading-edge discriminator (LED) to produce a logic signal. Both logic signals coming from the P and N sides of the same DSSSD were sent to a three-fold logic unit (TFLU) to generate a logic signal for each DSSSD by means of an *AND* condition between both signals (trigger of the DSSSD). The energy signal of the amplifier was sent to the analog-to-digital converter (ADC).

2. **CEPA4** signals were amplified, filtered, and digitized. The signals were split into three branches for timing, short integration, and long integration. The time signal was processed by a timing filter amplifier (TFA) and a constant fraction discriminator (CFD) to produce an amplitude-independent time trigger (trigger of the CEPA4). The long integration corresponds to the charge-to-digital-converter (QDC) part of the processing software.

The trigger signals of the DSSSDs and of the CEPA4 were sent to the VME controller to generate the gate for the ADCs. This gate had a time window of 3μs that was long enough to acquire the data from all the detectors.

The energies of the alpha particles that reached the first and second DSSSD were determined using the simulation toolkit GEANT4, after passing $\Delta x_1 = 35$ mm and $\Delta x_2 = 8$ mm of air, respectively. The Fig. 3.11(a) shows the spectrum of one strip of the DSSSD 1, where it was possible to distinguish the three peaks of the triple α source at 300, 1237, and 1900 keV, leading to approximately 4200 keV as the full energy range for this detector. It can be seen in Fig. 3.11(b) that the α source of ^{241}Am deposited 4835 keV on the DSSSD 2. The full energy range for this detector in the spectra was determined

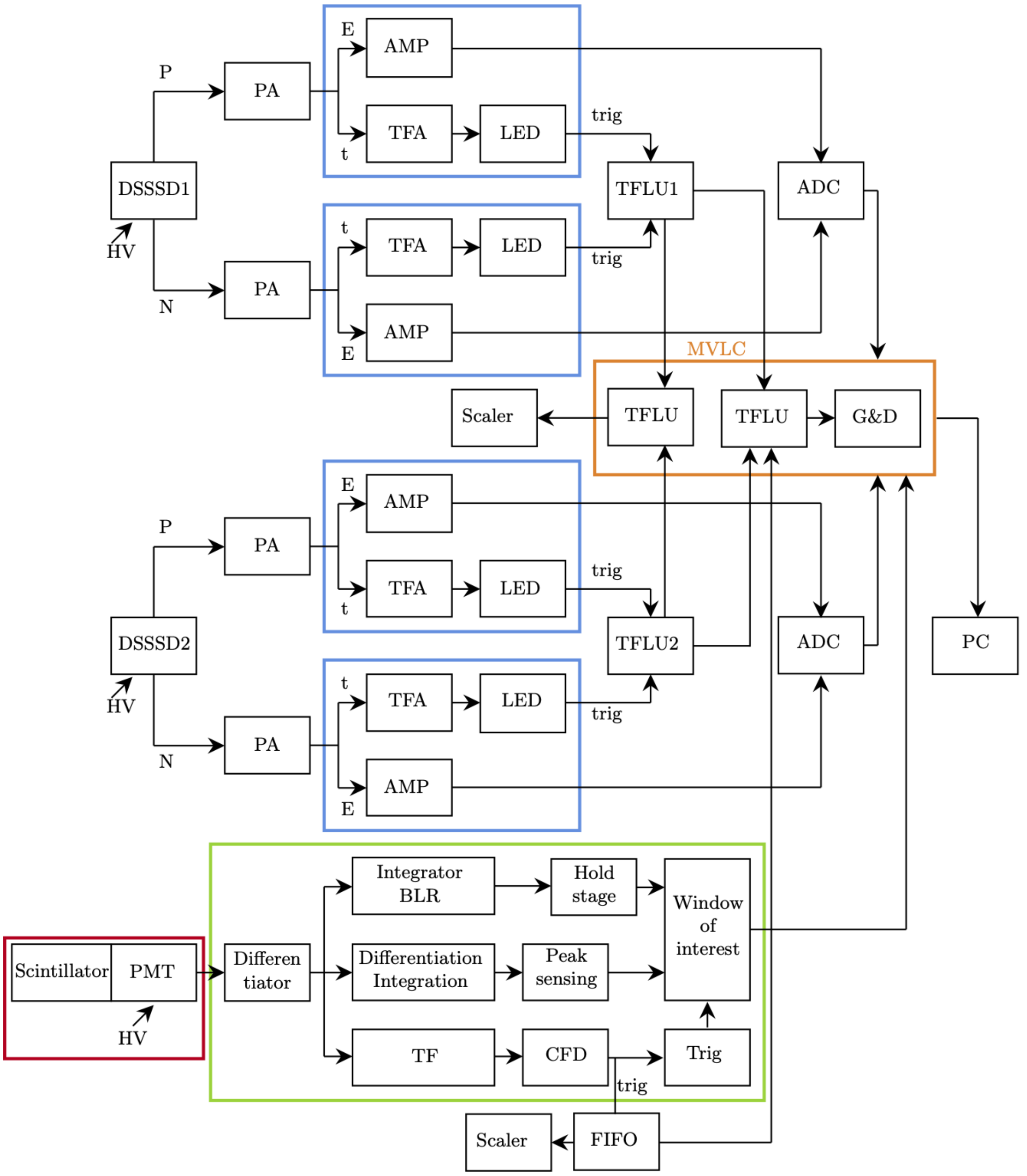

FIGURE 3.10: Electronic chain for the determination of the dynamic ranges of the detectors. The red box represents the CEPA4, the blue boxes represent the shaping/timing filter amplifier modules STM-16+, the green box represents the digital pulse processor module MDPP-16-QDC and the orange box represents the VME controller.

to be approximately 8400 keV. For this part, it was supposed that the dynamic ranges of the detectors tested using α particles were similar to those obtained after the irradiation with protons.

The dynamic range of the CEPA4 was calculated taking the energy deposited by the γ rays emitted in the decay of the ^{22}Na. Fig. 3.12 shows the spectra of two crystal arrays of the CEPA4, where it was possible to distinguish both peaks of the ^{22}Na source. This detector's full energy ranges were approximately 65 MeV for crystals 1 and 2 and 80 MeV for crystals 3 and 4.

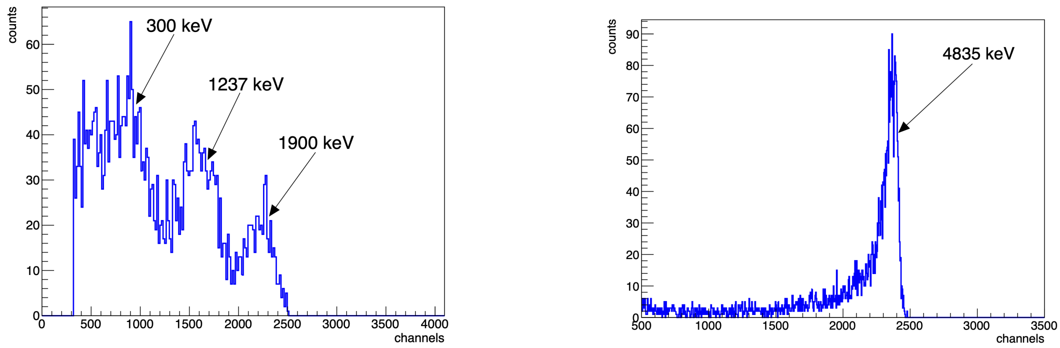

(a) Spectrum of triple alpha source at Δx_1 =35 mm from the DSSSD 1.

(b) Spectrum of ^{241}Am at Δx_1 =8 mm from the DSSSD 2.

FIGURE 3.11: Spectra used to set the dynamic ranges of the DSSSDs. The triple alpha source was located at Δx_1 =35 mm from the first DSSSD, and the ^{241}Am was located at Δx_2 =8 mm from the second DSSSD as shown in Fig. 3.9(b); both sources were in air.

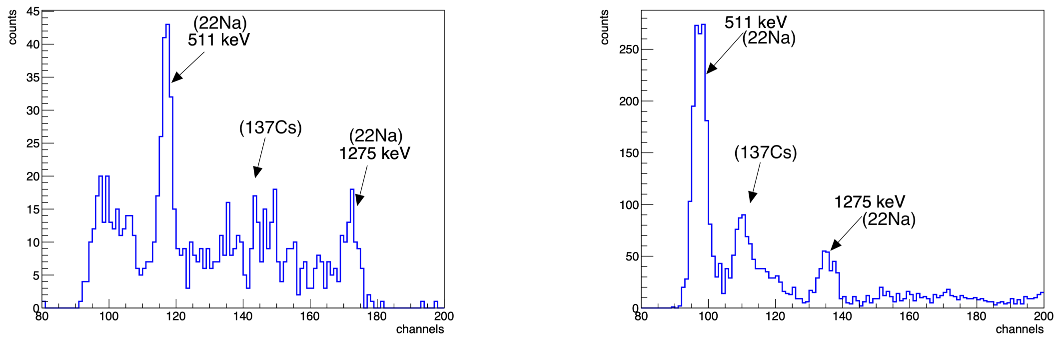

(a) Spectrum of ^{22}Na and ^{137}Cs on the detector 2 of CEPA4.

(b) Spectrum of ^{22}Na and ^{137}Cs on the detector 3 of CEPA4.

FIGURE 3.12: Spectra used to set the dynamic ranges of the CEPA4 detector. The radioactive sources of ^{22}Na and ^{137}Cs were located as shown in Fig. 3.9(b).

To guarantee the coincidence of the signals coming from the three detectors, bringing them all inside the same time window was necessary. As a result, the spectra were measured in coincidence between the detectors. The yellow line corresponding to the trigger indicates that the acquisition system started to collect data in the interval called gate in Fig. 3.13. It was observed that the energy signal of the DSSSD (cyan signal) was always inside the window. The pink signal corresponded to the trigger of the CEPA4 detector, that was observed 300 ns after the energy signal of the CEPA4 detector shown in green. This allowed the determination of the window start and the width of the window as –300 ns and 400 ns, respectively.

With the completion of these tests the initial parameters for the electronic settings of the experiment were obtained. The dynamic ranges of the detectors were set at 4200 keV for DSSSD 1, 8400 keV for DSSSD 2, 65 MeV for detectors 1 and 2 of the CEPA4 and 80 MeV for detectors 3 and 4 of the CEPA4.

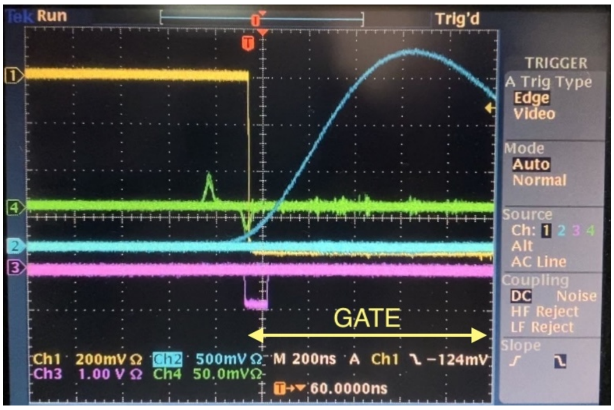

FIGURE 3.13: Logic and analogic signals of the gate, energy signal from DSSSD 2, trigger CEPA4, energy signal CEPA4 (Monitor output MDPP-16).

3.3 Test of the pCT scanner prototype at the Cyclotron Centre Bronowice

The pCT scanner prototype was tested using the Proteus C-235 cyclotron at the Cyclotron Centre Bronowice in Krakow, Poland from June 5 to June 8, 2021. The Cyclotron Centre Bronowice (CCB from its name in Polish, *Centrum Cyklotronowe Bronowice*) is a scientific research center of cyclotrons' applications that is part of the Henryk Niewodniczański Institute of Nuclear Physics Polish Academy of Sciences (IFJ PAN) in Krakow. The Proteus C-235 cyclotron is an isochronous cyclotron installed in its new building at IFJ PAN on May 11, 2012. It can accelerate protons to an energy of 230 MeV, and it was designed and produced for medical applications by IBA (Ion Beam Applications S.A., Belgium) [28, 29].

The prototype was irradiated with proton beams of energies ranging from 90 MeV to 120 MeV. Fig. 3.14(a) shows an image of the placement of the experimental chamber inside the experimental hall at the CCB facility. A scattering target foil of 25 μm of titanium was located at the exit of the beamline. The experimental chamber was located at a distance of $\sim$1066 mm from the scattering target and at an angle of $\sim 12.5°$ with respect to the to the incident proton beam direction to guarantee that the counting rate of the system was below 10 kHz, as shown in Fig. 3.14(c). The beam spot was measured approximately 2 m before the scattering target of titanium, Fig. 3.14(b) shows its dimensions of $\sim 11 \times 11$ mm^2. Table 3.3 shows the calculations of the energy loss in the titanium target and the final energy that reaches the pCT scanner prototype at an angle 12.5° from the beamline. The variations in the energy were considered in the simulations performed by C. Ballesteros [6]

The electronic chain previously described in Fig. 3.10 was used in this experiment. The detection of particles was done in such a way that the system registered all events that left energy at least in one detector. For this reason, the TFLUs of each DSSSD were used as generators of logic gates using the condition *AND* to assure the selection of those events that trigger them simultaneously on the front and back sides. The TFLUs that linked the detectors and generated the acquisition window were set using the condition *OR*.

Fig. 3.15 shows the phantoms of uniform thickness that were imaged using the pCT scanner prototype. To calibrate the detectors, 50 mm of PMMA, resulting from putting together the phantoms shown in Fig. 3.15(a), were irradiated with protons of 95 MeV, 100 MeV, and 120 MeV. Both aluminum phantoms shown in Figs. 3.15(b) and 3.15(c)

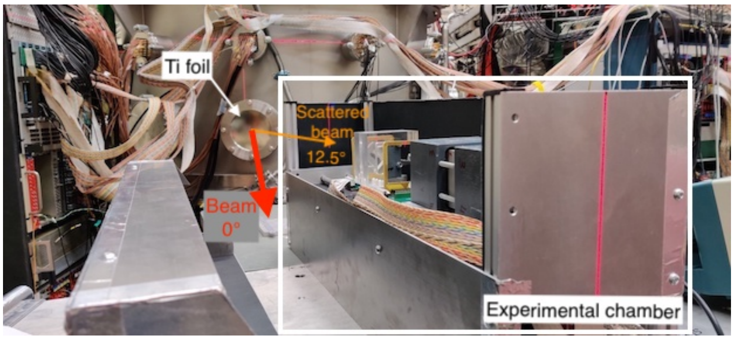

(a) An image of the experimental setup

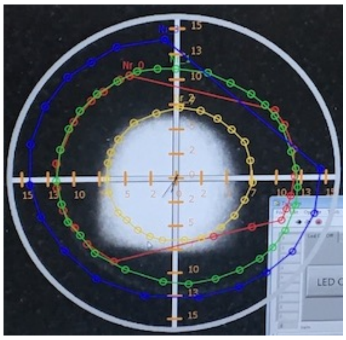

(b) Beam spot

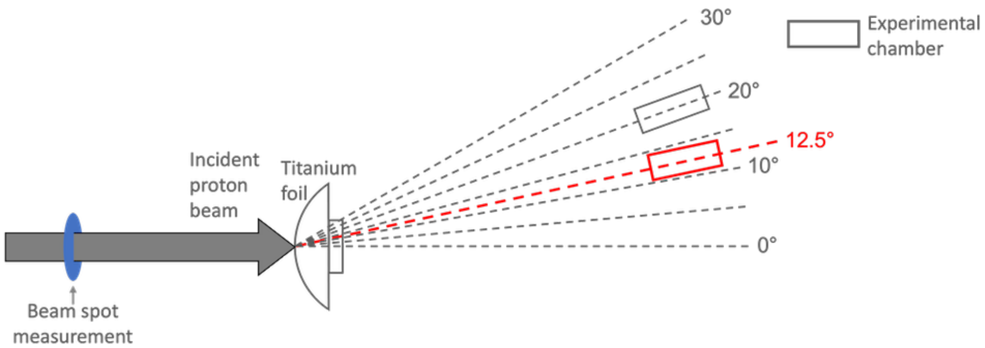

(c) Diagram not scaled of the upper view of the experimental setup

FIGURE 3.14: Experimental setup of the pCT scanner prototype tested at the Cyclotron Centre Bronowice (a) A photo of the placement of the experimental chamber, (b) Beam spot measured at the center of the experimental room, $\approx$ 2m before the titanium foil target, (c) Diagram of the upper view, the red lines represent the location of the experimental chamber with respect to the scattering target and the original beamline (0°).

TABLE 3.3: Proton beam energy that reach the detector after passing through a titanium target of 25 μm thickness and at 12.5° angle form the incident beam direction.

Incident beam energy (MeV)	**Energy loss in 25μm-Ti** (MeV)	**Beam energy at the scattering angle of 12.5°** (MeV))
95	0.060	94.83
100	0.058	99.83
110	0.054	109.83
120	0.050	119.83

have a frame of PMMA, and they were located in a sandwich configuration using the two layers of 20 mm of PMMA, thicker layers shown in Fig. 3.15(a).

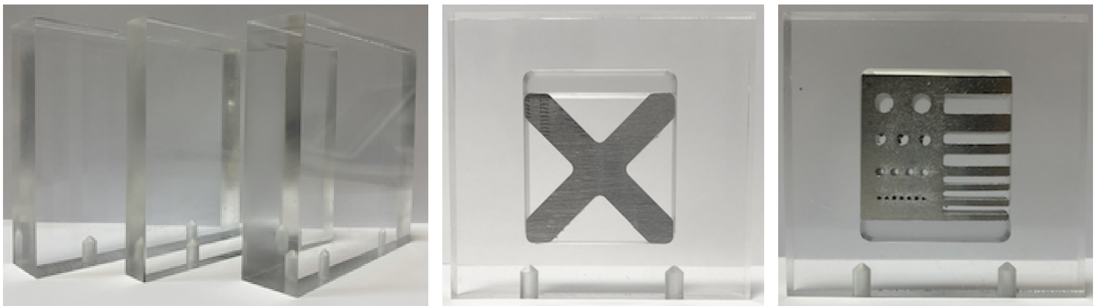

(a) Uniform phantoms of PMMA (b) Cross phantom (c) Derenzo-type phantom

FIGURE 3.15: Uniform thickness phantoms imaged with the pCT scanner prototype at the Cyclotron Centre Bronowice (a) PMMA uniform thickness phantoms of 2×20 mm and 1×10 mm; (b) Uniform thickness aluminum cross phantom with dimensions: 39.80 mm×39.85 mm, 54.30 mm diagonal, 8.95 mm arm width; (c) Uniform thickness aluminum Derenzo-type phantom with dimensions , diameters of the circles from larger to smaller 4.80, 2.95, 2.10 and 1.00 mm and bars of variable width, 2×4.90 mm, 2×2.80 mm and 3×1.95 mm.

Table 3.4 summarizes the irradiation time of the phantoms alongside the beam energies used to image them.

TABLE 3.4: Irradiation time of the phantoms for the different energies used.

Beam energy	**Irradiation time of the phantoms** (min)		
(MeV)	**Uniform**	**Cross**	**Derenzo**
95	6	-	-
100	30, 60	60, 30	60, 30
110	-	-	15
120	6	-	-

Chapter 4

Data analysis algorithms

Spectra for 100-MeV proton beams at the titanium target are shown due to higher the statistics acquired for this dataset. As it was mentioned in chapter 3, the energy that reached the pcT scanner prototype did not correspond to the energy values at the titanium target. When it is said that a measurement was performed at a specific proton energy, it is referred to the energy of the proton beams at the titanium target. The data analysis and all the spectra shown were done using the software ROOT.

4.1 Energy calibration of the detectors

The calibration of the detectors was performed by irradiating them while the uniform phantom was located between the DSSSDs. The proton beam energies used for the calibration were 95 MeV, 100 MeV, and 120 MeV.

Monte Carlo simulations were performed by C. Ballesteros [6] using the simulation toolkit GEANT4. Simulations with the beam energies used in our calibration measurements mentioned above were performed to know the values of energy deposited in each detector. These values were used to calibrate the detectors and they are shown in Table 4.1.

TABLE 4.1: Energy deposited on each detector for the calibration energies, values calculated using the simulation toolkit GEANT4 for initial energies of 95, 100 and 120 MeV.

Beam	**DSSSDs**		**CEPA4**			
energy	**DSSSD1**	**DSSSD2**	**Crystal1**	**Crystal2**	**Crystal3**	**Crystal4**
(MeV)	(keV)	(keV)	(keV)	(keV)	(keV)	(keV)
95	1410.94	3512.27	15682.2	15902.4	15876.7	15618.4
100	1339.84	2746.87	30325.3	30578.3	30532.3	30294.5
120	1143.34	1716.26	67580.8	67661.3	67648.3	67574.5

The structure of the root files was previously described in section 3.1.3. The first step of the analysis involved reading the files to determine the conditions to consider one event a good event. Firstly, all events were analyzed to obtain the energy loss spectra of each detector. As explained in the previous chapter, the electronics were set to acquire data every time at least one of the three detectors was hit. This condition did not guarantee the possibility of tracking the protons, so it became necessary to define a set of steps to define events that were coincident on all the detectors. Consequently, these events were filtered to study only those that simultaneously triggered only one vertical strip and one horizontal strip on each DSSSD, and the CEPA4 detector. The following steps of the analysis are described below for each detector.

4.1.1 DSSDs

The raw spectra show the energy deposited on the detector regardless of the multiplicity of the events on each DSSSD, this is just an unconditioned spectrum of the DSSSDs. Raw experimental spectra of the energy loss on the DSSSDs for different proton energy beams are shown in Figs. 4.1(a) and 4.1(a) fot the first and second DSSSD, respectively. The central strip P7 was selected as a reference. The fact that beams with higher energy passing through thin layers of materials deposit smaller amounts of energy on the layers was observed for both DSSSDs.

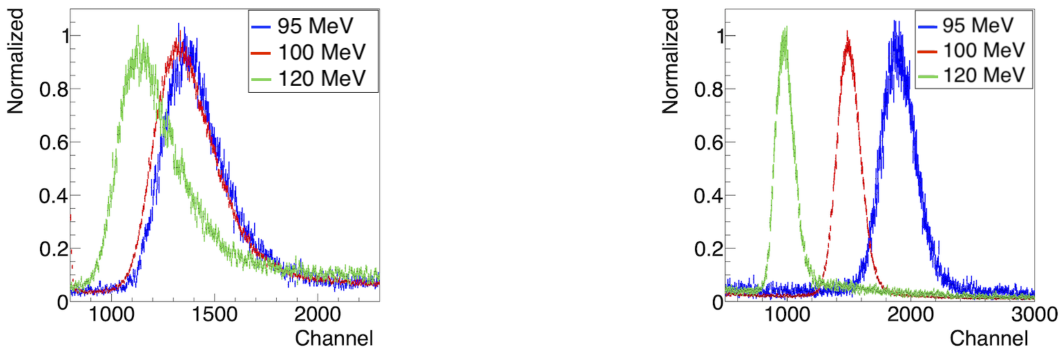

(a) DSSSD 1

(b) DSSSD 2

FIGURE 4.1: Raw energy loss spectra in silicon of the strip P7 of DSSDDs at different energies for the calibration tests, the spectra were normalized to their maximum to be 1 for the measurement of the uniform phantom. The signal produced by the 95-MeV beam is shown in blue, by the 100-MeV beam in red, and by the 120-MeV beam in green.

The energy loss spectra were filtered for those events with multiplicity on each DSSSD equals to two, and that hit only one strip on the P and N sides of the detector. This step reduced the noise signal that appeared outside the peaks of the spectra. Figs.

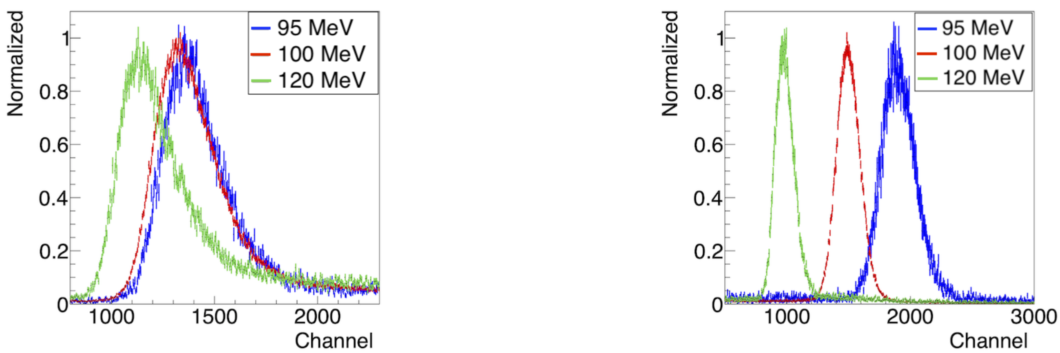

(a) DSSSD 1

(b) DSSSD 2

FIGURE 4.2: Normalized energy loss spectra in silicon of the strip P7 of DSSD2 at different energies for the calibration tests for those events with multiplicity 2 and one hit over any strip of N side and the strip P7, the spectra were normalized to their maximum to be 1 for the measurement of the uniform phantom. The signal produced by the 95-MeV beam is shown in blue, by the 100-MeV beam in red, and by the 120-MeV beam in green.

4.2(a) and 4.2(b) show a lower baseline when compared to the raw spectra shown in Fig. 4.1 for DSSSD 1 and DSSSD 2, respectively.

The energy loss spectra of events hit only one strip on the P and N sides of the detector were analyzed for both tracking detectors with this selection of events. The centroids of the deposited energy peaks were obtained using an automated ROOT program that finds the peaks of the spectra and it fits them to specific functions. The convolution of a Landau and a Gaussian functions properly reproduced the shape of the observed energy loss spectra of the first DSSSD. Fig. 4.3(a) shows an example of the fit performed for all strips of the first DSSSD. The spectra of the second DSSSD were fitted using a Gaussian function, as it can be seen in Fig. 4.3(b). The lines in red are the fits superimposed on the experimental energy loss spectra of the strip P7 of both DSSSDs. The centroids of the peaks are given in Appendix A.

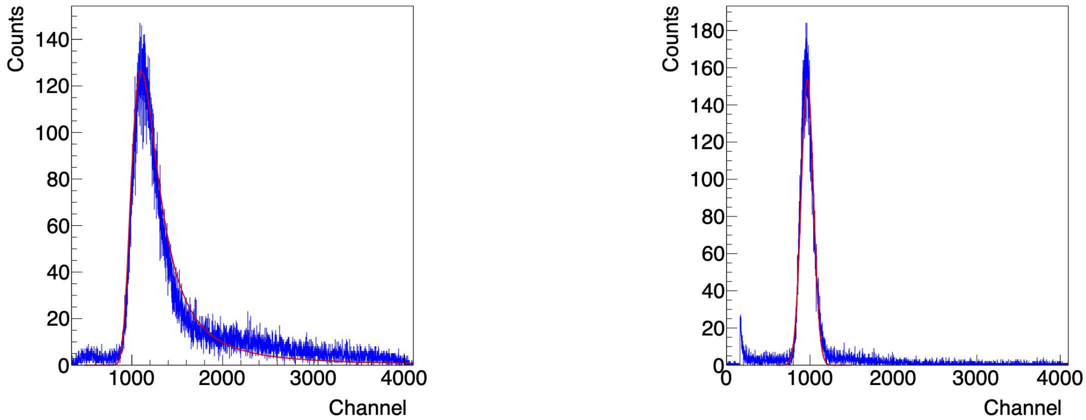

(a) DSSSD 1

(b) DSSSD 2

FIGURE 4.3: Fits of the energy loss spectra of the strip P7 of both tracking detectors for the 120 MeV beam energy (a) DSSSD 1 (b) DSSSD 2.

Each detector was calibrated with a linear fit between the centroids of the peaks displayed in the spectra and the energies of the Table 4.1. The calibration for each detector was performed by following the Eq. 4.1.

$$\text{Energy(keV)} = \text{Slope} \times \text{channel} + \text{Offset} \tag{4.1}$$

Table B.1 shows the calibration parameters of the DSSSDs. The reported energy of an event on each tracking detector corresponded to the energy measured with the P side of the DSSSDs. This selection was justified with the consistently observed better energy resolution of this side for both detectors. The centroids and FWHM of all spectra of the DSSSDs are shown in Appendix C.

No signal was coming from the horizontal strip 1 and the vertical strip 16 of the DSSSD 1 and the horizontal strips 1, 4, and 5, and the vertical strip 15 of the DSSSD 2. From now on, these strips will be called dead strips.

4.1.2 CEPA4

Fig. 4.4 shows the energy deposited in each detector of the CEPA4 normalized to the area of their internal emission. This normalization is equivalent to a normalization per measurement time because the radiation of the $LaBr_3$ and $LaCl_3$ crystals coming from the disintegration of ^{138}La has a constant emission rate [22]. The anodes of crystals 1, 2, and 3 were calibrated using only two energy peaks, as the corresponding to 120 MeV was not observed since it was out of range as it can be seen in the spectra. The anode of crystal 4, and all the dynodes were calibrated with three points.

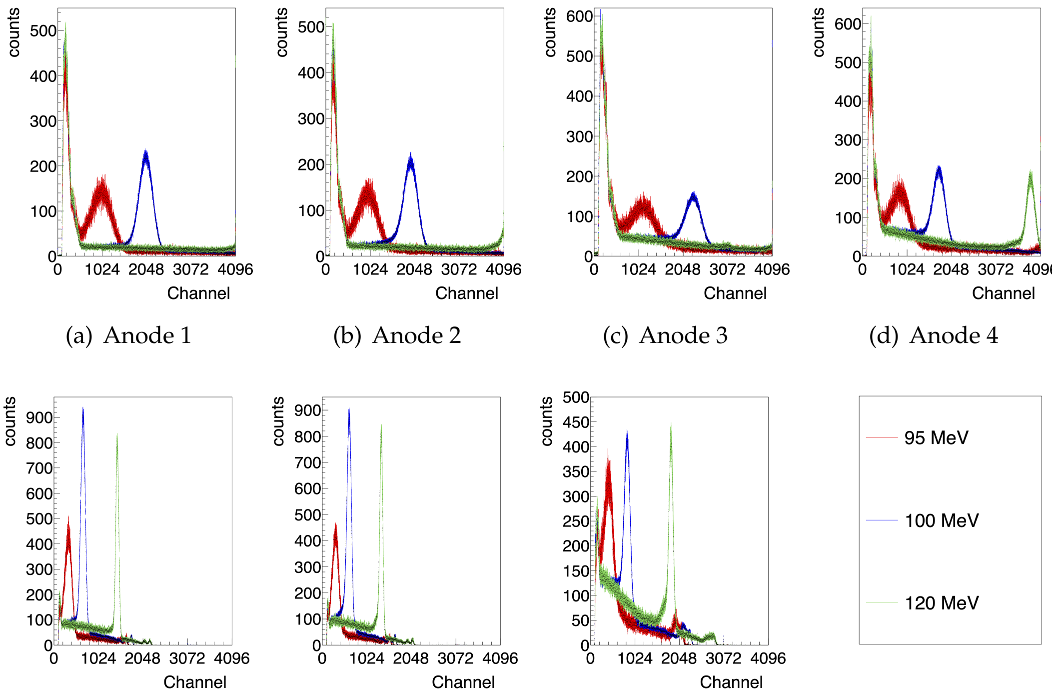

(a) Anode 1 (b) Anode 2 (c) Anode 3 (d) Anode 4

(e) Dynode 1 (f) Dynode 2 (g) Dynode 3

FIGURE 4.4: Spectra of the calibration tests for the CEPA4 normalized to the area of the internal emission of the crystals for the measurement of the uniform phantom with 95-MeV, 100-MeV, and 120-MeV proton beams. The signal produced by the 95-MeV beam is shown in red, by the 100-MeV beam in blue, and by the 120-MeV beam in green.

The peaks in the spectra were fitted using a Gaussian function. Table A.3 shows all the centroids of the anodes and dynodes. Each crystal was calibrated with a linear fit following the Eq. 4.1. The calibration parameters of the CEPA4 are presented in Table B.2.

4.2 Selection of events

The events were selected according to the criteria described in this section. Each DSSSD collected information of the energy deposited on it with the front side (P side) and the rear side (N side) per event. Fig. 4.5 shows the 2D plots of the energy distribution of all the events on each DSSSD for the measurement at 100 MeV with the uniform phantom. The color scale was set in a logarithmic scale observe the different regions in which the events were distributed.

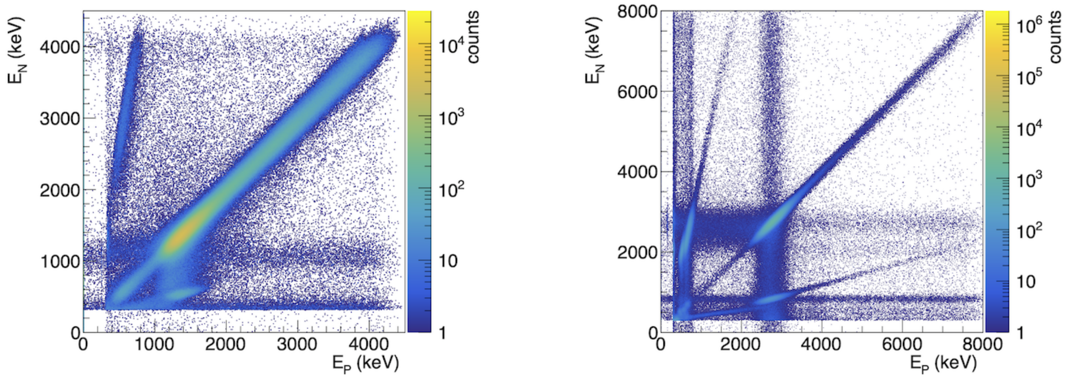

(a) DSSSD 1 (b) DSSSD 2

FIGURE 4.5: Two-dimensional plots of the energy distribution of events in an energy on side P versus energy on side N representation for each DSSSD for the measurement at 100 MeV with the uniform phantom. (a) DSSSD 1, (b) DSSSD 2

4.2.1 Energy difference between the P side and N side of the DSSSDs

The energy difference between the P side and N side was calculated for all events. Fig. 4.6 shows the distribution of this energy difference for both DSSSDs for the measurement at 100 MeV with the uniform phantom. The energy difference distributions were fitted to Gaussian distributions. The accepted events were those having an absolute value of the energy difference lower than 3σ. The standard deviations σ of the energy difference of DSSSD 1 and DSSSD 2 were 78.48 and 67.25 keV, respectively.

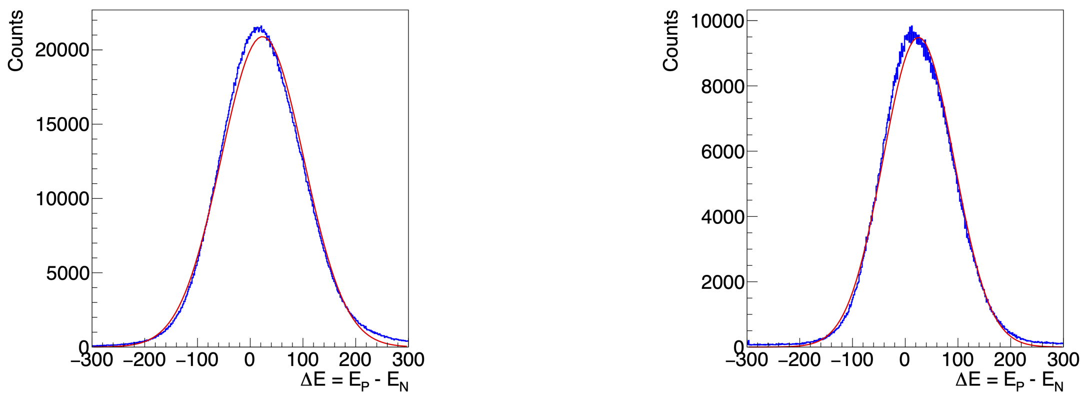

(a) DSSSD 1 (b) DSSSD 2

FIGURE 4.6: Difference between the energy measured at the P side and N side for the same event. (a) DSSSD 1 (b) DSSSD 2.

Fig. 4.7 shows two-dimensional plots of the energy distribution of events (energy deposited on the N-side vs. energy deposited on the P-side) on each DSSSD that have an absolute value of the energy difference lower than 3σ, which were considered accepted events.

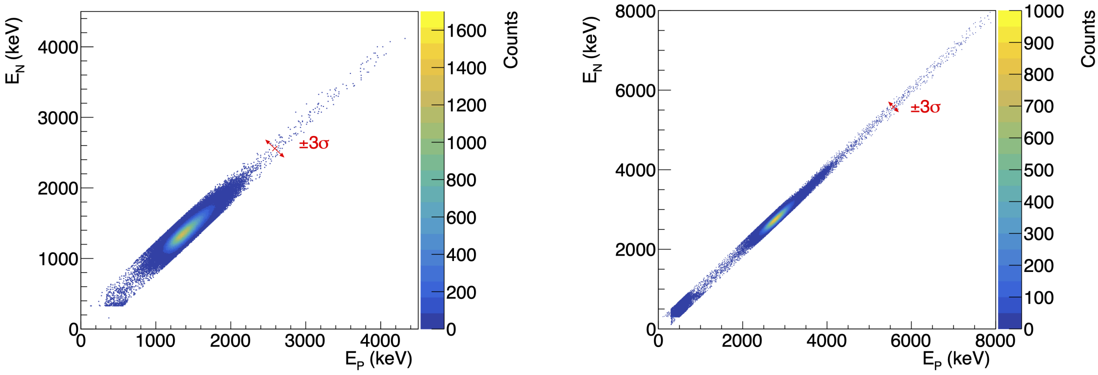

(a) DSSSD 1

(b) DSSSD 2

FIGURE 4.7: Two-dimensional plots of the energy distribution of events (energy deposited on the N-side vs. energy deposited on the P-side) that have an absolute value of the energy difference lower than 3σ on each detector for the measurement at 100 MeV with the uniform phantom. (a) DSSSD 1, (b) DSSSD 2.

4.2.2 Deposited energy on the DSSSDs

Fig. 4.8 shows the energy spectra of all the events that hit each DSSSD on any of the strips. The particles deposited different amounts of energy on both detectors; on the first DSSSD the spectra showed an energy distribution centered around 1350 keV, meanwhile on he second DSSSD the distribution was centered around 2700 keV. The events that deposited energy between 1000 and 2000 keV on this detector and more than 1200 keV on DSSSD 2 were selected as accepted events.

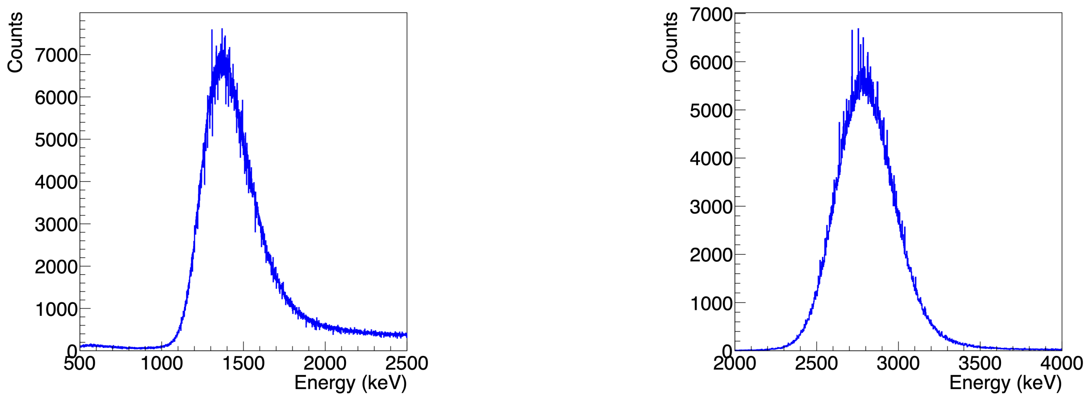

(a) DSSSD 1

(b) DSSSD 2

FIGURE 4.8: Total energy spectra of the DSSSDs for the determination of the energy limits of the events (a) DSSSD 1 (b) DSSSD 2.

Two-dimensional plots of the energy distribution of events on each DSSSD that have an absolute value of the energy difference lower than 3σ and now, with the added condition that the energy deposited on the first detector was between 1000 keV and 2000 keV and more than 1200 keV on the second detector are shown in Fig. 4.9.

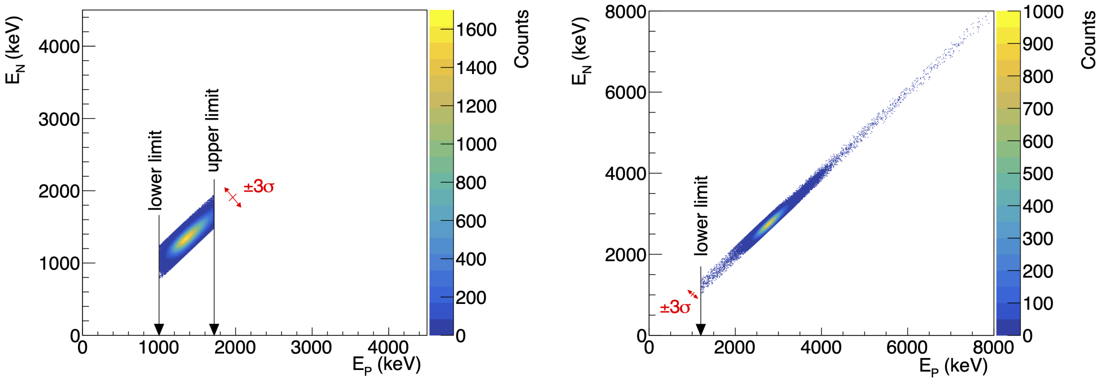

(a) Selected events for DSSSD 1 (b) Selected events for DSSSD 2

FIGURE 4.9: Energy distribution of events (energy deposited on the N-side vs. energy deposited on the P-side) of each detector for the measurement at 100 MeV with the uniform phantom. (a) Selected events for DSSSD 1 (b) Selected events for DSSSD 2.

4.2.3 Deposited energy on the CEPA4

The last selection criterion of good events was that the proton deposited energy on the CEPA4. This final condition guaranteed the coincidence on all three detectors, which made possible to identify a proton traversing the phantom whose energy loss can be determined using this setup. Fig. 4.10 shows the energy spectra of all the events that correspond to protons that hit each DSSSD and met the following criteria:

- The absolute value of the energy difference measured between the front side and the back side of each detector was lower than 3σ.
- The deposited energy on the first detector was between 1000 keV and 2000 keV and on the second detector was more than 1200 keV.
- The particle deposited energy on the CEPA4.

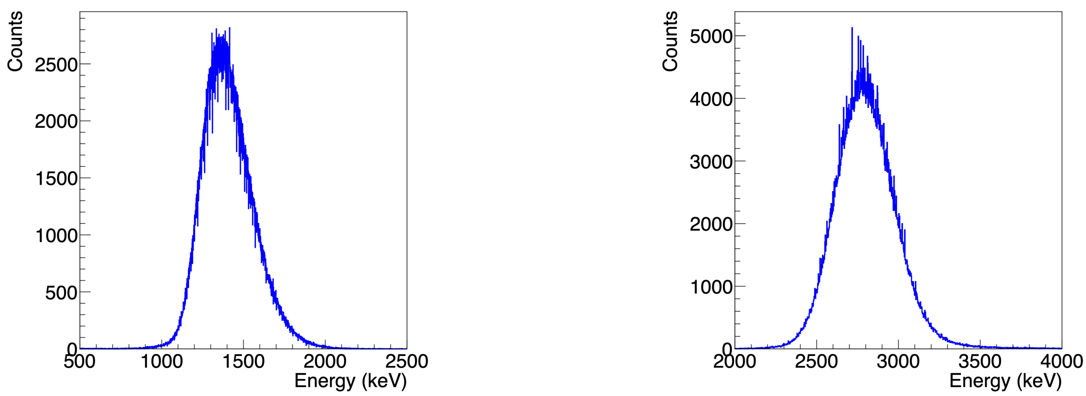

(a) DSSSD 1 (b) DSSSD 2

FIGURE 4.10: Filtered total energy spectra of the DSSSDs (a) On DSSSD 1 (b) On DSSSD 2.

With the conditions described to select a good event, in a central strip of DSSSD 1 approximately 60% of the initial events were lost, as it can be seen in Fig. 4.11(a). Fig.

4.11(b) shows a lower loss of events on the number of events ($\sim$ 40%). This occurs because the effective area of this detector is higher than the effective area of the first DSSSD. A visual difference is perceived on the integral of the good events (in pink), this is due to the different energy resolution that detectors have. However, the integral of the good events correspond to $\sim$ 90000 counts for both strips of the DSSSDs.

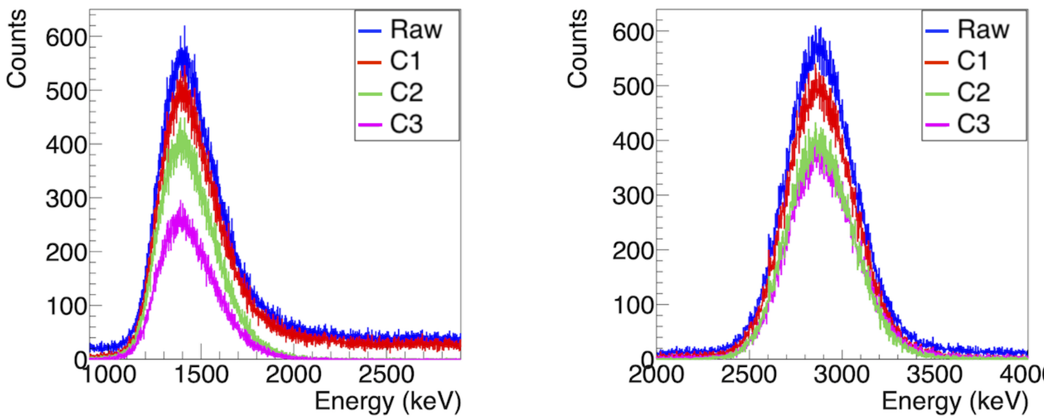

(a) DSSSD 1

(b) DSSSD 2

FIGURE 4.11: Energy loss spectra of the strip P7 of both DSSSDs, showing the raw spectra in blue, the spectra of those events that hit one vertical strip and one horizontal strip on each DSSSD in red, in green the spectra of the events in coincidence between DSSSDs, and the spectra events in coincidence between the three detectors (good events) in pink for the measurement at 100 MeV with the uniform phantom.

4.3 Proton track reconstruction

The criteria described in the previous section were used to create the plots of the number of hits and the energy deposited on the detectors. Event by event, all the criteria to select the events were checked. The reconstruction of two-dimensional images was performed in two phases. The general procedure consisted of the analysis of the events that fulfilled the criteria. The additional procedure comprised the recovery of the events that hit dead strips.

4.3.1 General procedure

Each time a proton hit one vertical strip and one horizontal strip, the Cartesian combination of both strips gives the position of the hit on the detector. From now on, the intersection between a vertical and a horizontal strip will be called a pixel. The position and energy of all events were registered into two-dimensional plots of hits and energy deposited. Fig. 4.12 shows the two-dimensional plots of the hits on both DSSSDs for the measurement with the uniform phantom at 100 MeV. These plots represent the number of protons on each pixel that deposit energy on each detector. Several white strips were observed. The white strips corresponded to strips that did not get any signal because they were damaged, constituting what is defined here as dead strips. The front tracking detector had one vertical and one horizontal dead strips both located at the border. On the other hand, the rear tracking detector had three vertical and one horizontal dead strips.

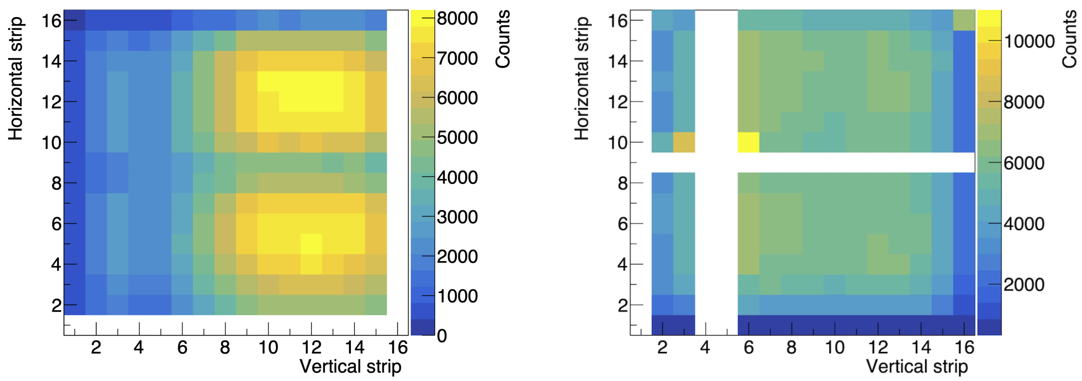

(a) DSSSD 1 (b) DSSSD 2

FIGURE 4.12: Two-dimensional plots of the number of hits on the DSSSDs for the measurement at 100 MeV with the uniform phantom. (a) DSSSD 1, the strips horizontal 1 and vertical 16 were damaged, (b) DSSSD 2, the strips horizontal 9 and vertical 1, 4 and 5 were damaged.

Fig. 4.13(a) shows possible proton trajectories through the detection system from a simplified top view of the detectors. Orange and purple lines show two possible trajectories of undetected protons as no energy was deposited at DSSSD 2 or the CEPA4 detectors. Blue line displays a trajectory of protons detected with the same strip on both DSSSDs. The green line displays the last possibility: a proton hit a detector on different strips on the front and rear detectors.

The hit's position on the phantom was determined using the coordinates of the hits on the front and rear detectors. It is possible to divide the phantom into segments similar to the DSSSDs. With the segmentation of the phantom, it was possible to locate the position of the proton hits. The position of the proton hit on the phantom was determined using the Eq. 4.2.

$$(x,y)_P = \left(\frac{x_1+x_2}{2}, \frac{y_1+y_2}{2}\right) \tag{4.2}$$

where $(x,y)_P$ represents the Cartesian coordinates of the proton hit on the phantom, and (x_1,y_1) and (x_2,y_2) are the coordinates of the proton hit on the front and rear DSSSD, respectively.

Fig. 4.13(b) shows possible proton trajectories through one single pixel of each DSSSD. In the figure, it can be seen that the hit positions are distributed within each pixel area.

The distribution of events on each pixel was modeled using a random generator between 0 and 1 for each DSSSD. This made possible to uniformly distribute the events of one pixel over its full area, using Eq. 4.3.

$$(x,y)_P = \left(\frac{(x_1+R(0,1))+(x_2+R(0,1))}{2}, \frac{(y_1+R(0,1))+(y_2+R(0,1))}{2}\right) \tag{4.3}$$

where $(x,y)_P$ represents the Cartesian coordinates of the proton hit on the phantom, (x_1,y_1) and (x_2,y_2) are the coordinates of the proton hit on the front and rear DSSSD, respectively, and $R(0,1)$ are uniform random values between 0 and 1 that were included to guarantee a uniform distribution of events on each pixel.

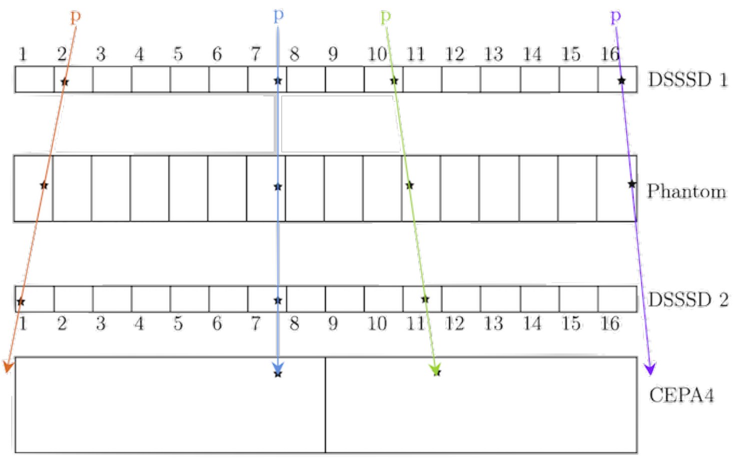

(a) Top view

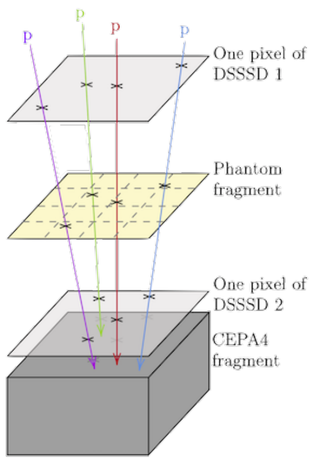

(b) One pixel view

FIGURE 4.13: Possible proton trajectories through the detection system.

The increment on the images' granularity on the phantom plane was possible due to the random distribution of events on each pixel that were previously described. The drawback of having dead strips on the DSSSDs did not allow a total reconstruction of the images on the phantom plane, as it can be seen in plots of the hits on the uniform phantom of Fig. 4.14. Two areas with lower number of counts are mainly observed, a horizontal area between strips 8 and 9 and a vertical area between strips 4 and 6. The low count areas correspond to the dead strips of the second tracking detector. Meanwhile the dead strips of DSSSD1 cause the empty borders at the bottom and right side. The empty border on the left side corresponds to the dead strip in the DSSSD2. Note that if a particle hits a dead strip on any detector, it is not fulfilling the coincidence conditions that we apply, therefore, it does not contribute to the image obtained. These preliminary results showed that the recovery of dead strips was necessary to reconstruct the two-dimensional images of the phantoms.

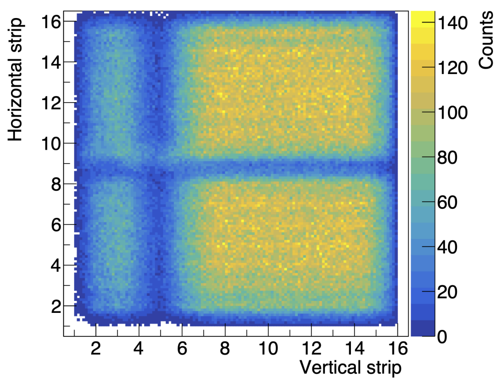

FIGURE 4.14: Two-dimensional plot of the number of hits on the uniform phantom for the measurement at 100 MeV.

4.3.2 Additional procedure: Recovery of the dead strips

Fig. 4.15 shows the energy loss spectra of the strips P7 and P6 of the DSSSD 2. Both spectra show a peak around channel number 2800 which corresponds to protons hitting such strips. The strip P6 was next to a dead dead strip and it displayed an additional peak placed at channel number 522 as shown in Fig. 4.15(b). The peak centered at channel 522 (~522.6 keV) corresponded to events coming from the dead strip P5. It was observed that the charge collected on any of the dead strips was transmitted to their neighboring strips. Two different recovery methods were used.

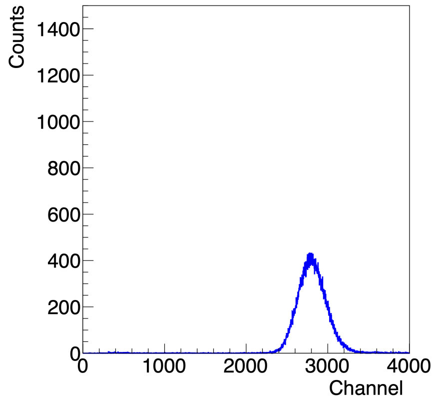

(a) Strip P7 (b) Strip P6

FIGURE 4.15: Spectra of (a) Strip P7, and (b) Strip P6 of DSSSD2.

First recovery algorithm

The first approach to recover these events was to pair the dead strips with one contiguous strip. Strips P16 and N1 of the first DSSSD were paired to strips P15 and N2, respectively. On the other hand, strips P1, P4, P5, and N9 of the second DSSSD were paired to strips P2, P3, P6, and N8, respectively. Each time an event deposited less than 1000 keV on the contiguous strips, a count on the dead strip was added. The energy lost by the proton was taken from the energy measured with the coincident strip from the other side (front or rear) depending on the case where the full charge generated by the traversing particle was collected.

The results of the first recovery algorithm on the DSSSDs are shown in Fig. 4.16.

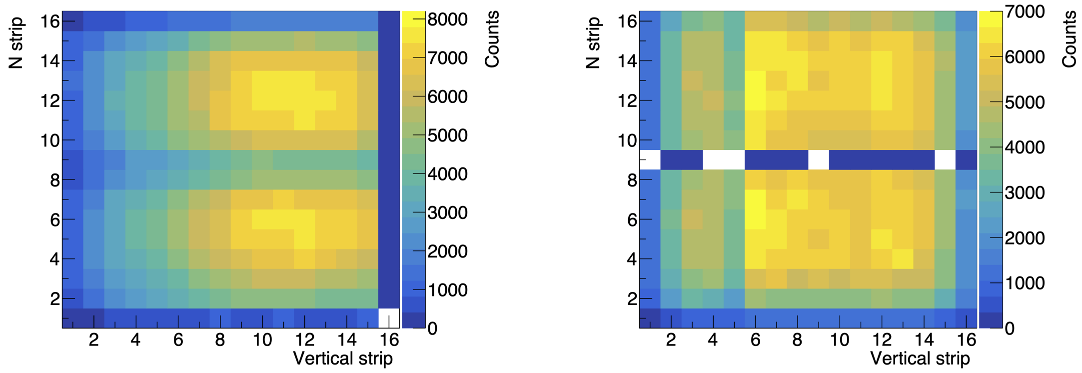

(a) DSSSD 1 (b) DSSSD 2

FIGURE 4.16: Two-dimensional plots of the number of hits on DSSSDs for the measurement at 100 MeV with the uniform phantom after the first recovery algorithm. (a) DSSSD1, (b) DSSSD2.

Fig. 4.17 shows that this step improved the reconstruction of the vertical strips on the phantom plane. Nevertheless, it yielded similar results for the horizontal area between strips 8 and 9.

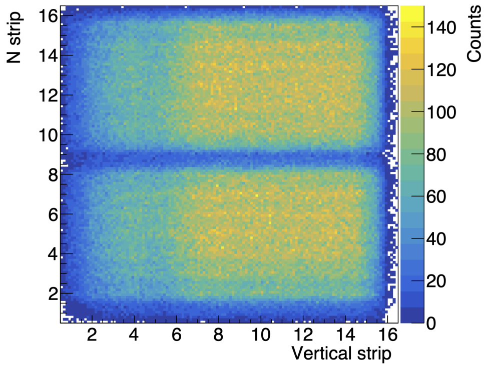

FIGURE 4.17: Two-dimensional plot of the number of hits on the uniform phantom for the measurement at 100 MeV after the first recovery algorithm.

Second recovery algorithm

The subsequent approach included the study of two types of events with multiplicity equals to three on DSSSD 2. The first type were those events that hit any of the vertical strips (P side) and strip N9, where the charge of strip N9 was simultaneously distributed between strips N8 and N10. When an event fell into this category, one count was assigned to the pixel $(x, 8)$, where x is the number of the vertical strip triggered. The energy loss of these events was the energy measured on the P side. The second type of events hit strip P4 or P5, and the charge was partially collected by strips P3 and P6 and any of the horizontal strips (N side). Similarly, if an event came under this type, one count was assigned to the pixel (x, y), where x is the strip P4 or P5, according to the contiguous strip (P3 or P6) that had collected more charge, and y is the number of the horizontal strip triggered. The energy loss of these events was the energy measured on the N side. Both types of events were selected if the reported energy was within the

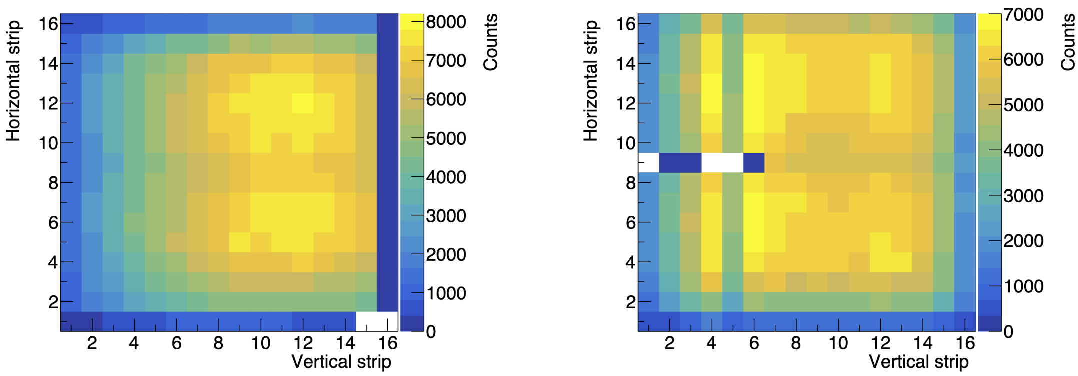

(a) DSSSD 1

(b) DSSSD 2

FIGURE 4.18: Two-dimensional plot of the number of hits on the DSSSDs for the measurement at 100 MeV with the uniform phantom after the second recovery algorithm.

energy ranges for each detector, between 1000 and 2000 keV, and higher than 1200 keV for the first and second DSSSD, respectively. Fig. 4.18 shows the results of the second recovery algorithm on the DSSSDs.

The main clear difference between Figs. 4.16 and 4.18 is the increase in the central horizontal strips of both DSSSDs. The counts on the strip N9 of the second DSSSD approximately increased in 50000 counts. This increment corresponded to the increment on counts of the strips N8, N9, and N10 of the first DSSSD which were triggered in coincidence with the strip N9 of the second DSSSD. Fig. 4.19 shows that this last step improved the reconstruction of the horizontal strips on the phantom plane, giving a notorious difference between images performed without and with the recovery of the dead strips. Nevertheless, the recovery algorithms applied were not enough to improve the two-dimensional plot of the hits on the uniform phantoms in the region where the dead strips intersect.

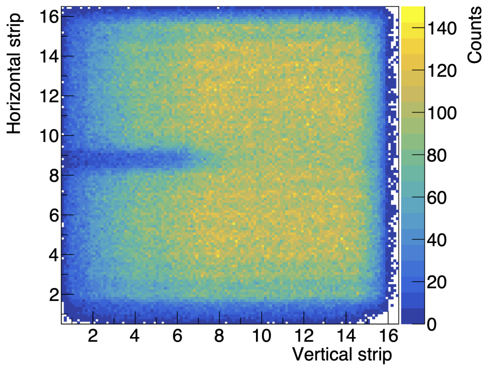

FIGURE 4.19: Two-dimensional plot of the number of hits on the uniform phantom for the measurement at 100 MeV after the second recovery algorithm.

The plots of the number of hits shown in Figs. 4.18 and 4.19 display non-uniform particle counts due to the Rutherford scattering that occurs on the scattering target of titanium located at the exit of the beam. Regions on the right get higher particle counts because they are located closer to the incident beam direction (0° of scattering angle). Lower counts on the borders were observed for both DSSSDs. The darkening on the borders can be explained by the reduction of the effective area of both detectors. To achieve higher effective areas, the use of a collimated or pencil beam, perpendicular to the DSSSD detectors instead of the scattered beam we are using in this experiment is necessary. For this reason, the experimental chamber was located far from the beam exit.

Fig. 4.20 shows a scheme of the positioning of the detectors at CBB facility. The total active areas of both DSSSDs are 50×50 mm^2 and the total active area of the CEPA4 detector is 54×54 mm^2. The experimental chamber was located 1066 mm away from the beam exit, the DSSSDs were separated 152 mm from each other, and the CEPA4 was located at 108 mm from the DSSSD 2. In this configuration, the effective areas of the front and rear DSSSD are 75.4% and 98.4%, respectively.

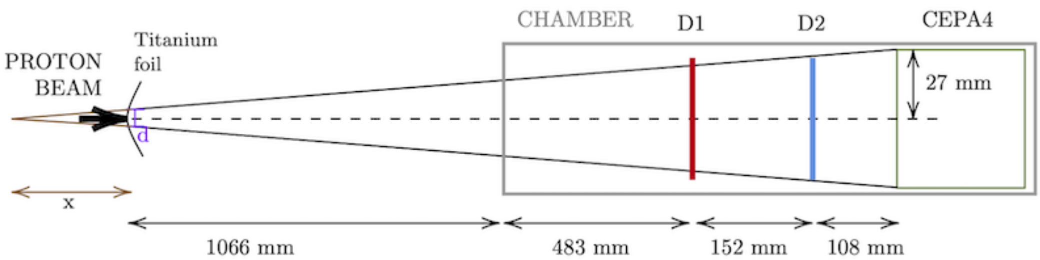

FIGURE 4.20: Scheme to determine the effective area of the detectors. Figure not scaled.

4.4 Reconstruction of the image in the phantom plane

Two-dimensional plots of the energy loss were generated alongside the plots of the hits on each detector to study the energy deposited per proton. Fig. 4.21 shows the plots of the energy loss on the tracking detectors. The distribution of energy on the pixels due to the particle distribution on the detectors made the Rutherford scattering effects observed on the energy loss plots.

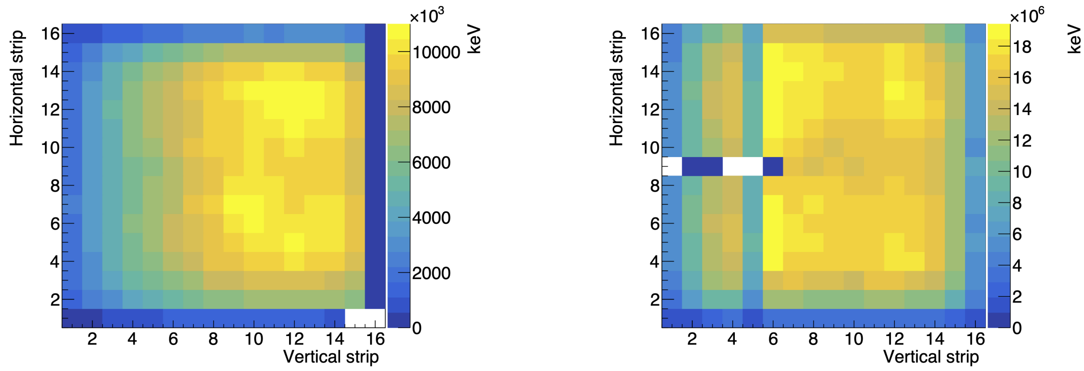

(a) DSSSD 1

(b) DSSSD 2

FIGURE 4.21: Two-dimensional plots of the energy losses on the DSSSDs for the measurement at 100 MeV with the uniform phantom.

The two-dimensional plots of the energy loss were divided by the plots of the number of hits for both detectors to correct the apparent effect of non-uniform energy loss caused by the Rutherford scattering. Two-dimensional plots of the energy lost per hit on the DSSSDs for the calibration test at 100 MeV are shown in Fig. 4.22. On average, protons of 100 MeV deposited approximately 1400 keV on the first DSSSD and 2700 keV on the second DSSSD.

To obtain the two-dimensional plots of the energy deposited per hit, the process included three main steps:

1. Obtain the two-dimensional plot of the number of hits.
2. Obtain the two-dimensional plot of the energy deposited on the scanner detectors.
3. Divide the two-dimensional plot of the energy deposited by the two-dimensional plot of the number of hits.

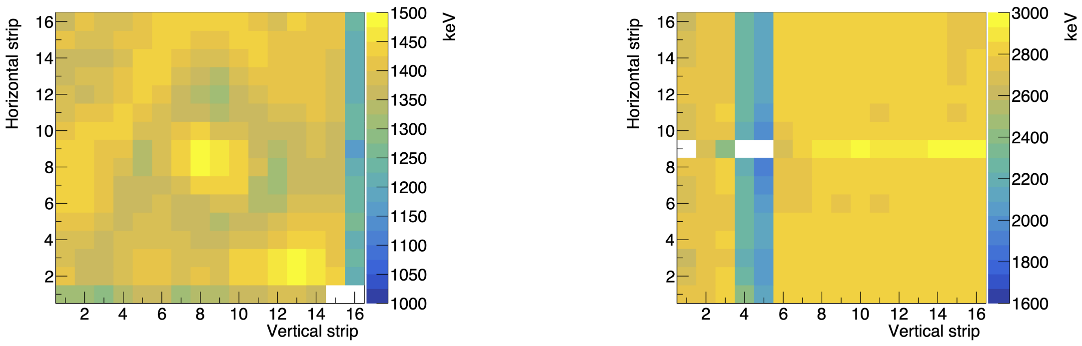

(a) DSSSD 1 (b) DSSSD 2

FIGURE 4.22: Two-dimensional plots of the energy lost per hit on the DSSSDs for the measurement at 100 MeV with the uniform phantom.

The images at the the phantom plane were obtained by adding the energy deposited on all three detectors on each pixel. Fig. 4.23 shows the two-dimensional plots of the energy lost per particle on the detectors for the three different phantoms tested at 100 MeV. The color palette was changed in order to compare with the simulated results presented in the following chapter.

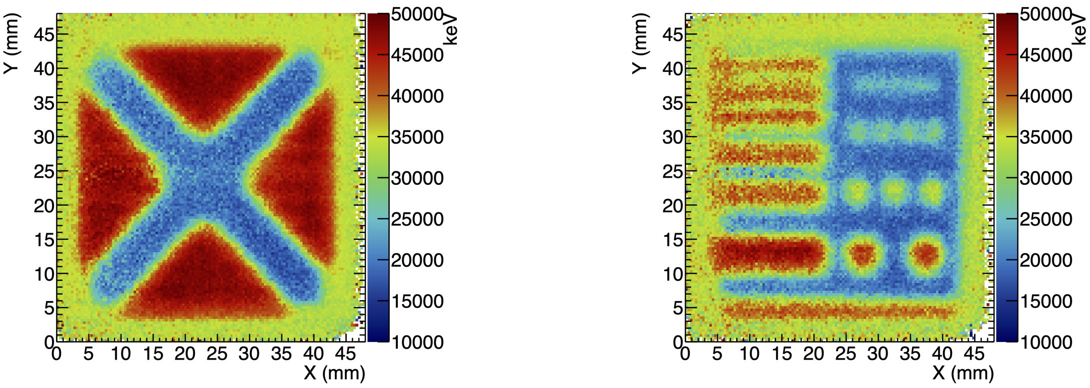

(a) Cross phantom (b) Derenzo-type phantom

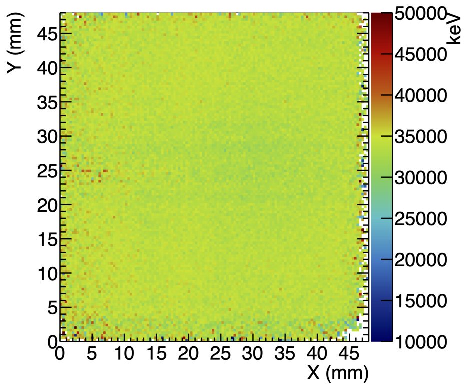

(c) Uniform phantom

FIGURE 4.23: Two-dimensional plots at the phantom plane of the energy lost per proton on the detectors for the measurement at 100 MeV beam.

Chapter 5

Discussion

In this chapter, the final reconstructed images are presented and studied. It is also presented a comparison with simulated results as part of the work done by C. Ballesteros in his Master thesis [6].

As mentioned in Chapter 3, the phantoms were located in the sandwich configuration shown in Fig. 5.1. When referring to specific material, it is implied that protons traversed 20 mm of PMMA before and after this material.

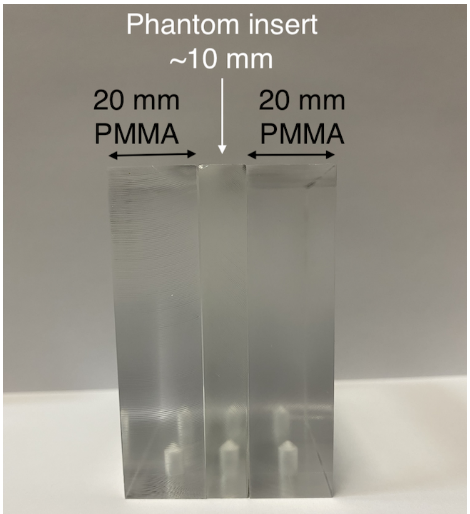

FIGURE 5.1: Sandwich configuration used for the irradiation of the phantoms. For all the radiographs, two 20-mm-thick PMMA layers were placed before and after the 10 mm layer containing the aluminum patterns.

5.1 Imaging the aluminum cross phantom

The aluminum cross phantom shown in Fig. 5.2(a) was inserted between two PMMA pieces of 20-mm thickness as shown in Fig. 5.1 and it was irradiated with proton beams of 100 MeV. Two data sets were acquired, the first one during a 1-hour run and the second during a run that lasted 30 minutes. The reconstructed images are shown in Fig. 5.2(c) and 5.2(e), respectively. Images were built and exported as PNG files in greyscale to perform their post-analysis using the ImageJ software [30]. Eighteen measurements described in Fig. 5.2(b) were performed in the image to determine differences between the actual dimensions of the phantom and the ones estimated from the image (radiograph). The study of this phantom may be methodologically simple, but precise results confirm the reconstruction algorithm for a simple geometry.

(a) Phantom insert

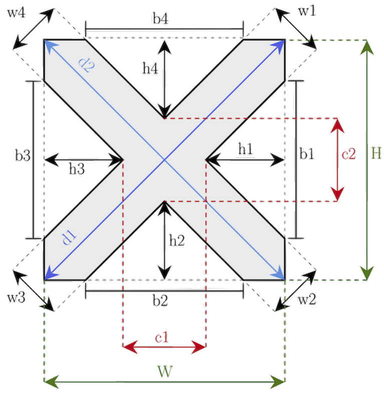

(b) Lengths of the phantom defined for the comparison between results

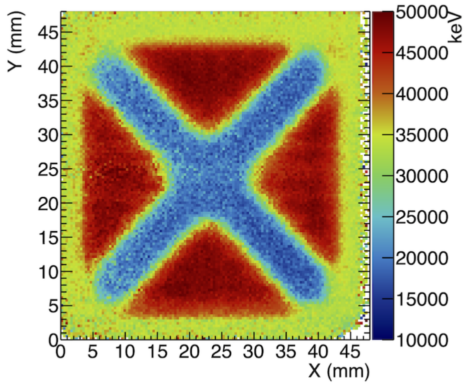

(c) Experimental image from 1-hour measurement corresponding to 1.6×10^6 counts

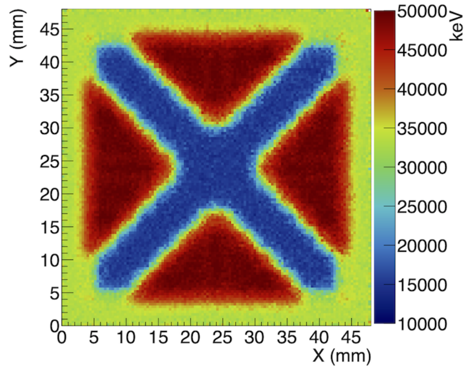

(d) Simulation with $\approx 1.6 \times 10^6$ counts

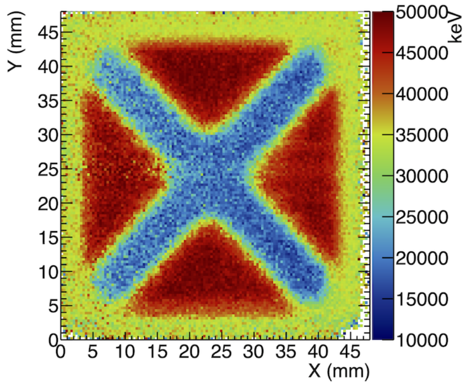

(e) Experimental image from 1-hour measurement corresponding to 8×10^5 counts (proton hits)

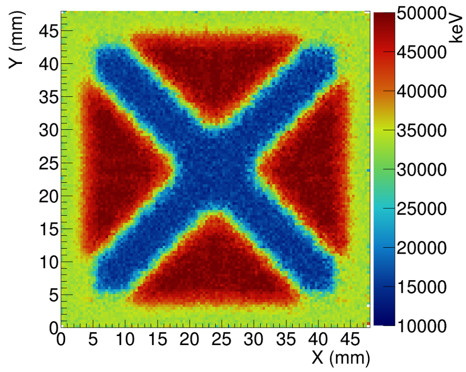

(f) Simulation with $\approx 8 \times 10^5$ counts

FIGURE 5.2: (a) Aluminum cross phantom, (b) Lengths of the phantom defined for the comparison between experimental and simulated results. Two-dimensional plots of the energy lost per hit on the scanner at the phantom plane (c) Experimental for 1-hour measurement (1.6×10^6 counts), (d) Simulation with $\approx 1.6 \times 10^6$ counts, (e) Experimental for 30-minutes measurement (8×10^5 counts), (f) Simulation with $\approx 8 \times 10^5$ counts. Images (d) and (f) taken from [6].

Fig. 5.2(c) and 5.2(e) display three well-differentiated zones that correspond to the different materials present in the phantom insert that we can see in Fig. 5.2(a): PMMA, air, and aluminum.

The green frame that is observed corresponds to the zone where protons pass through the PMMA region. Each proton that traversed the PMMA deposited, in average, 33 MeV on the scanner detectors. This average energy deposited per hit corresponded to the energy deposited per proton on the scanner detectors after passing through 50 mm of PMMA (Fig. 4.23(c)). The zones where protons pass through air are four triangular red sectors that appear in red in the image. Each proton that went through this region deposited approximately 48 MeV on the scanner detectors (DSSSD 1, DSSSD 2, and CEPA4). These regions are those with the highest energy deposited per hit on the scanner, as it was expected since these are the protons losing less energy in the phantom as they traverse 40 mm of PMMA. The lowest energy deposited per hit on the phantom was observed for the blue region that corresponds to the aluminum region. This is in agreement with the expectations since in this case protons are traversing 40 mm PMMA and 10 mm of aluminum, that it is a more dense material than PMMA. The shape of the aluminum piece was very defined in both, Figs. 5.2(c) and 5.2(e). The average energy deposited per hit on the scanner detectors in this region was approximately 20 MeV.

Around 1.6×10^6 events were analyzed to generate the two-dimensional plots of the energy lost per hit on the scanner at the phantom plane for the 1-hour measurement shown in Fig. 5.2(c). In comparison, approximately 8×10^5 events were processed for the measurement that lasted 30 minutes, whose image is shown in Fig. 5.2(e). Their equivalent images obtained from simulations are shown in Figs. 5.2(d) and 5.2(f) for 1.6×10^6 and 8×10^5 events, respectively. The corresponding images with similar statistics were obtained from Monte Carlo simulations performed by C. Ballesteros [6] and they are shown next to the experimental results for 1-hour and 30-minutes measurements. Similar to the experimental results, regions that correspond to different materials display heavy color gradients, going from the green frame that differentiates the PMMA from the air and aluminum that appear in slightly darker red and blue tones than the experimental figures.

All images are presented with the same granularity (128×128 pixels) and energy scales (10 - 50 MeV). As expected, for both experimental and simulated results, higher statistics increased the uniformity of the images.

Fig. 5.3 shows the histograms of the energy deposited per proton on the scanner detectors for the experimental measurements as obtained pixel by pixel in the images acquired with a proton beam of energy 100 MeV during 1 hour ($\sim 1.6 \times 10^6$ counts) and 30 minutes ($\sim 8 \times 10^5$ counts), and the 1-hour equivalent simulated measurement ($\sim 1.6 \times 10^6$ counts) of the cross phantom images. The energy deposited on each type of material did not show any drastic variations in the experimental results (lines blue and green). Experimentally, the energies deposited by protons passing through the aluminum region was larger than the obtained with the simulations, while the energy value was lower for the air regions when compared to the simulated results, as it was previously visually observed in Fig. 5.2. Similar values were obtained for the energy deposited for the PMMA regions on both, experimental and simulated results. The experimental energy distributions displayed larger standard deviations when compared to the simulated energy distribution, this might be due to the use of a lower value of the instrumental standard deviation on the simulations, which typically is manually added to account for all the instrumental contributions to the experimental resolution that are not included in the Monte Carlo simulation.

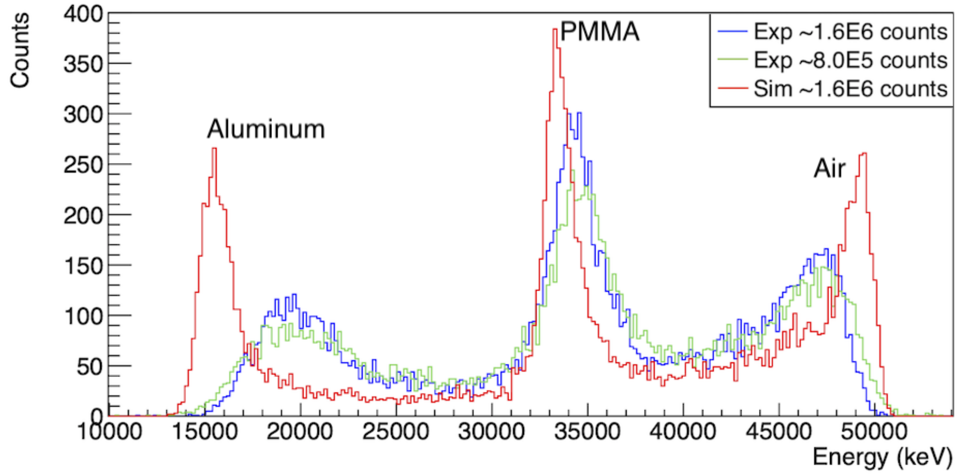

FIGURE 5.3: Histogram of the energy deposited per proton on the scanner detectors for the cross phantom with a proton beam of 100 MeV.

The average values of energy lost per hit on the scanner detectors for the different regions that composed the phantom were obtained by fitting a Gaussian curve on each of the peaks that are observed in Fig. 5.3. The values are shown in Table 5.1 as the centroid of each peak fit and their corresponding standard deviation.

TABLE 5.1: Average energies deposited on the pCT scanner prototype for the cross phantom. Energy values are presented as $\mu(\sigma)$.

	Experimental results		**Simulated results**	
Stats (counts) **Material**	$\sim$**1.6**$\times$**10**^{6} (MeV)	$\sim$**8**$\times$**10**^{5} (MeV)	$\sim$**1.6**$\times$**10**^{6} (MeV)	$\sim$**8**$\times$**10**^{5} (MeV)
Aluminum	19.6(18)	20(2)	15.5(7)	15.5(10)
PMMA	34.3(15)	34.7(16)	33.5(8)	33.6(10)
Air	47.1(12)	47.3(15)	49.1(6)	49.1(8)

5.1.1 Estimation of the phantom's dimensions

The final two-dimensional plot of the energy lost per hit at the phantom plane acquired for 1 hour was also represented in linear greyscale. Darker areas correspond to higher energy deposited on the pCT scanner. Fig. 5.4(a) shows the energy lost per hit with the energy ranges set by default with a lower contrast from a material to another. The empty areas appearing at the right side and bottom side of the figure cause the low contrast observed in the images due to the need of setting such areas to energy values equal to zero. After adjusting the lower and higher values of the greyscale, Fig. 5.4(b) was obtained and later analyzed.

Grey level profiles were obtained to determine all the dimensions of the phantom shown in Fig. 5.2(b). The general process to obtain the grey level profiles was performed with the software ImageJ and it included three steps that are enumerated as follows:

1. Generate a straight line using the line tool to select the region of interest (ROI).

2. Choose the width of the ROI equivalent to the line width to select a region of pixels and not only a single line of pixels to average the results and avoid the influence of statistical fluctuations. In this way a smoother grey level profile of the region is obtained.

3. Plot the profile of the region and export the data in text files for processing of the curves.

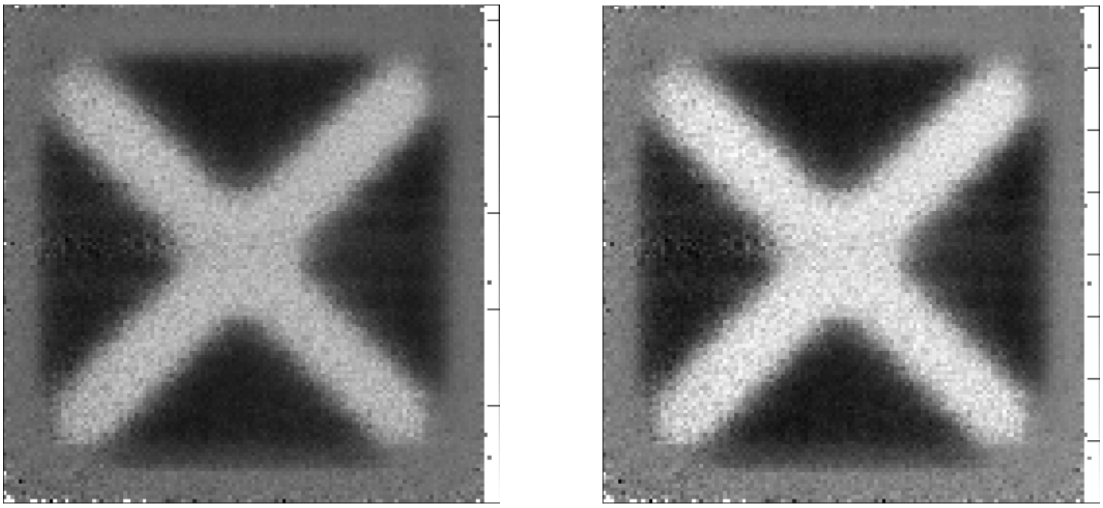

(a) Default greyscale from 0 to 75 MeV (b) greyscale from 10 to 50 MeV

FIGURE 5.4: Two-dimensional plot in greyscale of the energy lost per hit on the detectors at the phantom plane when irradiating the cross phantom with proton beams of 100 MeV.

Fig. 5.5(b) shows the grey level profile of the ROI marked in yellow on Fig. 5.5(a), and it displays different grey levels for the PMMA, air, and aluminum regions.

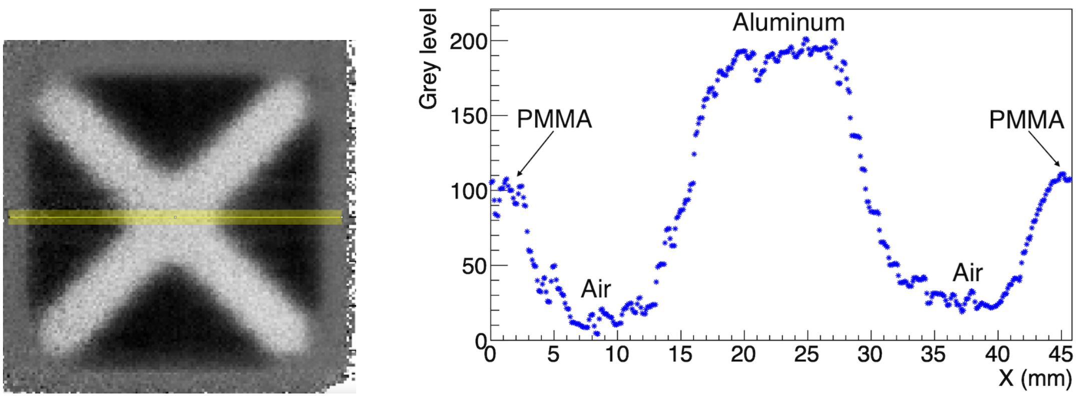

(a) Selected region in yellow (b) Grey level profile of the selected region

FIGURE 5.5: (a) Selected ROI marked as a wide straight line in yellow, (b) 1-dimensional plot of the ROI's grey level profile.

Fig. 5.6 shows the grey level profiles of the ROI marked in yellow on Fig. 5.5(a). Both profiles display different grey levels for the regions that correspond to the different materials, however, the averaged grey level profile shown in Fig. 5.6(b) displays a smoother behavior with less statistical fluctuations than the one presented in Fig.

5.6(a). The line width selected for all the obtained profiles was 15; this gave averaged profiles for all the ROIs that presented a more consistent behavior in the zones corresponding to the same material.

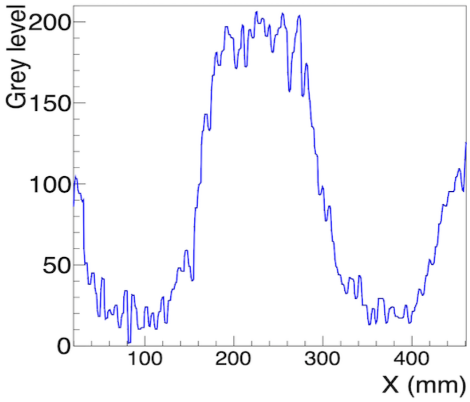

(a) Grey level profile of the ROI using a width line of 1

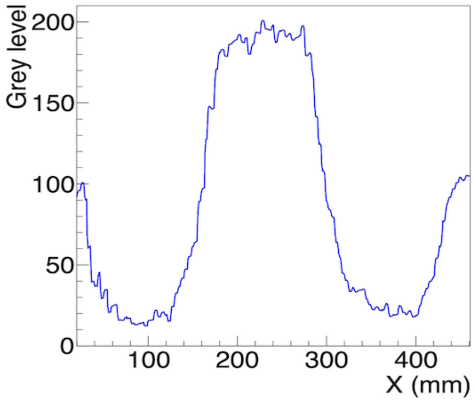

(b) Grey level profile of the ROI using a width line of 15

FIGURE 5.6: Grey level profile of the ROI marked in Fig. 5.5(a) using width lines of 1 and 15.

The regions of aluminum and air were extracted and individually fitted to the higher-order Gaussian function, also known as super-Gaussian distribution, shown in Eq. 5.1:

$$f(x) = a_0 + a_1 x + \frac{a_3}{\sqrt{2\pi} a_2} \exp\left(-\frac{1}{2}\left(\frac{(x-a_4)}{a_2}\right)^{a_5}\right) \tag{5.1}$$

where a_0 and a_1 are the parameters of the distribution's background assumed to be linear, a_2 is the standard deviation, a_3 is a multiplicative constant that defines the amplitude of the curve, a_4 is the mean value, and a_5 corresponds to the order of the super-Gaussian distribution. Fig. 5.7 shows the fit performed for the aluminum region of the grey level plot (Fig. 5.5(b)). The full width at half maximum (FWHM) and full width at tenth maximum (FWTM) are two important values of each fit that represent an estimation of the dimensions of the phantom.

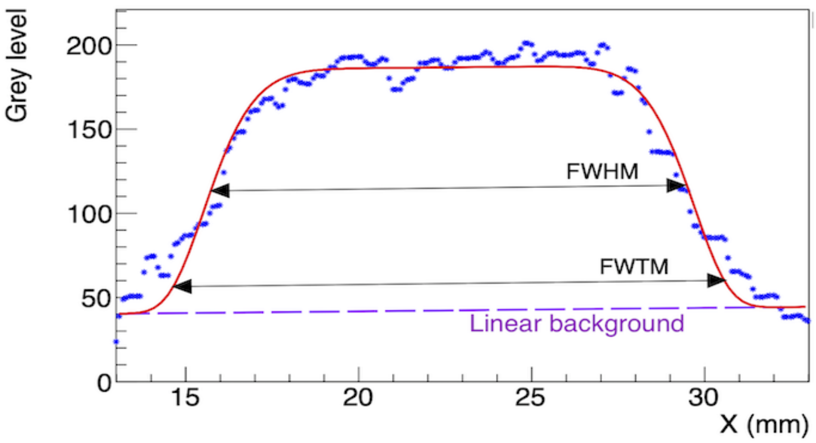

FIGURE 5.7: Fit of the grey level profile of the aluminum region shown in the example of Fig. 5.5(b).

The FWHM represents the distance between two points, one at each side of the maximum, on the fit curve whose intensity is 50% of the maximum. FWTM represents the distance between two points whose intensity is 10% of the peak. The FWHM and FWTM are calculated using Eqs. 5.2 and 5.3.

$$\mathrm{FWHM} = 2a_2\left(2\log(2)\right)^{1/a_5} \tag{5.2}$$

$$\mathrm{FWTM} = 2a_2\left(2\log(10)\right)^{1/a_5} \tag{5.3}$$

In general, the reconstruction of the images yielded reliable results comparable to those of the real phantom. The dimensions of the different parts of the cross calculated from the grey level profiles of the image, as defined in Fig. 5.2(b), are in agreement with the real values shown with grey background as shown in Table 5.2.

TABLE 5.2: Measurements of the aluminum cross phantom. The grey column corresponds to the dimensions of the phantom as measured directly from the piece, the dimensions are described in Fig. 5.2(b).

Dimension	**Real value** (mm)	**Fit order** a_5	**FWHM** (mm)	**ΔFWHM** (%)	**FWTM** (mm)	**ΔFWTM** (%)
W	39.70(5)	12	34.93(14)	12	38.60(15)	3
H	39.85(5)	12	35.15(15)	12	38.85(16)	3
c1	14.45(5)	8	14.07(10)	3	16.34(11)	13
c2	14.45(5)	8	13.36(7)	8	15.52(8)	7
d1	54.30(5)	10	48.7(2)	10	54.9 (2)	1
d2	54.35(5)	10	50.0(3)	8	56.4 (3)	4
w1	9.00(5)	6	7.31(5)	19	8.93(6)	1
w2	9.00(5)	6	7.05(6)	22	8.62(7)	4
w3	9.00(5)	6	6.95(6)	23	8.50(7)	6
w4	9.00(5)	6	6.91(7)	23	8.44(8)	6
h1	12.60(5)	4	14.04(7)	17	18.95(10)	1
b1	26.15(5)	8	24.87(8)	5	28.90(9)	11
h2	12.70(5)	8	11.22(14)	12	13.04(16)	3
b2	26.15(5)	8	23.17(5)	11	26.92(5)	3
h3	12.70(5)	12	11.40(11)	10	12.60(13)	1
b3	26.15(5)	8	22.84(7)	13	26.54(8)	1
h4	12.70(5)	8	11.99(8)	6	13.94(9)	10
b4	26.15(5)	12	24.98(6)	4	27.61(7)	6

The FWHM and FWTM are reported as the calculated dimensions of the phantom. A general result is that the values of the FWHM underestimated all the dimensions of the phantom. The highest deviations of the FWHM to the real values were 23% for the arm widths w3 and w4 (left side). The horizontal central region c1 presented the smallest deviation when considering the FWHM as the measured dimensions of the phantom. On the other hand, the FWTM overestimated more than half of the dimensions; however, it gave more accurate results than the FWHM with smaller deviations from the actual dimensions. Considering the FWHM as the measured dimensions of the phantom, the maximum deviation obtained corresponded to 13% of the real value.

5.2 Imaging the aluminum Derenzo-type phantom

The Derenzo-type phantom of Fig. 5.8(a), inserted in between two PMMA pieces of 20-mm thick each as shown in Fig. 5.1, was irradiated with proton beams of 100 MeV and 110 MeV. The data sets for 100-MeV proton beams were acquired in two measurements, one of 1 hour and another of 30 minutes. The irradiation using protons of 110 MeV lasted 15 minutes. The corresponding reconstructed images are shown in Figs. 5.8(c), 5.8(e) for the 100 MeV runs, and in Fig. 5.10(a) for the 110 MeV case. As was the case of the cross' images, greyscale images were built and exported as PNG to perform their post-analysis. The measurements indicated in Fig. 5.8(b) were performed.

Figs. 5.8(c) and 5.8(e) were both acquired with 100-MeV proton beams. However, they were acquired during 1 hour and 30 minutes, respectively.

Concerning the images taken with 100 MeV, the longer acquisition times also increased the uniformity of the image for this phantom since statistical fluctuations are reduced. Regardless of the different acquisition times, similar colour tones are observed for all the structures on both images.

The zones where protons pass through air appear in red tones, similarly to the images recorded with the cross-pattern phantom. Each proton that went through this material deposited approximately 48 MeV on the scanner detectors. The energy deposited on the regions where smaller circles are located is expected to be 48 MeV, but these appear in green tones that correspond to lower energy. Average energies deposited on the scanner prototype for aluminum and PMMA regions were 20 and 34 MeV, respectively.

Both experimental images taken with 100-MeV proton beams display six rectangular regions of similar widths and variable heights, nine clearly visible circles of different diameters grouped in three rows of two, three and four circles. It also shows a blurred zone corresponding to the row of 1-mm holes. The simulated results of approximately 1.6×10^6 and 8×10^5 events are shown in Fig. 5.8(d) and 5.8(f); these results contain similar statistics to the experimental measurements of Figs. 5.8(c) and 5.8(e). The experimental images were placed next to their simulated equivalent for comparison.

Fig. 5.9 shows the histograms of the energy deposited per proton on the scanner detectors for the experimental and simulated results of the Derenzo-type phantom images taken with 100-MeV proton beams. Results similar to the observed for the cross-shaped phantom were obtained.

Fig. 5.10 shows the experimental (5.10(a)) and simulated (5.10(b)) images for the measurement with a proton beam of 110 MeV. The data of Fig. 5.10(a) was acquired for 15 minutes with protons of 110 MeV. The experimental results show blurred edges when compared to the simulation. Similarly, the edges between materials on the results at 110 MeV are less defined when compared to the results obtained at 100 MeV.

Fig. 5.11 shows the histogram of energy deposited on the scanner prototype using protons of 110 MeV. In both, experimental and simulated results, two main peaks are observed. The peak at energies below 45000 keV corresponds to the protons that pass through aluminum, and the most intense peak corresponds to the protons that pass through PMMA. In here, it was clearly observed that the experimental energy distributions displayed larger standard deviations when compared to the simulated energy distribution, which leads to believe that this behavior might be partially explained by the use of a lower value of the instrumental standard deviation on the simulations. Further studies are needed to determine the effects that account for the observed behavior.

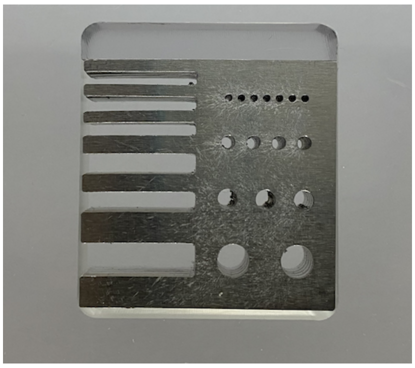

(a) Phantom insert

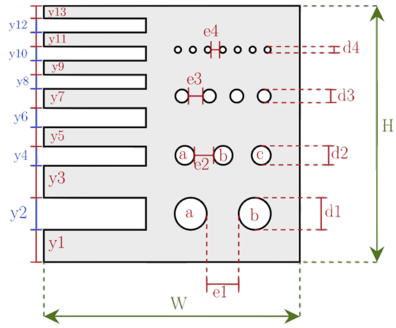

(b) Lengths of the phantom defined for the comparison between results

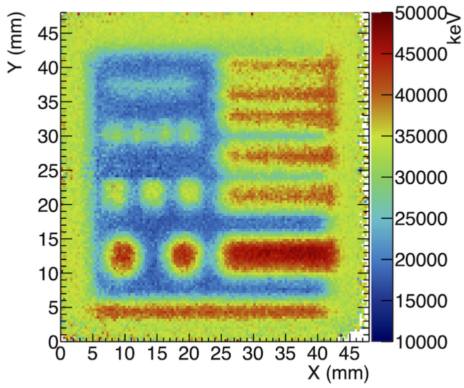

(c) Experimental image from 1-hour measurement corresponding to 1.6×10^6 counts

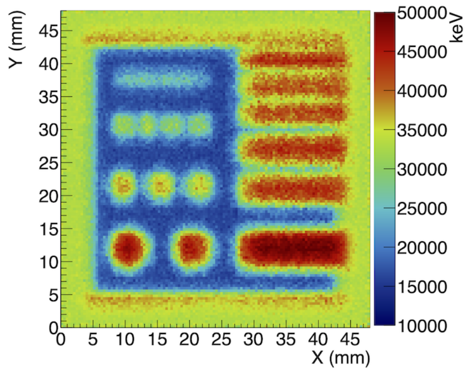

(d) Simulation with $\approx 1.6 \times 10^6$ counts

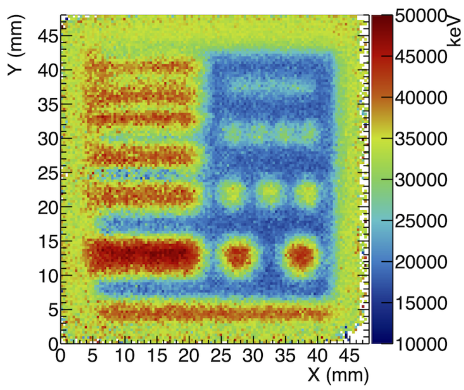

(e) Experimental image from 30-min measurement corresponding to 8×10^5 counts

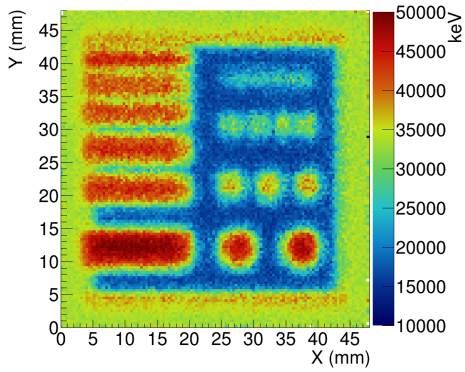

(f) Simulation with $\approx 8 \times 10^5$ counts

FIGURE 5.8: (a) Aluminum Derenzo-type phantom, (b) Lengths of the phantom defined for the comparison between experimental and simulated results. Two-dimensional plots of the energy lost per hit on the scanner at the phantom plane with a 100-MeV proton beam (c) Experimental image for the 1-hour measurement (1.6×10^6 counts), (d) Simulation with $\approx 1.6 \times 10^6$ counts, (e) Experimental image for the 30-minutes measurement (8×10^5 counts), (f) Simulation with $\approx 8 \times 10^5$ counts. Images (d) and (f) taken from [6].

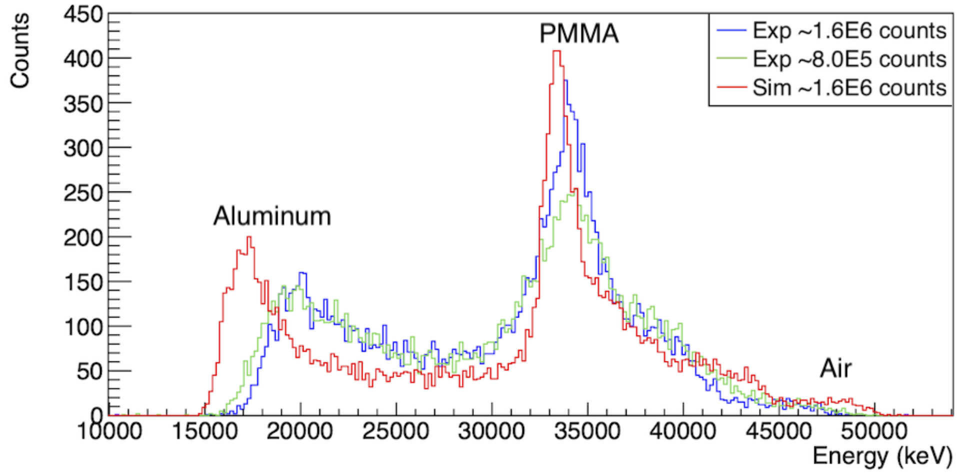

FIGURE 5.9: Histograms of the energy deposited per proton on the scanner detectors for the Derenzo-type phantom with protons of 100 MeV.

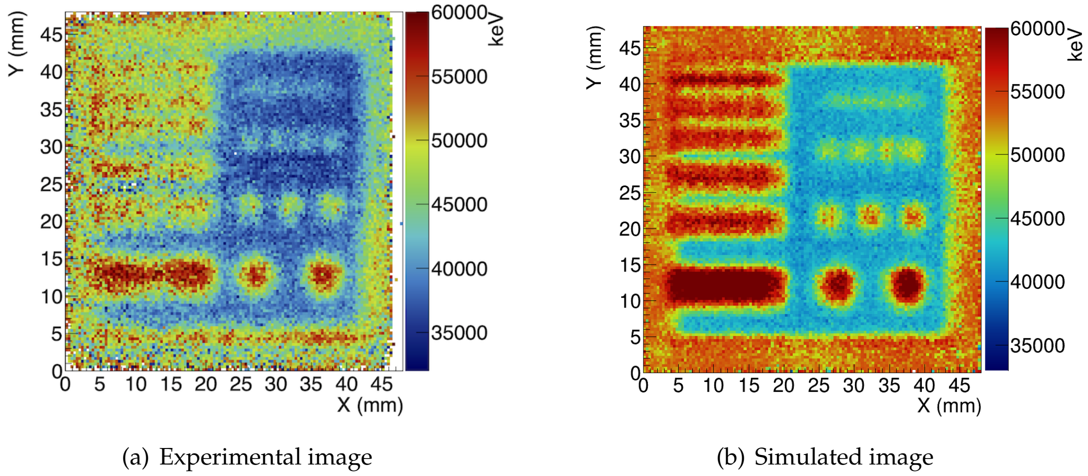

FIGURE 5.10: Two-dimensional plots of the energy lost per hit on the scanner at the phantom plane for the measurement with a 110-MeV proton beam. (a) Image obtained experimentally for a measurement of 15 minutes, (b) Image obtained from Monte Carlo simulations containing $\approx 6 \times 10^5$ counts. Image (b) taken from [6].

Table 5.3 shows the average values of the deposited energies on the pCT scanner detectors for the three regions of the different materials that composed the phantom for both beam energies. The values of the deposited energies were obtained by fitting a Gaussian curve on each of the peaks that are observed in Figs. 5.9 and 5.11, and the values are shown in Table 5.3 as the centroid of each peak fit and their corresponding standard deviation.

For the measurements performed at 100 MeV, the similarity of the deposited energies on the scanner must be highlighted regardless of the acquisition times. While the different structures are still visible on the images taken with 110-MeV protons, the edges of the materials are less notorious than with lower beam energy. The leading cause of this effect is that for 100-MeV protons the depth of the Bragg peak is closer to the accumulated proton range after passing all the layers of the phantom than for

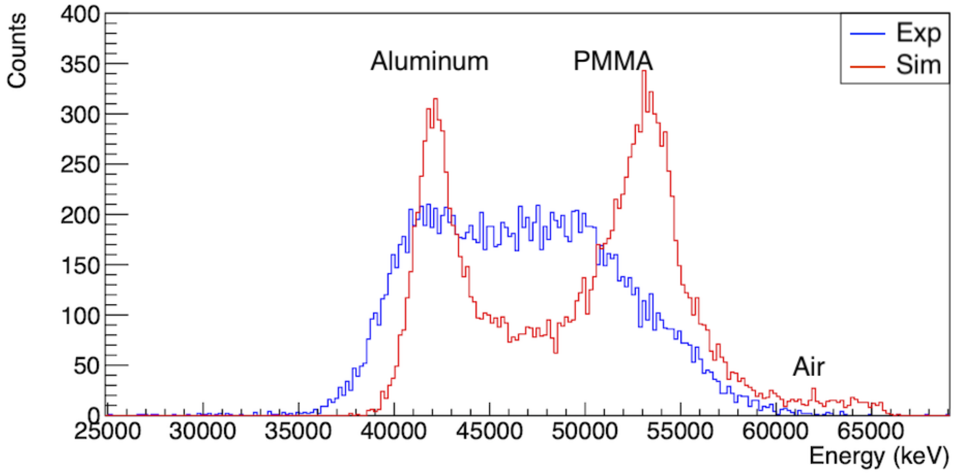

FIGURE 5.11: Histograms of the energy deposited per proton on the scanner detectors for the Derenzo-type phantom with protons of 110 MeV. Both, experimental and simulated results contain $\sim 6 \times 10^5$ counts.

TABLE 5.3: Average energies deposited on the pCT scanner prototype for the Derenzo-type phantom. for the cross phantom. Energy values are presented as $\mu(\sigma)$.

	Experimental results			**Simulated results**	
Beam energy	**100 MeV**		**110 MeV**	**100 MeV**	**110 MeV**
Stats (counts)	**$\sim$1.6$\times$10^6**	**$\sim$8$\times$10^5**	**$\sim$6$\times$10^5**	**$\sim$1.6$\times$10^6**	**$\sim$6$\times$10^5**
Material	(MeV)	(MeV)	(MeV	(MeV)	(MeV)
Aluminum	20.1(14)	19.6(15)	41(2)	17.2(10)	42.1(11)
PMMA	34.0(14)	34(2)	48(4)	33.5(9)	53.2(15)
Air	45(2)	–	–	48(2)	62(2)

110 MeV. This means that the gradient of the stopping power of protons is more pronounced for 100 MeV than for 110 MeV and, therefore, it provokes larger differences for different materials traversed in the image recorded.

Experimentally, the deposited energies on the scanner prototype for the case of 110-MeV proton beam range from approximately 40 MeV up to around 58 MeV. Although the simulation appears to describe the phantom with excellent fidelity, it is not possible to experimentally arrive to the same result unless an adjustment of the color scale without a prior adjustment of the color scale.

These differences between the experimental and simulated results in the maximum and minimum deposited energies on the scanner detectors were observed for all proton energies but they became more evident for the results at 110-MeV proton beams. Some possible causes for these discrepancies are:

- The experimental thresholds of the detectors generate a rather small increment on the average energy measured on the low-energy region of the CEPA4 spectra.
- The value of the density assigned in the simulations for PMMA and/or aluminum materials might be different from the density of the material used in the experiment.
- Overestimation on the beam energy spread in the simulated results.

The experimental and simulated results for 110-MeV beam energy do not correspond to each other as well as the 100-MeV results. Experimentally, the energy deposited per proton on all the materials is approximately 3.5 MeV **lower** than the simulated values. This difference motivated the modification on the color bar's range in the experimental results and the color distribution of the simulations was achieved, showing more similarities as shown in Fig. 5.12. A lower definition of the different shapes presented on the phantom is still observed in the experimental results compared to the result from the simulation. It must be highlighted that the acquisition time of the images taken at 110 MeV was only 15 minutes, which decreased the number of analyzed events, i.e. the statistics of the image. Higher acquisition times might help to define and improve the uniformity of the images.

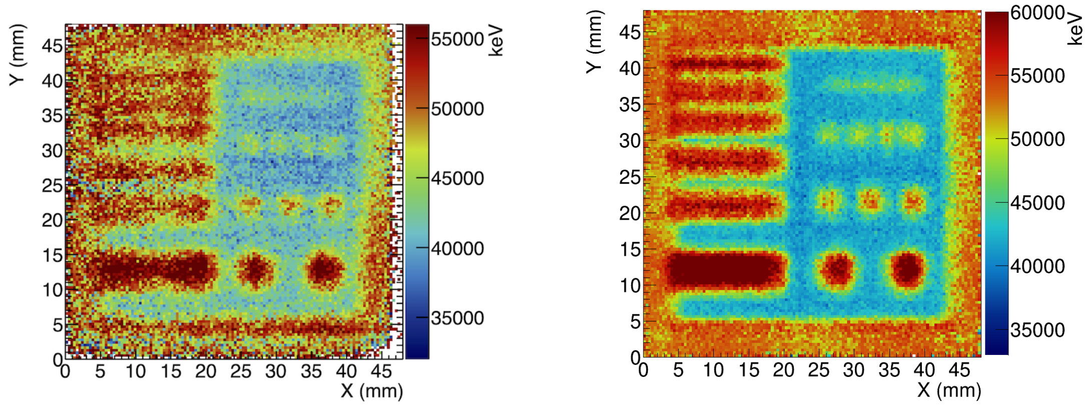

(a) Image from experiment with $\approx 6 \times 10^5$ counts after manually modifying the colour scale to be from 32000 to 56000 keV

(b) Image from Monte Carlo simulation with $\approx 6 \times 10^5$ counts

FIGURE 5.12: Two-dimensional plots of the energy lost per hit on the scanner at the phantom plane with 110-MeV proton beam (a) 15 minutes measurement with modified color bar (b) Simulation with $\approx 6 \times 10^5$ counts. Image (b) taken from [6].

5.2.1 Estimation of the phantom's dimensions

The phantom dimensions represented in Fig. 5.8(b) were estimated with the process described in section 5.1.1. The images that were analyzed are shown in Figs. 5.13(a) and 5.13(b), the greyscale images of the phantom were taken using 100-MeV and 110-MeV proton beams. An aspect to take into account is that the image taken using protons of 100 MeV had fourfold the acquisition time of the image taken with 110 MeV protons, and about 2.5 times more statistics (1.5×10^6 vs 6×10^5 counts). This short time might cause, up to a point, the non uniform distribution on the image of 110 MeV (Fig. 5.13(b)). The changes on the experimental images are easily perceived. However, these visual changes are not so evident on the simulated results, where all the structures appear defined very similar for both energies.

Fig. 5.14(b) shows a vertical grey-level profile of the ROI marked in yellow on Fig. 5.14(a). The rectangular sections of aluminum and air of the Derenzo-type phantom will be called as the bars and slits from now on. It is observed that the system's capability to differentiate between regions of different materials decreases with the size of the structures. Seven regions with local maxima are observed and they correspond to the seven bars of decreasing widths, from left to right, that are present in the phantom.

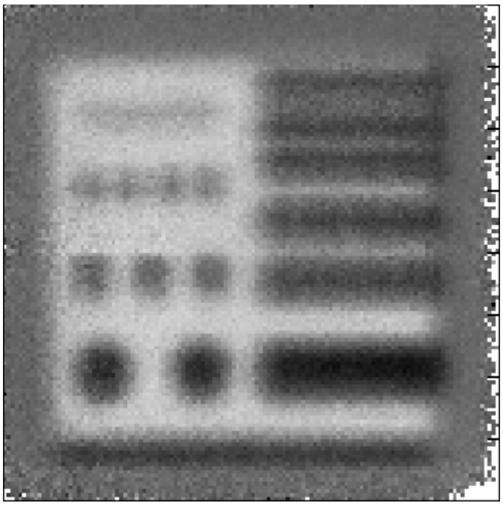

(a) Image of the Derenzo phantom obtained with 100-MeV protons

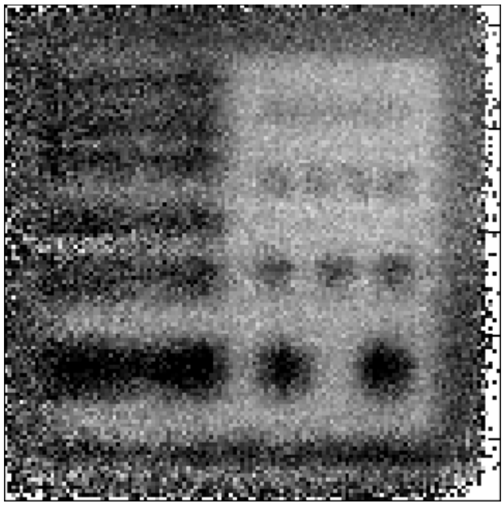

(b) Image of the Derenzo phantom obtained with 110-MeV protons.

FIGURE 5.13: Two-dimensional plots in greyscale of the energy lost per hit on the detectors at the phantom plane when irradiating the Derenzo-type phantom obtained experimentally with a beam energy of (a) 100 MeV and (b) 110 MeV.

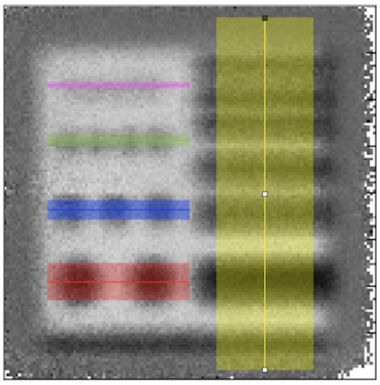

(a) Selected ROIs for the analysis of the phantom

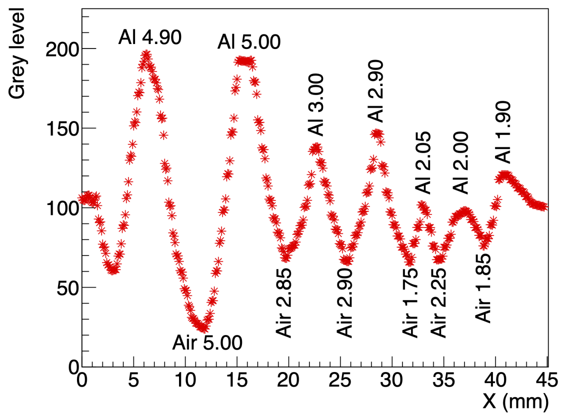

(b) Grey level profile of the yellow region

FIGURE 5.14: (a) Selected ROIs for the Derenzo-type phantom, (b) Grey-level profile of the yellow ROI (bars and slits) for the image taken with 100-MeV protons, the sections widths decrease from left to right. The labels on the figure correspond to the material and dimension expressed in mm of the region.

The regions where protons pass through air are observed as the seven sections with local minima, the first one of which corresponds to the air gap between the aluminum structure of the phantom and the PMMA frame, as it can be seen in the picture of Fig. 5.8(a), and the rest are the slits of variable widths. The left and right borders of the figure correspond to the grey level of PMMA.

A decrease in the contrast between air and aluminum is observed when scanning structures of smaller sizes, this is related to the spatial resolution of the scanner prototype, and up to some extent, this phantom helps to define the system capability by determining the size of the smallest shapes that can be distinguished on the phantom.

Fig. 5.15 shows the grey level profiles of the horizontal ROIs that cover the four rows of the circles with different diameters (shown in Fig. 5.14(a)) of the image taken with 100-MeV protons. The color of the ROIs in 5.14(a) correspond to the color of the markers in Fig. 5.15. The regions with local minima correspond to the circular holes, thus, to the air regions traversed by of protons, while the local maxima refer to the aluminum regions traversed by the protons. It is observed a difference in the contrast between aluminum and air regions. This contrast decrease is related to the system's capability to distinguish small structures made of different materials.

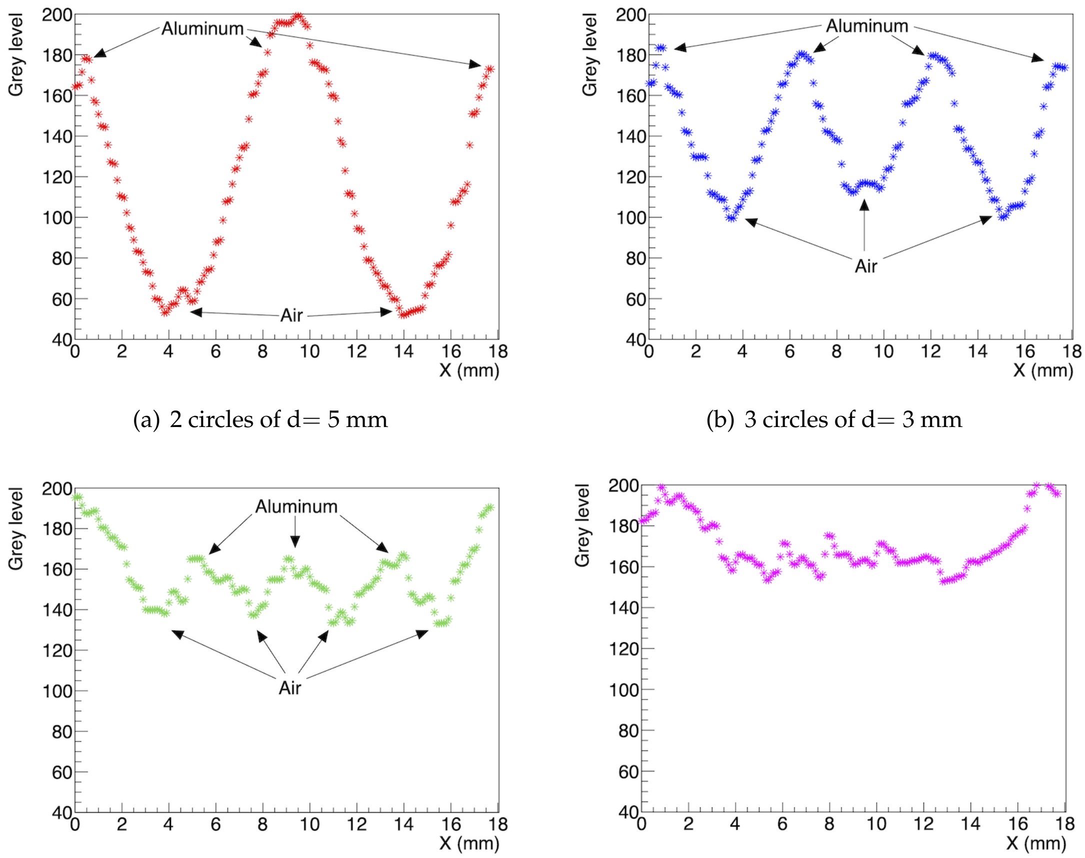

(a) 2 circles of d= 5 mm

(b) 3 circles of d= 3 mm

(c) 4 circles of d= 2 mm

(d) 7 circles of d= 1 mm

FIGURE 5.15: Grey-level profiles of the image taken with 100 MeV protons for the circles of 5 mm, 3 mm, 2 mm, and 1 mm diameter.

The grey level profiles of the Derenzo-type phantom allowed the determination of the structures' sizes for both images taken with 100-MeV and 110-MeV proton beams. The phantom was composed by two regions of different shapes. The first region included four rows of circles of variable diameters, going from 5 mm to 1 mm. The second section of the phantom included the bars and slits of variable widths. The dimensions of the circles and gaps were obtained using the Eq. 5.2 and 5.3 after performing the corresponding Gaussian fits. It is expected that the dimensions of the phantom are within the limits defined by the FWHM and the FWTM. Table 5.4 shows the dimensions of the FWHM and FWTM of each section. The grey column shows the dimensions of the shapes present in this phantom that are defined in Fig. 5.8(b).

In general, the dimensions measured from the image taken with protons of 100 MeV were more accurate than the dimensions obtained from the 110 MeV image. The 1-mm diameter circles were not resolved for any of the energies used in this experiment. While the circles with diameter of 2 mm were observed for both energies, it was possible to determine their dimensions only for the image taken with 100 MeV protons due to the low statistics of the measurement with 110 MeV. The average dimensions of this region were 1.88 mm with a statistical error of 43% for the diameters and 2.49 mm $\pm$0.6% for the gaps between circles. The regions with circles of 3-mm and 5-mm diameter were accurately measured. The bars and slits were measured in both images and lay within the expected values, except for y6, y9, and y13.

TABLE 5.4: Measurements of the aluminum Derenzo-type phantom. The column **M** represents the material of the region: aluminum (Al) or air. The grey column corresponds to the real dimensions of the phantom described in Fig. 5.8(b).

			100 MeV			110 MeV		
Dimension	**M**	**Real value** (mm)	**Fit order** a_5	**FWHM** (mm)	**FWTM** (mm)	**Fit order** a_5	**FWHM** (mm)	**FWTM** (mm)
W	Al	40.05(5)	16	36.28(11)	39.11(12)	16	36.73(16)	39.59(17)
H	Al	38.90(5)	16	37.33(11)	40.24(12)	16	36.81(13)	39.68(14)
d1(a)	Al	5.00(5)	6	4.87(7)	5.95(9)	4	4.76(8)	6.43(10)
d1(b)	Al		6	4.80(6)	5.86(8)	4	4.80(4)	6.48(5)
e1(a)	Air	5.00(5)	6	4.85(9)	5.92(11)	4	5.40(7)	7.29(10)
d2(a)	Al	2.95(5)	4	3.30(5)	4.45(7)	4	3.24(6)	4.37(8)
d2(b)	Al		4	3.30(4)	4.45(6)	4	3.28(9)	4.42(12)
d2(c)	Al		4	3.25(3)	4.39(4)	2	3.24(8)	5.91(14)
e2(a)	Air	3.00(5)	6	2.87(8)	3.51(9)	6	3.00(10)	3.66(13)
e2(b)	Air		6	2.78(6)	3.40(7)	4	3.21(14)	4.33(20)
d3(a)	Al	2.00(5)	6	2.70(16)	3.30(19)	-	-	-
d3(b)	Al		4	0.91(8)	1.23(11)	-	-	-
d3(c)	Al		6	1.53(9)	1.87(11)	-	-	-
d3(d)	Al		4	2.39(8)	3.23(11)	-	-	-
e3(a)	Air	2.00(5)	6	2.13(3)	2.60(4)	-	-	-
e3(b)	Air		6	3.18(6)	3.88(7)	-	-	-
e3(c)	Air		6	2.18(11)	2.66(13)	-	-	-
y1	Al	4.90(5)	6	3.88(10)	4.74(12)	8	4.45(8)	5.17(9)
y2	Air	5.00(5)	6	4.5 (2)	5.4 (3)	6	5.57(7)	6.80(9)
y3	Al	5.00(5)	6	4.05(13)	4.94(16)	6	4.52(16)	5.53(19)
y4	Air	3.00(5)	2	2.94(9)	5.35(16)	8	4.18(7)	4.86(8)
y5	Al	3.00(5)	2	2.95(7)	5.37(12)	4	2.27(8)	3.06(11)
y6	Air	2.90(5)	2	3.14(5)	5.72(09)	6	3.08(10)	3.76(12)
y7	Al	2.90(5)	2	2.87(8)	5.23(14)	4	3.31(7)	4.47(10)
y8	Air	1.75(5)	4	2.09(8)	2.82(10)	6	2.00(6)	2.45(8)
y9	Al	2.05(5)	2	1.36(5)	2.48(9)	6	1.69(14)	2.07(17)
y10	Air	2.25(5)	4	2.06(6)	2.79(9)	8	3.27(12)	3.80(14)
y11	Al	2.00(5)	2	2.26(7)	4.11(13)	4	2.88(14)	3.89(18)
y12	Air	1.85(5)	2	1.62(8)	2.96(15)	4	2.10(11)	2.84(14)
y13	Al	1.90(5)	2	2.60(10)	4.75(17)	6	3.60(8)	4.40(10)

With these results, it is possible to say that this scanner prototype was capable to resolve structures as small as 2 mm of aluminum of the Derenzo-type phantom for proton beams of 100 MeV, and 3 mm for proton beams of 110 MeV. However, there is still a possibility to infer the location and size of isolated 2 mm shapes on the images generated with 110 MeV proton beams despite the low statistics of this measurement.

Chapter 6

Conclusions

A prototype of a pCT scanner has been developed at the *Instituto de Estructura de la Materia* of the *Consejo Superior de Investigaciones Científicas* (IEM-CSIC). It was tested at the Cyclotron Centre Bronowice (CCB) in Krakow, Poland, using proton beams with energies between 95 and 120 MeV during the first week of June 2021. This work presents the analysis of the radiography images taken with the scanner prototype and a comparison with Monte Carlo simulations performed by C. Ballesteros as part of his Master thesis [6].

Three different phantoms with planar geometry that were composed of aluminum and PMMA were imaged using two double-sided silicon strip detectors of 1000 μm thickness (DSSSDs) and the CEPA4 detector, a compound scintillator of 4 crystal arrays of $LaBr_3$(Ce) (4 cm) and $LaCl_3$(Ce) (6 cm) in phoswich configuration. The DSSSDs were used as particle trackers, and the CEPA4 detector was used to measure the residual energy of the particles. The calibration of the detectors was performed using a phantom that consisted of three uniform layers of PMMA, with a total thickness of 50 mm.

The conclusions of this work are:

- In order to reconstruct the image, data have been selected in triple coincidence. The production of *continuous* images was possible by the use of a random generator tool to uniformly distribute the statistics of each pixel over the its full area.
- The different materials used in the cross-shaped phantom were clearly distinguished in the resulting image created by adding the energy deposited in the three detectors of the scanner.
- The FWHM and FWTM of the super-Gaussian fits to the grey-level profiles of the image were compared to the real dimensions of the phantom. For the cross-shaped phantom, the FWHM underestimated the phantom dimensions by 4% to 23%. The FWTM gave more accurate results, overestimating the actual dimensions on 1% to 13%.
- The complex structure of the Derenzo-type phantom was well separated except for the 1-mm circles were observed. As a result, the scanner prototype was capable to resolve structures as small as 2 mm.
- The uniformity of the images generated for both phantoms increased when larger number of events were analyzed as statistical fluctuations on the energy deposited on the scanner detectors were reduced.

6.1 Outlook

The described planar image reconstruction, as done in this work, is a good starting point for the analysis of the tomographic scans using a cylindrical phantom with three different materials and a three-dimensional Derenzo-type phantom. The next steps in the development of the pCT scanner prototype include the tomographic reconstruction algorithms of three-dimensional images applying the data analysis developed in this work to study a phantom that includes inserts with different materials (water and alcohol).

As a continuation of this work, a proposal to study more complex phantoms at energies relevant for proton therapy, $\sim$ 200 MeV, was presented to the International Advisory Committee of CCB facility in Krakow, Poland, on August 27, 2021.

Appendix A

Centroids of the calibration peaks

In this appendix, the centroids of the energy loss peaks on the detectors for the three calibration energies are presented.

TABLE A.1: Centroids of the energy loss peaks on DSSSD 1 for the three calibration energies. Energies of the beam: 95, 100, and 120 MeV.

Strip	**Vertical strips**			**Horizontal strips**		
number	**95 MeV** (ch)	**100 MeV** (ch)	**120 MeV** (ch)	**95 MeV** (ch)	**100 MeV** (ch)	**120 MeV** (ch)
0	1394.20	1360.94	1166.41	0	0	0
1	1465.96	1438.51	1231.79	1442.10	1396.86	1205.92
2	1463.80	1419.93	1218.51	1403.74	1355.86	1171.80
3	1408.22	1365.25	1175.78	1425.79	1385.79	1201.42
4	1433.60	1402.43	1198.64	1359.24	1309.61	1140.13
5	1373.26	1333.19	1153.98	1380.13	1336.68	1157.87
6	1366.25	1323.24	1139.14	1407.78	1367.86	1196.53
7	1333.80	1296.14	1122.16	1351.57	1312.72	1141.44
8	1376.50	1322.22	1141.53	1362.74	1296.31	1151.23
9	1420.91	1392.42	1208.61	1395.05	1353.10	1176.85
10	1371.63	1324.53	1145.00	1296.37	1260.58	1098.00
11	1298.55	1253.62	1080.43	1378.77	1336.51	1163.78
12	1324.81	1304.34	1111.63	1387.25	1348.87	1168.00
13	1387.72	1365.28	1173.54	1437.56	1390.84	1299.80
14	1342.75	1302.97	1104.67	1427.99	1368.42	1182.88
15	0	0	0	1383.04	1262.34	1163.21

TABLE A.2: Centroids of the energy loss peaks on DSSSD 2 for the three calibration energies. Energies of the beam: 95, 100, and 120 MeV.

Strip number	Vertical strips 95 MeV (ch)	100 MeV (ch)	120 MeV (ch)	Horizontal strips 95 MeV (ch)	100 MeV (ch)	120 MeV (ch)
0	0	0	0	1812.22	1414.56	903.666
1	1875.96	1473.19	955.688	1860.33	1460.70	931.139
2	1819.46	1439.97	946.143	1903.89	1459.18	961.571
3	0	0	0	1770.17	1411.28	898.575
4	0	0	0	1785.59	1421.63	899.575
5	1864.80	1489.78	968.057	1787.66	1385.27	891.855
6	1891.85	1497.11	977.606	1800.32	1399.31	922.811
7	1824.65	1453.90	954.932	1820.40	1441.61	932.482
8	1846.65	1470.16	955.272	0	0	0
9	1894.87	1514.79	981.102	1767.99	1399.87	894.563
10	1752.74	1393.55	891.383	1770.74	1398.50	904.919
11	1808.41	1445.20	945.584	1738.38	1378.07	885.838
12	1792.37	1434.12	928.489	1815.18	1434.96	922.534
13	1794.47	1426.25	926.370	1810.60	1422.90	920.390
14	1792.71	1421.30	866.904	1821.23	1415.75	921.818
15	1893.97	1508.73	983.277	1889.77	1497.21	972.776

TABLE A.3: Centroids of the energy loss peaks on CEPA4 for the three calibration energies. Energies of the beam: 95, 100, and 120 MeV.

Crystal number	Anodes 95 MeV (ch)	100 MeV (ch)	120 MeV (ch)	Dynodes 95 MeV (ch)	100 MeV (ch)	120 MeV (ch)
1	990.339	2026.48	-	331.234	669.013	1456.78
2	952.386	1948.70	-	305.516	617.833	1356.35
3	1103.60	2271.68	-	411.638	841.979	1855.18
4	835.816	1754.52	3866.83	-	-	-

Appendix B

Calibration parameters

In this appendix, the calibration parameters for the detectors are presented. Detectors were calibrated with linear fits between the centroids of the peaks displayed in the spectra and the energies of the Table 4.1. The offsets of the DSSSD 1 and DSSSD2 are of the order of 1.9×10^{-13} and 3.9×10^{-13}, respectively; therefore, they have been reported as 0.

TABLE B.1: Calibration parameters for the DSSSDs.

	DSSSD 1				DSSSD 2			
Strip	P side		N side		P side		N side	
number	Slope (kev/ch)	Offset (keV)	Slope (kev/ch)	Offset (keV)	Slope (kev/ch)	Offset (keV)	Slope (kev/ch)	Offset (keV)
0	1.012	0.00	1.000	0.00	1.000	0.00	1.938	0.00
1	0.962	0.00	0.978	0.00	1.872	0.00	1.887	0.00
2	0.963	0.00	1.005	0.00	1.930	0.00	1.844	0.00
3	1.001	0.00	0.989	0.00	1.000	0.00	1.984	0.00
4	0.984	0.00	1.038	0.00	1.000	0.00	1.967	0.00
5	1.027	0.00	1.022	0.00	1.883	0.00	1.964	0.00
6	1.032	0.00	1.002	0.00	1.856	0.00	1.950	0.00
7	1.057	0.00	1.043	0.00	1.924	0.00	1.929	0.00
8	1.025	0.00	1.035	0.00	1.901	0.00	1.000	0.00
9	0.992	0.00	1.011	0.00	1.853	0.00	1.986	0.00
10	1.028	0.00	1.088	0.00	2.003	0.00	1.983	0.00
11	1.086	0.00	1.023	0.00	1.942	0.00	2.020	0.00
12	1.065	0.00	1.017	0.00	1.959	0.00	1.934	0.00
13	1.016	0.00	0.981	0.00	1.957	0.00	1.939	0.00
14	1.050	0.00	0.988	0.00	1.959	0.00	1.928	0.00
15	1.000	0.00	1.020	0.00	1.854	0.00	1.858	0.00

TABLE B.2: Calibration parameters for the CEPA4.

	Crystal 1		Crystal 2		Crystal 3		Crystal 4	
Output	Slope (kev/ch)	Offset (keV)	Slope (kev/ch)	Offset (keV)	Slope (kev/ch)	Offset (keV)	Slope (kev/ch)	Offset (keV)
Anode	14.340	1206.9	14.878	1477.2	12.484	1976.4	17.301	391.26
Dynode	46.304	28.184	49.503	273.29	36.375	-142.95		

Appendix C

Centroids and FWHM of the DSSSDs

This appendix contains the centroids and FWHM of the DSSSDs at 100 MeV.

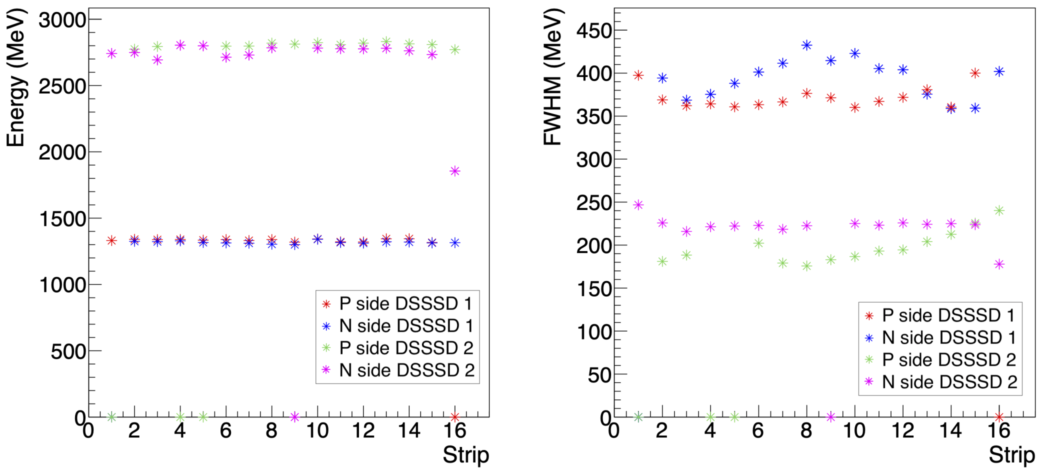

(a) Centroids

(b) Resolution

FIGURE C.1: (a) Centroids of the energy spectra of all strips of each DSSSD (P and N) (b) Energy resolution of all strips of each DSSSD (P and N)

Bibliography

[1] B. Healy, D. van der Merwe, K. Christaki, and A. Meghzifene, Clinical Oncology **29**, 110 (2017).

[2] J. Zindler, C. Thomas, S. Hahn, A. L. Hoffmann, E. Troost, and P. Lambin, JNCI: Journal of the National Cancer Institute **108**, 10.1093/jnci/djv305 (2016).

[3] C. Sarosiek, E. A. DeJongh, G. Coutrakon, D. F. DeJongh, K. L. Duffin, N. T. Karonis, C. E. Ordoñez, M. Pankuch, V. Rykalin, J. R. Winans, et al., Medical Physics **48**, 2271 (2021).

[4] R. P. Johnson, Reports on Progress in Physics **81**, 10.1088/1361-6633/aa8b1d (2018).

[5] *Pronto presentation*, http://nuclear.fis.ucm.es/pronto-en/.

[6] C. Ballesteros, "Estudio de capturas radiográficas de fantomas gruesos empleando el prototipo de escáner de protones del IEM-CSIC", Master's thesis (Universidad Complutense de Madrid, 2021).

[7] F. M. Khan and J. P. Gibbons, *Khan's the physics of radiation therapy* (Lippincott Williams & Wilkins, 2014).

[8] G. F. Knoll, *Radiation detection and measurement* (John Wiley & Sons, 2010).

[9] R. D. Evans and R. Evans, *The atomic nucleus*, Vol. 582 (McGraw-Hill New York, 1955).

[10] M. M. Khalil and P. Zanzonico, *Basic sciences of nuclear medicine* (Springer, 2011).

[11] W. D. Newhauser and R. Zhang, Physics in Medicine & Biology **60**, R155 (2015).

[12] G.-L. Jiang, Frontiers of medicine **6**, 165 (2012).

[13] S. H. Park and J. O. Kang, Radiation oncology journal **29**, 135 (2011).

[14] K Ilicic, S. Combs, and T. Schmid, Radiation oncology **13**, 1 (2018).

[15] H. Suit, T. DeLaney, S. Goldberg, H. Paganetti, B. Clasie, L. Gerweck, A. Niemierko, E. Hall, J. Flanz, J. Hallman, et al., Radiotherapy and Oncology **95**, 3 (2010).

[16] V. Giacometti, "Modelling and improvement of proton computed tomography", PhD thesis (University of Wollongong, 2016).

[17] V. García Távora, "Simulaciones Monte Carlo para el desarrollo de un prototipo de tomógrafo de protones con aplicación en protonterapia", Master's thesis (Universidad de Sevilla, 2019).

[18] M. I. Posadillo de Bringas, "Desarrollo de un prototipo con DSSDs para realizar imagen médica con protones", Master's thesis (Universidad de Sevilla, 2019).

[19] E. Nácher, M. Mårtensson, O. Tengblad, H. Álvarez-Pol, M. Bendel, D. Cortina-Gil, R. Gernhäuser, T. Le Bleis, A. Maj, T. Nilsson, A. Perea, B. Pietras, G. Ribeiro, J. Sánchez Del Río, J. Sánchez Rosado, A. Heinz, B. Szpak, M. Winkel, and M. Zieblinski, Nuclear Instruments and Methods in Physics Research, Section A: Accelerators, Spectrometers, Detectors and Associated Equipment **769**, 105 (2015).

[20] O. Tengblad, U. C. Bergmann, L. M. Fraile, H. O. Fynbo, and S. Walsh, Nuclear Instruments and Methods in Physics Research, Section A: Accelerators, Spectrometers, Detectors and Associated Equipment **525**, 458 (2004).

[21] O. Tengblad, T. Nilsson, E. Nácher, H. T. Johansson, J. A. Briz, M. Carmona-Gallardo, C. Cruz, V. Gugliermina, A. Perea, J. Sanchez Del Rio, M. Turrión Nieves, J. Bergström, E. Blomberg, A. Bülling, E. Gallneby, J. Hagdahl, L. Jansson, K. Jareteg, R. Masgren, M. Nordström, G. Risting, S. Shojaee, and H. Wittler, Nuclear Instruments and Methods in Physics Research, Section A: Accelerators, Spectrometers, Detectors and Associated Equipment **704**, 19 (2013).

[22] C. Rozsa, P. R. Menge, and M. Mayhugh, Saint Gobain Crystals (2007).

[23] mesytec GmbH & Co. KG, *Mvme - mesytec vme data acquisition*, English, version Version 1.4.5, mesytec GmbH & Co. KG (2021), 82 pp., 2021.

[24] P. Kerr and V. Mozin, *Stilbene scintillator detector array and data-acquisition system for active interrogation*, tech. rep. (Lawrence Livermore National Lab.(LLNL), Livermore, CA (United States), 2018).

[25] F. Lüke, *Mesytec-mvlc*, `https://github.com/flueke/mesytec-mvlc`, 2021.

[26] R. Brun and F. Rademakers, Nuclear Instruments and Methods in Physics Research Section A: Accelerators, Spectrometers, Detectors and Associated Equipment **389**, 81 (1997).

[27] *Overview geant4*, `https://geant4.web.cern.ch/node/`.

[28] CCB, *Cyclotron proteus c-235*, `https://ccb.ifj.edu.pl/en.cyklotron_proteus_c_235.html`, 2021.

[29] D. Vandeplassche, W. Beeckman, S. Zaremba, Y. Jongen, and T. Tachikawa, in Proceedings of the 1997 particle accelerator conference (cat. no. 97ch36167), Vol. 1 (IEEE, 1997), pp. 1045–1047.

[30] C. A. Schneider, W. S. Rasband, and K. W. Eliceiri, Nature methods **9**, 671 (2012).